



ISSN 1028-8546

Volume XXVI, Number 1

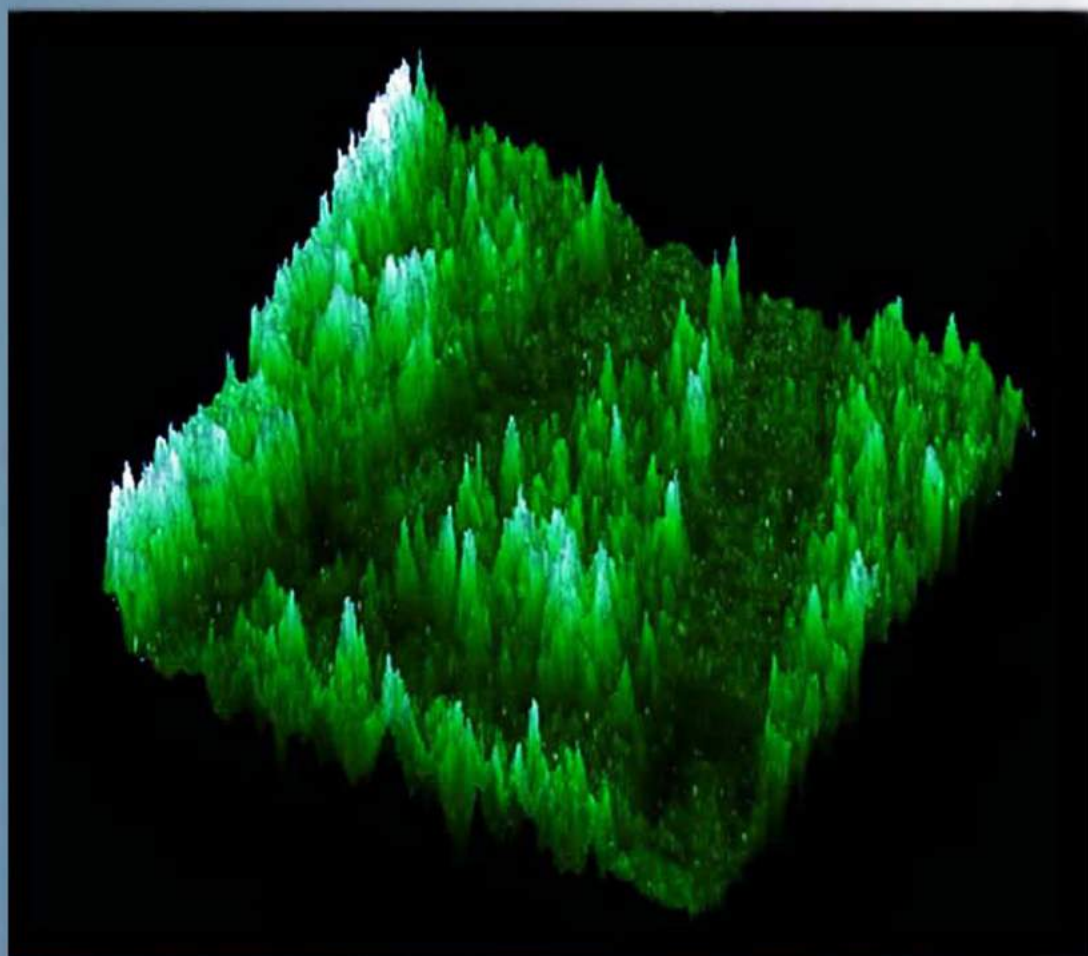
Section: En

April, 2020

# Azerbaijan Journal of Physics

# Fizika

[www.physics.gov.az](http://www.physics.gov.az)  
[jophphysics.wixsite.com/ajpphysics](http://jophphysics.wixsite.com/ajpphysics)



G.M. Abdullayev Institute of Physics  
Azerbaijan National Academy of Sciences  
Department of Physical, Mathematical and Technical Sciences

Published from 1995  
Ministry of Press and Information  
of Azerbaijan Republic,  
Registration number 514, 20.02.1995

**ISSN 1028-8546**  
vol. XXVI, Number 01, 2020  
Series: En

## *Azerbaijan Journal of Physics*

# *FIZIKA*

*G.M. Abdullayev Institute of Physics  
Azerbaijan National Academy of Sciences  
Department of Physical, Mathematical and Technical Sciences*

### **HONORARY EDITORS**

Arif PASHAYEV

### **EDITORS-IN-CHIEF**

Nazim MAMEDOV

Chingiz QAJAR

### **SENIOR EDITOR**

Talat MEHDIYEV

### **INTERNATIONAL REVIEW BOARD**

Ivan Scherbakov, Russia  
Kerim Allahverdiyev, Azerbaijan  
Mehmet Öndr Yetiş, Turkey  
Gennadii Jablonskii, Belarus  
Rafael Imamov, Russia  
Vladimir Man'ko, Russia  
Eldar Salayev, Azerbaijan  
Dieter Hochheimer, USA  
Victor L'vov, Israel

Vyacheslav Tuzlukov, South Korea  
Majid Ebrahim-Zadeh, Spain  
Anatoly Boreysho, Russia  
Mikhail Khalin, Russia  
Hasan Bidadi, Tebriz, Iran  
Natiq Atakishiyev, Mexico  
Tayar Djafarov, Azerbaijan  
Arif Hashimov, Azerbaijan  
Javad Abidinov, Azerbaijan

Bagadur Tagiyev, Azerbaijan  
Salima Mehdiyeva, Azerbaijan  
Talat Mehdiyev, Azerbaijan  
Ayaz Bayramov, Azerbaijan  
Tofiq Mammadov, Azerbaijan  
Shakir Nagiyev, Azerbaijan  
Rauf Guseynov, Azerbaijan  
Almuk Abbasov, Azerbaijan  
Yusif Asadov, Azerbaijan

### **TECHNICAL EDITORIAL BOARD**

Senior secretary: Elmira Akhundova; Nazli Huseynova, Gulnura Jafarova  
Nigar Akhundova, Elshana Aleskerova, Rena Nayimbayeva

### **PUBLISHING OFFICE**

131, H. Javid ave., AZ-1143, Baku  
ANAS, G.M. Abdullayev Institute of Physics

Tel.: (99412) 539-51-63, 539-32-23  
Fax: (99412) 537-22-92  
E-mail: [jophphysics@gmail.com](mailto:jophphysics@gmail.com)  
Internet: [www.physics.gov.az](http://www.physics.gov.az)  
<https://jophphysics.wixsite.com/ajpphysics>

Published at "AZERİ-DİZAYN"  
196, Nizami str., Baku  
Typographer: Filipp Podosinnikov

Sent for printing on: \_\_.\_\_. 201\_  
Printing approved on: \_\_.\_\_. 201\_  
Physical binding: \_\_\_\_\_  
Number of copies: \_\_\_\_\_ 200  
Order: \_\_\_\_\_

It is authorized for printing:

POLARIZATION EFFECTS AT HIGGS BOSON DECAY  $H \Rightarrow f\bar{f}\gamma$ 

S.K. ABDULLAEV, E.Sh. OMAROVA

23, Z. Khalilova str., Baku State University, Baku, Azerbaijan, AZ 1148

sabdullayev@bsu.edu.az

emiliya.abdullayeva@inbox.ru

In the framework of the Standard Model, the process of the radiation decay of Higgs boson into a fermion-antifermion pair was studied:  $H \Rightarrow f\bar{f}\gamma$ . Taking into account the spiralities of fermions and circular polarization of the  $\gamma$ -quanta an analytical expression is obtained for the decay width. The mechanisms of bremsstrahlung of a photon by a fermion pair, as well as fermion and  $W$ -boson loop diagrams, are considered in detail. The circular polarization of the  $\gamma$ -quanta was studied depending on the angle  $\theta$  and the invariant mass  $x$  of the fermion pair.

**Keywords:** Standard Model, Higgs boson, fermion pair, circular polarization, decay width.

**PACS:** 12.15-y, 12.15 Mm, 14.70 Hp, 14.80 Bn.

## 1. INTRODUCTION

The standard model (SM), based on the local gauge symmetry  $SU_C(3) \times SU_L(2) \times U_Y(1)$ , satisfactorily describes the strong and electroweak interactions of quarks, leptons, and gauge bosons [1, 2]. A doublet of scalar complex fields  $\varphi = \begin{pmatrix} \varphi^+ \\ \varphi^0 \end{pmatrix}$  is introduced into the theory, the neutral component of which has a non-zero vacuum value. As a result, the electroweak group  $SU_L(2) \times U_Y(1)$  spontaneously breaks down to the electromagnetic group  $U_Q(1)$ . In this case, three of the four components of the scalar field are absorbed by gauge bosons. The lagging fourth component of the scalar field is Higgs boson  $H$ . The standard Higgs boson was discovered by the ATLAS and CMS collaborations in 2012 at CERN at the Large Hadron Collider (LHC) [3, 4] (see reviews [5–7]) and this began a new stage of research to elucidate the nature of Higgs boson.

The standard Higgs boson can decay through different channels (see [1, 8]). One of the main channels of Higgs boson decay is the decay  $H \Rightarrow \gamma + \gamma$ ,  $H \Rightarrow \gamma + Z$  which was studied in [1, 8–10]. Along with these decay channels, much attention is also paid to the radiative decay  $H \Rightarrow f + \bar{f} + \gamma$ , where  $f\bar{f}$  is a pair of fundamental fermions (leptons, quarks) [11–15]. In these works, the decay width  $H \Rightarrow f + \bar{f} + \gamma$  was determined, the distribution of the fermion pair over the invariant mass, also the angular asymmetry of the front and back and the degrees of longitudinal and transverse polarizations of the fermions were studied. However, the circular polarization of the  $\gamma$ -quantum is not considered in these works.

The aim of this work is to study the circular polarization of a  $\gamma$ -quanta in decay

$$H \Rightarrow f + \bar{f} + \gamma, \quad (1)$$

where  $f\bar{f}$  is the fermion pair (lepton  $\tau^-\tau^+$  or quark  $c\bar{c}$ ,  $b\bar{b}$ , pair). In the framework of the SM, taking into account the longitudinal polarizations of the fermion pair and the circular polarization of the photon, an

analytical expression is obtained for the decay width. The dependence of the degree of circular polarization of a photon on the invariant mass of a fermion pair is studied in detail.

## 2. THE RADIATION OF PHOTON BY A FERMION PAIR

The radiation decay of the standard Higgs boson into a fermion pair is described by two types of Feynman diagrams which are shown in fig. 1. Diagrams a) and b) correspond to the bremsstrahlung of a photon by a fermion pair, and diagrams c), d), e), f) and g) are fermion and  $W$ -boson loop diagrams.

The amplitude corresponding to diagrams a) and b) of fig. 1 can be written as follows:

$$M_{i \rightarrow f} = i g_{Hff} e Q_f [\bar{u}_f(p_1, \lambda_1) R v_f(p_2, \lambda_2)], \quad (2)$$

where

$$R = \hat{e}^* \cdot \frac{\hat{p}_1 + \hat{k} + m_f}{(p_1 + k)^2 - m_f^2} - \frac{\hat{p}_2 + \hat{k} - m_f}{(p_2 + k)^2 - m_f^2} \cdot \hat{e}^*,$$

$g_{Hff} = m_f [\sqrt{2} G_F]^{1/2}$  is Higgs boson coupling constant with the fermion pair,  $m_f$  and  $Q_f$  is mass and charge of the fermion  $f$ ,  $e^*$  is 4-polarization vector of photon,  $p$ ,  $p_1$ ,  $p_2$  and  $k$  are 4-momenta of Higgs boson, fermion, antifermion and photon, respectively,  $\lambda_1$  and  $\lambda_2$  are spiralities of fermion and antifermion.

Applying the Dirac equations  $\bar{u}_f(p_1, \lambda_1)(\hat{p}_1 - m_f) = 0$ ,  $(\hat{p}_2 + m_f)v_f(p_2, \lambda_2) = 0$ , the amplitude (2) can be changed to:

$$M_{i \rightarrow f} = i A_0 [\bar{u}_f(p_1, \lambda_1) R v_f(p_2, \lambda_2)]. \quad (3)$$

Here

$$A_0 = - \frac{2\pi\alpha_{KED} m_f}{M_W \sin\theta_W}, \quad (4)$$

$$R = \frac{2(e^* \cdot p_1) + \hat{e}^* \hat{k}}{2(p_1 \cdot k)} - \frac{2(e^* \cdot p_2) + \hat{k} \hat{e}^*}{2(p_2 \cdot k)},$$

$M_W$  is the mass of  $W$ -boson,  $\theta_W$  is Weinberg angle.

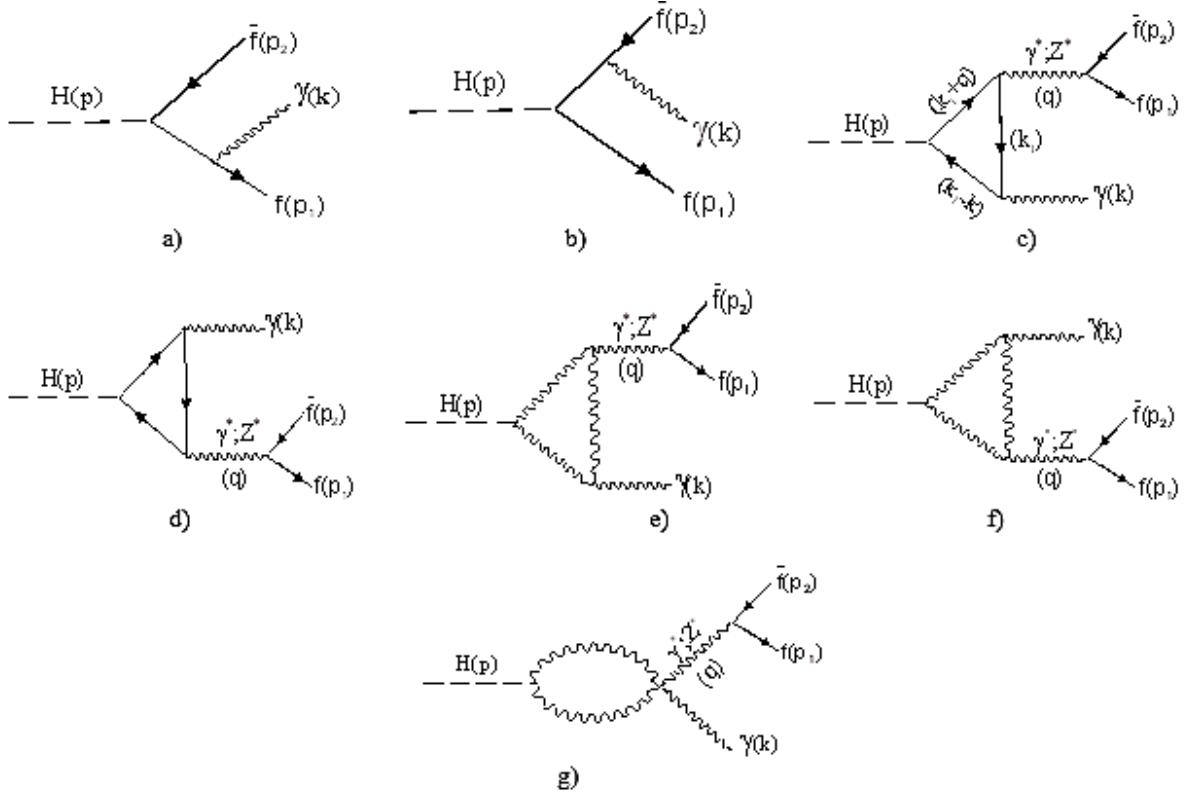


Fig. 1. Feynman diagrams for decay  $H \Rightarrow f \bar{f} \gamma$ .

The constant of interaction  $g_{Hff}$  increases when the mass of the fermion pair increases. Therefore, the decay of the standard Higgs boson with a mass of 125 GeV can produce fermion pairs  $\tau^- \tau^+$ ,  $c \bar{c}$  and  $b \bar{b}$ . Due to the small mass  $m_f$ , the decay channels  $H \Rightarrow e^- + e^+ + \gamma$ ,  $H \Rightarrow \mu^- + \mu^+ + \gamma$ ,  $H \Rightarrow u + \bar{u} + \gamma$ ,  $H \Rightarrow d + \bar{d} + \gamma$  and  $H \Rightarrow s + \bar{s} + \gamma$  are suppressed. The study of the radiative decay of  $H \Rightarrow \tau^- + \tau^+ + \gamma$  shows particular interest, since the decay channels of  $\tau^- \Rightarrow \pi^- + \nu_\tau$ ,  $\tau^- \Rightarrow K^- + \nu_\tau$ ,  $\tau^- \Rightarrow \rho^- + \nu_\tau$ , decay make it possible to measure the polarization of the  $\tau$ -lepton. In addition, in the decay of  $H \Rightarrow \tau^- + \tau^+ + \gamma$ , a photon can acquire circular polarization, the

measurement of which is a source of additional information about the standard Higgs boson.

Note that in the radiation decays of Higgs boson  $\Rightarrow \tau^- + \tau^+ + \gamma$ ,  $H \Rightarrow c + \bar{c} + \gamma$  and  $H \Rightarrow b + \bar{b} + \gamma$  the ratios are  $\frac{m_f^2}{M_H^2} = 0,0002 \ll 1$ ,  $\frac{m_c^2}{M_H^2} = 0,00017 \ll 1$ , and  $\frac{m_b^2}{M_H^2} = 0,00015 \ll 1$ . Therefore, we can neglect the terms, which are proportional to  $\frac{m_f^2}{M_H^2}$ . In this case, on the basis of amplitude (3) for the decay width  $H \Rightarrow f + \bar{f} + \gamma$ , the following expression is obtained (in the system of the center of mass of the fermion pair  $\vec{p}_1 + \vec{p}_2 = \vec{q} = 0$ ):

$$\frac{d\Gamma}{dx dz} = \frac{A_0^2 M_H v}{2^{10} \pi^3 (1-x)} \cdot \frac{N_C}{(1-v^2 z^2)^2} \times \{ (1 + \lambda_1 \lambda_2) (1 + x^2) (1 - v^2 z^2) + s_\gamma (\lambda_1 + \lambda_2) (1 - x) [2x v^2 (1 - z^2) + (1 - x) (1 - v^2 z^2)] \}. \quad (5)$$

Here  $s_\gamma = \pm 1$ , it characterizes the circular polarization of the photon (for  $s_\gamma = +1$  the photon has right circular polarization, and for  $s_\gamma = -1$  has the left one),  $z = \cos \theta$ ,  $\theta$  is the angle between the directions of Higgs boson and fermion momenta,  $x$  determines the invariant mass of the fermion pair in units of  $M_H^2$ :

$$x = \frac{q^2}{M_H^2} = \frac{s}{M_H^2} = \frac{(p_1 + p_2)^2}{M_H^2},$$

$v = \sqrt{1 - \frac{4m_f^2}{s}}$  is helicity of fermion,  $N_C$  is color factor (for the lepton pair  $N_C = 1$ , and for the quark pair

$N_C = 3$ ).

From the decay width (5) of  $H \Rightarrow f + \bar{f} + \gamma$  it follows that the fermion and antifermion must have the same spiralities:  $\lambda_1 = \lambda_2 = \pm 1$  ( $f_L \bar{f}_L$  or  $f_R \bar{f}_R$ , where  $f_L$  and  $f_R$  are the left and right fermions). This is due to the conservation of the total moment in the  $H \Rightarrow f + \bar{f}$  transition. The decay width (5) also shows that when a longitudinally polarized fermion pair is produced, the emitted photon acquires circular polarization.

We determine the degree of circular polarization of the  $\gamma$ -quanta in the standard way:

$$P_\gamma = \frac{d\Gamma(\lambda_1; s_\gamma=+1)/dx dz - d\Gamma(\lambda_1; s_\gamma=-1)/dx dz}{d\Gamma(\lambda_1; s_\gamma=+1)/dx dz + d\Gamma(\lambda_1; s_\gamma=-1)/dx dz} = \lambda_1 \cdot \frac{(1-x)[2xv^2(1-z^2) + (1-x)(1-v^2z^2)]}{(1+x^2)(1-v^2z^2)} \quad (6)$$

Figure 2 shows the angular dependence of the degree of circular polarization of the photon for various invariant masses of the  $\tau^-\tau^+$  lepton pair:  $x=0,102$ ;  $x=0,23$  and  $x=0,518$ . It can be seen that for the values of the cosines of the angle  $0 \leq z \leq 0,9$ , the degree of circular polarization of the photon in the  $H \Rightarrow \tau^-\tau^+ + \gamma$  process is almost constant, and for  $0,9 < z \leq 1$ , with increasing cosines of the angle  $\theta$ , the degree of circular polarization of the photon decreases. An increase in the energy  $x$  carried away by the  $\tau^-\tau^+$  lepton pair leads to a decrease in the degree of circular polarization of the photon.

Figure 3 illustrates the dependence of the degree of circular polarization of a photon in the  $H \Rightarrow \tau^-\tau^+ + \gamma$  decay on the invariant mass  $x$  at  $z=0$  and  $z=1$ . As can be seen, with an increase in the energy  $x$  carried away by the lepton pair  $\tau^-\tau^+$ , the degree of circular polarization of the photon monotonically decreases and vanishes at the end of the spectra (for  $x=1$ ).

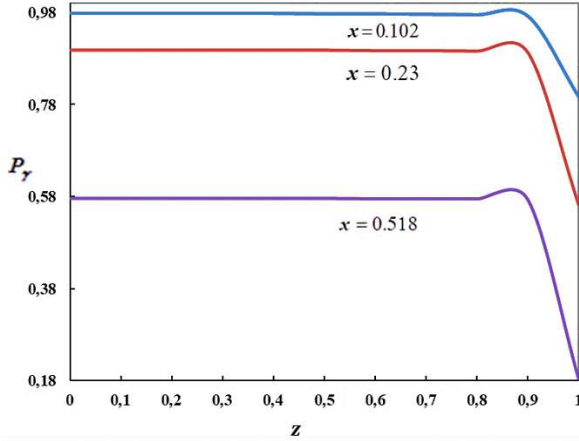


Fig. 2. Angular dependence of the degree of circular polarization of a photon in the  $H \Rightarrow \tau^-\tau^+\gamma$  decay at  $\lambda_1 = +1$ .

$$\frac{d\Gamma}{dx} = \frac{A_0^2 M_H v}{2^{10} \pi^3} \cdot \frac{N_C}{1-x} \{ (1 + \lambda_1 \lambda_2)(1 + x^2) \cdot L + s_\gamma (\lambda_1 + \lambda_2)(1 - x)[-2x + (1 + xv^2)L] \}, \quad (8)$$

where

$$L = \frac{1}{v} \ln \frac{1+v}{1-v}.$$

The degree of circular polarization of the photon integrated over the particle angles  $\theta$  is determined by the formula:

$$P_\gamma = \lambda_1 \cdot \frac{(1-x)[-2x + (1+xv^2)L]}{(1+x^2)L} \quad (9)$$

Figure 5 shows the energy dependence of the degree of circular polarization of the photon in the  $H \Rightarrow \tau^-\tau^+ + \gamma$  decay at  $M_H = 125$  GeV,  $m_\tau = 1.778$  GeV. With increasing  $x$ , the degree of circular polarization of the photon decreases.

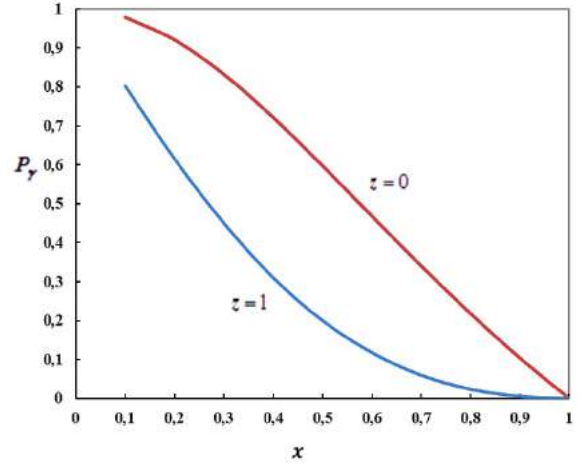


Fig. 3. Dependence of the degree of circular polarization of a photon in the  $H \Rightarrow \tau^-\tau^+\gamma$  decay on the invariant mass  $x$  for  $\lambda_1 = +1$ .

The decay width  $H \Rightarrow f + \bar{f} + \gamma$ , summed over the polarization states of the photon and fermion pair, is given by:

$$\frac{d\Gamma}{dx dz} = \frac{A_0^2 M_H N_C v}{128 \pi^3 (1-v^2 z^2)} \cdot \frac{1+x^2}{1-x}. \quad (7)$$

In fig. 4 shows the dependence of the decay width  $H \Rightarrow \tau^-\tau^+ + \gamma$  on the invariant mass  $x$  at  $M_H = 125$  GeV,  $m_\tau = 1.778$  GeV,  $M_W = 80.385$  GeV,  $\sin^2 \theta_W = 0.2315$  and various values of the cosines of the angle  $\theta$ :  $z=0$ ;  $z=0.5$ . As can be seen, with an increase in the invariant mass  $x$ , the decay width  $H \Rightarrow \tau^-\tau^+ + \gamma$  increases, a decrease in the exit angle  $\theta$  leads to an increase in the decay width.

Integrating (5) over the particle exit angles  $\theta$ , for the decay width  $H \Rightarrow f + \bar{f} + \gamma$  we find the following expression that determines the distribution of the fermion pair over the invariant mass  $x$ :

Figure 5 shows the energy dependence of the degree of circular polarization of the photon in the  $H \Rightarrow \tau^-\tau^+ + \gamma$  decay at  $M_H = 125$  GeV,  $m_\tau = 1.778$  GeV. With increasing  $x$ , the degree of circular polarization of the photon decreases.

The decay width  $H \Rightarrow f + \bar{f} + \gamma$ , which characterizes the distribution of the fermion pair over the invariant mass  $x$  without taking into account the polarizations of the particles, is determined by the expression:

$$\frac{d\Gamma}{dx} = \frac{A_0^2 M_H N_C}{128 \pi^3} \cdot \frac{1+x^2}{1-x} \ln \left( \frac{1+v}{1-v} \right). \quad (10)$$



Figure 6 illustrates the dependence of the  $H \Rightarrow \tau^- \tau^+ + \gamma$  decay width on the invariant mass  $x$  at  $M_H = 125$  GeV. With an increase in the fraction of energy carried away by the  $\tau^- \tau^+$  lepton pair, the  $H \Rightarrow \tau^- \tau^+ + \gamma$  decay width increases.

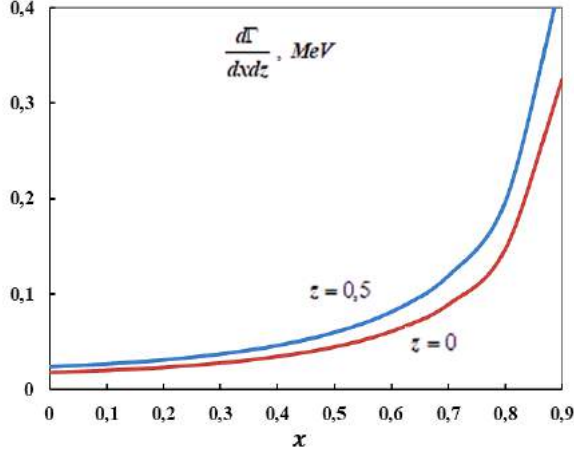


Fig. 4. Dependence of the decay width  $H \Rightarrow \tau^- \tau^+ \gamma$  on the invariant mass  $x$ .

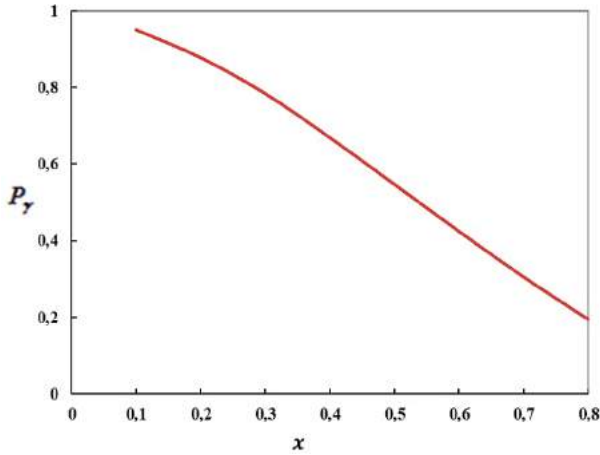


Fig. 5. The dependence of the circular polarization of the photon on  $x$  in the decay of  $H \Rightarrow \tau^- \tau^+ \gamma$  at  $\lambda_1 = +1$

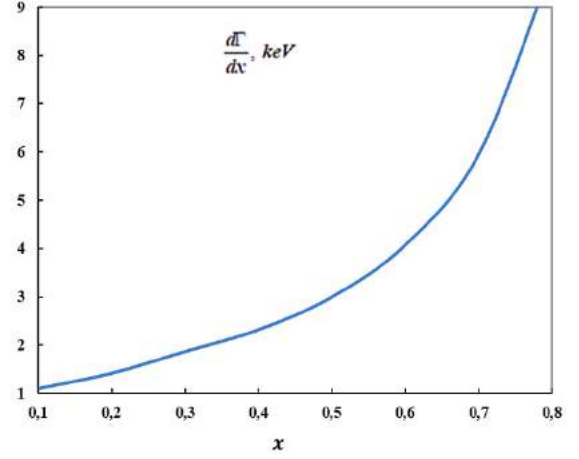


Fig. 6. Dependence of the  $H \Rightarrow \tau^- \tau^+ \gamma$  decay width on the invariant mass  $x$

### 3. Fermion and $W$ - boson loop diagrams

The amplitude corresponding to the bremsstrahlung of the photon by the fermion and antifermion (diagrams a) and b) in fig. 1) is proportional to the mass of the fermion  $m_f$ , therefore, the contribution of fermion and  $W$  -boson loop diagrams to Higgs decay of the  $H \Rightarrow f + \bar{f} + \gamma$  boson can be significant. Typical single-loop Feynman diagrams are shown in fig. 1 (diagrams c), d), e), f) and g)). They are the photon and  $Z$  -boson pole diagrams of the  $H \Rightarrow \gamma + \gamma^* \Rightarrow \gamma + f + \bar{f}$  and  $H \Rightarrow \gamma + Z^* \Rightarrow \gamma + f + \bar{f}$  decays.

The single-loop Feynman diagrams shown in fig. 1 are crucial for the radiation production of a light fermion pair  $H \Rightarrow e^- + e^+ + \gamma$ ,  $H \Rightarrow u + \bar{u} + \gamma$ , etc. We proceed to calculate the amplitude corresponding to these diagrams. The amplitude corresponding to fermion loop diagrams is written as:

$$M = i g_{Hff} \int \frac{d^4 k_1}{(2\pi)^4} \cdot \frac{Sp[\gamma_\mu (\hat{k}_1 + \hat{q} + m)(\hat{k}_1 - \hat{k} + m)\gamma_\nu (\hat{k}_1 + m)]}{(k_1^2 - m^2)[(k_1 + q)^2 - m^2][(k_1 - k)^2 - m^2]} \cdot e_\nu^* \times \frac{g_{\mu\rho}}{q^2} [\bar{u}(p_1)\gamma_\rho v(p_2)], \quad (11)$$

where  $m$  is the mass of the loop fermion.

Using the Feynman integration technique, we can carry out integration over the 4 - momenta  $k_1$ , as a result, we have the amplitude:

$$M_{LOOP}^{(fermion)} = M_1 + M_2, \quad (12)$$

$$M_1 = (e^* \cdot q) \bar{u}(p_1, \lambda_1) [A_1 \hat{k} + A_2 \hat{k} \gamma_5] v(p_2, \lambda_2) - (k \cdot q) \bar{u}(p_1, \lambda_1) [A_1 \hat{e}^* + A_2 \hat{e}^* \gamma_5] v(p_2, \lambda_2),$$

$$M_2 = -i(\mu e^* k q)_\varepsilon \bar{u}(p_1, \lambda_1) [A_3 \gamma_\mu + A_4 \gamma_\mu \gamma_5] v(p_2, \lambda_2), \quad (13)$$

where

$$A_1 = g_V(f) D_Z(s) P_{syz} - \frac{1}{s} P_{\gamma\gamma}, \quad A_2 = g_A(f) D_Z(s) P_{syz}, \quad (14)$$

$$A_3 = g_V(f) D_Z(s) P_{ayz}, \quad A_4 = g_A(f) D_Z(s) P_{ayz}$$

$$D_Z(s) = (s - M_Z^2 + i M_Z \Gamma_Z)^{-1}, \quad (\mu e^* k q)_\varepsilon = \varepsilon_{\mu\nu\rho\sigma} e_\nu^* k_\rho q_\sigma,$$

$$\begin{aligned}
 g_V(f) &= \frac{T_f - 2Q_f \sin^2 \theta_W}{2 \sin \theta_W \cos \theta_W}, \quad g_A(f) = \frac{T_f}{2 \sin \theta_W \cos \theta_W}, \\
 P_{\gamma Z} &= \frac{\alpha_{KED}^2}{M_W \sin \theta_W} \cdot \frac{N_C e_f I_f}{\sin \theta_W \cos \theta_W} A_{f_2}(\tau_f, \lambda_f), \\
 P_{\gamma \gamma} &= \frac{\alpha_{KED}^2}{M_W \sin \theta_W} \left( -2N_C \frac{I_f - 2e_f \sin^2 \theta_W}{\sin \theta_W \cos \theta_W} A_{f_1}(\tau_f, \lambda_f) \right), \\
 P_{\gamma \gamma} &= \frac{\alpha_{KED}^2}{M_W \sin \theta_W} \cdot (-4N_C) \cdot e_f^2 A_{f_1}(\tau_f, \lambda_f),
 \end{aligned} \tag{15}$$

$$\begin{aligned}
 A_{f_1}(\tau, \lambda) &= I_1(\tau, \lambda) - I_2(\tau, \lambda), \\
 A_{f_2}(\tau, \lambda) &= \frac{\tau \lambda}{\lambda - \tau} [2g(\tau) - 2g(\lambda) + f(\tau) - f(\lambda)], \\
 I_1(\tau, \lambda) &= \frac{\tau \lambda}{2(\tau - \lambda)} + \frac{\tau^2 \lambda^2}{2(\tau - \lambda)^2} [f(\tau) - f(\lambda)] + \frac{\tau^2 \lambda}{(\tau - \lambda)^2} [g(\tau) - g(\lambda)], \\
 I_2(\tau, \lambda) &= -\frac{\tau \lambda}{2(\tau - \lambda)} [f(\tau) - f(\lambda)],
 \end{aligned} \tag{16}$$

and the functions  $f(\tau)$  and  $g(\tau)$  are equal:

$$\begin{aligned}
 f(\tau) &= \begin{cases} \arcsin^2 \frac{1}{\sqrt{\tau}} & \tau \geq 1 \\ -\frac{1}{4} \left[ \ln \frac{1+\sqrt{1-\tau}}{1-\sqrt{1-\tau}} - i\pi \right]^2 & \tau < 1 \end{cases}, \\
 g(\tau) &= \begin{cases} \sqrt{\tau-1} \arcsin \frac{1}{\sqrt{\tau}} & \tau \geq 1 \\ \frac{1}{2} \sqrt{1-\tau} \left[ \ln \frac{1+\sqrt{1-\tau}}{1-\sqrt{1-\tau}} - i\pi \right] & \tau < 1 \end{cases},
 \end{aligned} \tag{17}$$

$\tau$  and  $\lambda$  are given by the relations:

$$\tau = \frac{4m^2}{M_H^2}, \quad \lambda = \frac{4m^2}{s}.$$

Here  $e_f$  and  $I_f$  are the charge and the third projection of the weak isospin of the loop fermion;  $g_V(f)$  and  $g_A(f)$  are the vector and axial-vector coupling constants of fermion  $f$ ;  $M_Z$  and  $\Gamma_Z$  are the mass and total decay width of the  $Z$  boson;  $T_f$  is the third projection of the weak isospin of fermion  $f$ , in the case of a  $t$ -quark loop we have:  $\tau = \frac{4m^2}{M_H^2} > 1$ ,

$$\lambda = \frac{4m^2}{s} > 1.$$

In the unitary gauge there are only three  $W$ -boson loop diagrams d), e) and f). Taking into account all the loop diagrams in Fig. 1, the decay amplitude of  $H \Rightarrow f + \bar{f} + \gamma$  is determined by expression (12), but the expressions  $P_{\gamma Z}$  and  $P_{\gamma \gamma}$  change, they contain the contributions of both fermion and  $W$ -boson loop diagrams:

$$\begin{aligned}
 P_{\gamma Z} &= \frac{\alpha_{KED}^2}{M_W \sin \theta_W} \left[ -ctg \theta_W A_W(\tau_W, \lambda_W) - 2N_C e_f \frac{I_f - 2e_f \sin^2 \theta_W}{\sin \theta_W \cos \theta_W} A_{f_1}(\tau_f, \lambda_f) \right], \\
 P_{\gamma \gamma} &= \frac{\alpha_{KED}^2}{M_W \sin \theta_W} \cdot [-A_W(\tau_W, \lambda_W) - 4N_C e_f^2 A_{f_1}(\tau_f, \lambda_f)], \\
 A_W(\tau, \lambda) &= \left[ \left(1 + \frac{2}{\tau}\right) \left(\frac{4}{\lambda} - 1\right) - \left(5 + \frac{2}{\tau}\right) \right] I_1(\tau, \lambda) + 16 \left(1 - \frac{1}{\lambda}\right) I_2(\tau, \lambda).
 \end{aligned} \tag{18}$$

The square of the  $H \Rightarrow f + \bar{f} + \gamma$  decay amplitude, corresponding to fermion and  $W$ -boson loop diagrams, in the general case, has a complex structure and is given in the Appendix. However, in

the center-of-mass system of a fermion pair ( $\vec{q} = \vec{p}_1 + \vec{p}_2 = 0$ ), the square of Higgs boson decay amplitude is greatly simplified:

$$\begin{aligned}
 |M_{LOOP}|^2 &= |M_1|^2 + |M_2|^2 + M_1^* M_2 + M_2^* M_1, \\
 |M_1|^2 &= \frac{(M_H^2 - s)^2}{16} s \{ (1 - \lambda_1 \lambda_2) [(|A_1|^2 + |A_2|^2)(1 + v^2 z^2) + 4 \text{Re}(A_1 A_2^*) s_\gamma v z] + \\
 &\quad + (\lambda_2 - \lambda_1) [(|A_1|^2 + |A_2|^2) \cdot 2s_\gamma v z + 2 \text{Re}(A_1 A_2^*)(1 + v^2 z^2)] \},
 \end{aligned} \tag{19}$$

$$\begin{aligned}
 |M_2|^2 &= \frac{(M_H^2 - s)^2}{16} s \{ (1 - \lambda_1 \lambda_2) [ (|A_3|^2 + |A_4|^2)(1 + v^2 z^2) + 4 \operatorname{Re}(A_3 A_4^*) s_\gamma v z ] + \\
 &\quad + (\lambda_2 - \lambda_1) [ (|A_3|^2 + |A_4|^2) \cdot 2 s_\gamma v z + 2 \operatorname{Re}(A_3 A_4^*) (1 + v^2 z^2) ] \}, \\
 M_1^* M_2 + M_2^* M_1 &= \frac{(M_H^2 - s)^2}{16} s \{ (1 - \lambda_1 \lambda_2) [ 2 \operatorname{Re}(A_1 A_3^* + A_2 A_4^*) s_\gamma (1 + v^2 z^2) + \\
 &\quad + 4 \operatorname{Re}(A_1 A_4^* + A_2 A_3^*) v z ] + (\lambda_2 - \lambda_1) [ 4 \operatorname{Re}(A_1 A_3^* + A_2 A_4^*) v z + \\
 &\quad + 2 \operatorname{Re}(A_1 A_4^* + A_2 A_3^*) s_\gamma (1 + v^2 z^2) ] \}. \tag{20}
 \end{aligned}$$

The differential decay width  $H \Rightarrow f + \bar{f} + \gamma$ , containing the contribution of fermion and  $W$  boson loop diagrams, can be written in the form:

$$\begin{aligned}
 \frac{d\Gamma}{dx dz} &= \frac{(M_H^2 - s)^3}{2^{11} \pi^3 M_H} s v \{ (1 - \lambda_1 \lambda_2) [ (|A_1|^2 + |A_2|^2 + |A_3|^2 + |A_4|^2)(1 + v^2 z^2) + \\
 &\quad + 4 \operatorname{Re}(A_1 A_2^* + A_3 A_4^*) s_\gamma v z + 2 \operatorname{Re}(A_1 A_3^* + A_2 A_4^*) s_\gamma (1 + v^2 z^2) + 4 \operatorname{Re}(A_1 A_4^* + A_2 A_3^*) v z ] + \\
 &\quad + (\lambda_2 - \lambda_1) [ (|A_1|^2 + |A_2|^2 + |A_3|^2 + |A_4|^2) 2 s_\gamma v z + 2 \operatorname{Re}(A_1 A_2^* + A_3 A_4^*) (1 + v^2 z^2) + \\
 &\quad + 2 \operatorname{Re}(A_1 A_4^* + A_2 A_3^*) s_\gamma (1 + v^2 z^2) + 4 \operatorname{Re}(A_1 A_3^* + A_2 A_4^*) v z ] \}, \tag{21}
 \end{aligned}$$

It follows from the decay width (21) that the fermion and antifermion should have opposite spiralities:  $\lambda_1 = -\lambda_2 = \pm 1$  ( $f_R \bar{f}_L$  or  $f_L \bar{f}_R$ , where  $f_L(\bar{f}_L)$  and  $f_R(\bar{f}_R)$  are the right and left-polarized fermion (antifermion)). This is due to the preservation of the full moment in the transitions  $\gamma^* \Rightarrow f + \bar{f}$  and  $Z^* \Rightarrow f + \bar{f}$ .

As noted in the previous section, when a photon is emitted by a fermion pair, the fermion and antifermion must have the same spiralities  $\lambda_1 = \lambda_2 = \pm 1$  ( $f_R \bar{f}_R$  or  $f_L \bar{f}_L$ ). Thus, by the spiral properties of

the fermion pair, we can separate the contribution of the loop diagrams to the decay width from the contribution of bremsstrahlung. At  $\lambda_1 = -\lambda_2 = \pm 1$ , the contribution to the decay amplitude of the  $H \Rightarrow f + \bar{f} + \gamma$  diagrams of bremsstrahlung vanishes, and at  $\lambda_1 = \lambda_2 = \pm 1$ , on the contrary, the contribution of the loop diagrams vanishes.

Let us consider some particular cases of the decay width (21). We summarize the decay width according to the polarization states of the fermion pair:

$$\begin{aligned}
 \frac{d\Gamma}{dx dz} &= \frac{(M_H^2 - s)^3}{2^9 \pi^3 M_H} s v \{ [ |A_1|^2 + |A_2|^2 + |A_3|^2 + |A_4|^2 ] (1 + v^2 z^2) + 4 \operatorname{Re}(A_1 A_2^* + A_3 A_4^*) s_\gamma v z + \\
 &\quad + 4 \operatorname{Re}(A_1 A_4^* + A_2 A_3^*) v z + 2 \operatorname{Re}(A_1 A_3^* + A_2 A_4^*) s_\gamma (1 + v^2 z^2) \}. \tag{22}
 \end{aligned}$$

Using the standard formula, we determine the degree of circular polarization of a photon in  $H \Rightarrow f + \bar{f} + \gamma$  decay:

$$\begin{aligned}
 P_\gamma(s, z) &= \frac{d\Gamma(s_\gamma=+1)/dx dz - d\Gamma(s_\gamma=-1)/dx dz}{d\Gamma(s_\gamma=+1)/dx dz + d\Gamma(s_\gamma=-1)/dx dz} = \\
 &= \frac{2 \operatorname{Re}(A_1 A_3^* + A_2 A_4^*) (1 + v^2 z^2) + 4 \operatorname{Re}(A_1 A_2^* + A_3 A_4^*) v z}{[ |A_1|^2 + |A_2|^2 + |A_3|^2 + |A_4|^2 ] (1 + v^2 z^2) + 4 \operatorname{Re}(A_1 A_4^* + A_2 A_3^*) v z}. \tag{23}
 \end{aligned}$$

After summing the decay width (21) over the polarization states of the antifermion and photon, we have:

$$\begin{aligned}
 \frac{d\Gamma}{dx dz} &= \frac{(M_H^2 - s)^3}{2^9 \pi^3 M_H} s v \{ [ |A_1|^2 + |A_2|^2 + |A_3|^2 + |A_4|^2 ] (1 + v^2 z^2) + 4 \operatorname{Re}(A_1 A_4^* + A_2 A_3^*) v z - \\
 &\quad - \lambda_1 [ 2 \operatorname{Re}(A_1 A_2^* + A_3 A_4^*) (1 + v^2 z^2) + 4 \operatorname{Re}(A_1 A_3^* + A_2 A_4^*) v z ] \}. \tag{24}
 \end{aligned}$$

The degree of longitudinal polarization of the fermion is determined in the standard way:

$$\begin{aligned}
 P_f(s, z) &= \frac{d\Gamma(\lambda_1=+1)/dx dz - d\Gamma(\lambda_1=-1)/dx dz}{d\Gamma(\lambda_1=+1)/dx dz + d\Gamma(\lambda_1=-1)/dx dz} = \\
 &= - \frac{2 \operatorname{Re}(A_1 A_2^* + A_3 A_4^*) (1 + v^2 z^2) + 4 \operatorname{Re}(A_1 A_3^* + A_2 A_4^*) v z}{[ |A_1|^2 + |A_2|^2 + |A_3|^2 + |A_4|^2 ] (1 + v^2 z^2) + 4 \operatorname{Re}(A_1 A_4^* + A_2 A_3^*) v z}. \tag{25}
 \end{aligned}$$



The differential decay width  $H \Rightarrow f + \bar{f} + \gamma$ , containing the contribution of the loop diagrams, has the form:

$$\frac{d\Gamma}{dx dz} = \frac{(M_H^2 - s)^3}{2^8 \pi^3 M_H} s v \{ [|A_1|^2 + |A_2|^2 + |A_3|^2 + |A_4|^2] (1 + v^2 z^2) + 4 \text{Re}(A_1 A_4^* + A_2 A_3^*) v z \} \quad (26)$$

Due to the second term proportional to  $z$ , angular asymmetry occurs back and forth, defined as

$$A_{FB}(s) = \frac{\int_0^1 \frac{d\Gamma}{dx dz} dz - \int_{-1}^0 \frac{d\Gamma}{dx dz} dz}{\int_0^1 \frac{d\Gamma}{dx dz} dz + \int_{-1}^0 \frac{d\Gamma}{dx dz} dz} = \frac{12 \text{Re}(A_1 A_4^* + A_2 A_3^*) v}{[|A_1|^2 + |A_2|^2 + |A_3|^2 + |A_4|^2] (3 + v^2)}. \quad (27)$$

Integrating the decay width (21) over the polar angle  $\theta$  we have:

$$\begin{aligned} \frac{d\Gamma}{dx} = \frac{(M_H^2 - s)^3 s v}{2^{10} \pi^3 M_H} \left(1 + \frac{v^2}{3}\right) \{ (1 - \lambda_1 \lambda_2) [ |A_1|^2 + |A_2|^2 + |A_3|^2 + |A_4|^2 ] + \\ + 2 \text{Re}(A_1 A_3^* + A_2 A_4^*) s_\gamma \} + (\lambda_2 - \lambda_1) [ 2 \text{Re}(A_1 A_2^* + A_3 A_4^*) + 2 \text{Re}(A_1 A_4^* + A_2 A_3^*) s_\gamma \}. \end{aligned} \quad (28)$$

It follows that the non-zero  $\text{Re}(A_1 A_3^* + A_2 A_4^*)$  and  $\text{Re}(A_1 A_2^* + A_3 A_4^*)$  expressions give rise to the degree of circular polarization of the photon and the degree of longitudinal polarization of the fermion:

$$P_\gamma(s) = \frac{2 \text{Re}(A_1 A_3^* + A_2 A_4^*)}{|A_1|^2 + |A_2|^2 + |A_3|^2 + |A_4|^2}, \quad (29)$$

$$P_f(s) = - \frac{2 \text{Re}(A_1 A_2^* + A_3 A_4^*)}{|A_1|^2 + |A_2|^2 + |A_3|^2 + |A_4|^2}. \quad (30)$$

We obtained expressions for the degree of circular polarization of the photon  $P_\gamma(s, z)$  and  $P_\gamma(s)$ , for the degree of longitudinal polarization of the fermion  $P_f(s, z)$  and  $P_f(s)$ , and also for the forward-backward angular asymmetry  $A_{FB}(s)$ . Let us estimate them in the  $H \Rightarrow \gamma + e^- + e^+$  decay, where the main Feynman diagrams are fermion and  $W$ -boson loop diagrams, and the bremsstrahlung diagrams are suppressed. The following parameters were used in the calculations:  $M_H = 125$  GeV,  $m_t = 173.2$  GeV,  $m_e = 0.51 \cdot 10^{-3}$  GeV,  $M_Z = 91.1875$  GeV,  $\Gamma_Z = 2.4952$  GeV,  $M_W = 80.385$  GeV,  $x_W = 0.2315$ . It is assumed that particle loops are  $t$ -quark and the  $W$ -boson.

Figure 7 shows the dependence of the degree of circular polarization of the photon on the invariant mass  $\sqrt{s}$  at various angles  $\theta$ .

As can be seen, at  $\theta = 30^\circ$  the degree of circular polarization of the photon is negative, with an increase in the energy of the fermion pair it decreases and reaches a minimum near  $\sqrt{s} = 80$  GeV, and a further increase in energy leads to an increase in the degree of circular polarization of the photon. With increasing fermion emission angle, the degree of circular polarization of the photon module decreases. At  $\theta = 90^\circ$  the degree of circular polarization is zero.

Figure 8 illustrates the angular dependence of the degree of circular polarization of a photon at various  $\sqrt{s}$ .

It follows from the figure that at the fermion pair

energy  $\sqrt{s} = M_Z$ , the degree of circular polarization of the photon is positive and decreases monotonically from 0.422 to 0.154 with increasing polar  $\theta$  angle from zero to  $180^\circ$ . However, at an energy  $\sqrt{s} = 80$  GeV, the degree of circular polarization of the photon at the beginning of the angular spectrum is negative, increases monotonically with increasing angle  $\theta$  and vanishes near  $90^\circ$ , and then the degree of circular polarization of the photon becomes positive and reaches a maximum at the end of the angular spectrum.

At an energy  $\sqrt{s} = 40$  GeV, a similar dependence is also observed, however, the numerical value of  $P_\gamma(s, z)$  is small and varies within the range of  $-0.051 \leq P_\gamma(s, z) \leq 0.051$ .

Figure 9 illustrates the angular dependence of the degree of longitudinal polarization of an electron  $P_e(s, z)$  at various energies  $\sqrt{s}$ .

The graph shows that for  $\sqrt{s} = M_Z$  at the beginning of the angular spectrum, the degree of longitudinal polarization of the electron is negative and monotonically increases from  $-0.422$  to  $0.154$  with increasing angle  $\theta$ .

At  $\sqrt{s} = 80$  GeV (40 GeV), the degree of longitudinal polarization of the electron does not depend on the angle  $\theta$  and contain 58.6% (5.1%).

As for the angular asymmetry of the forward and backward  $A_{FB}(s)$ , we note that in the  $H \Rightarrow e^- + e^+ + \gamma$  decay this asymmetry due to  $\text{Re}(A_1 A_4^* + A_2 A_3^*) \Rightarrow 0$  is equal to zero.

Figure 10 shows the dependence of the degree of circular polarization of the photon  $P_\gamma(s)$  and the degree of longitudinal polarization of the electron  $P_e(s)$  on the invariant mass  $\sqrt{s}$ . Due to  $\text{Re}(A_1 A_3^* + A_2 A_4^*) = 0$ , the degree of circular polarization is  $P_\gamma(s) = 0$ .

However, with an increase in the invariant mass of the  $e^- e^+$  pair, the degree of longitudinal polarization of the electron increases and reaches a maximum near  $\sqrt{s} = 80$  GeV, a further increase in the invariant mass leads to a decrease in the degree of longitudinal polarization of the electron.

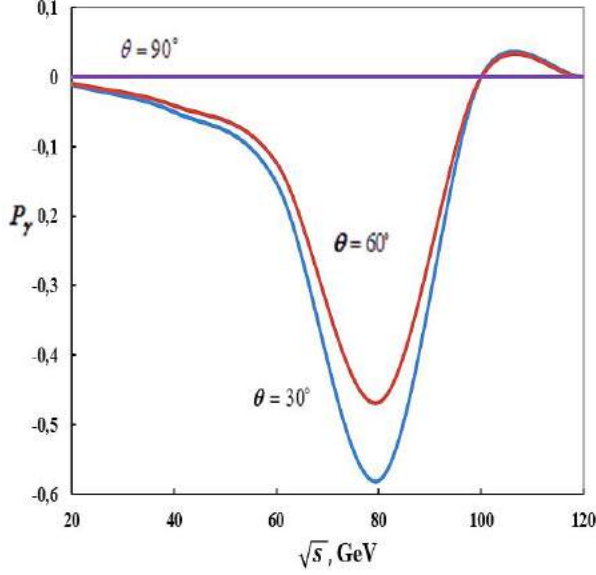


Fig. 7. The degree of circular polarization of photon in  $H \Rightarrow e^- + e^+ + \gamma$  decay as a function of  $\sqrt{s}$ .

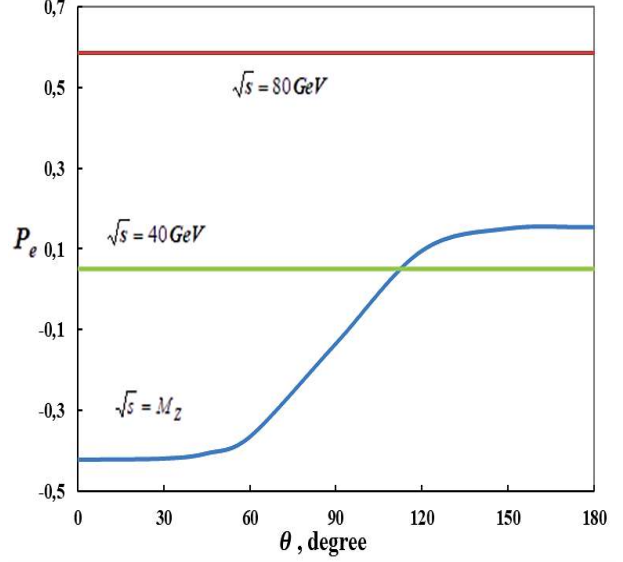


Fig. 9. Angular dependence of the degree of longitudinal polarization of electron  $P_e(s, z)$  at various energies  $\sqrt{s} = M_Z$ .

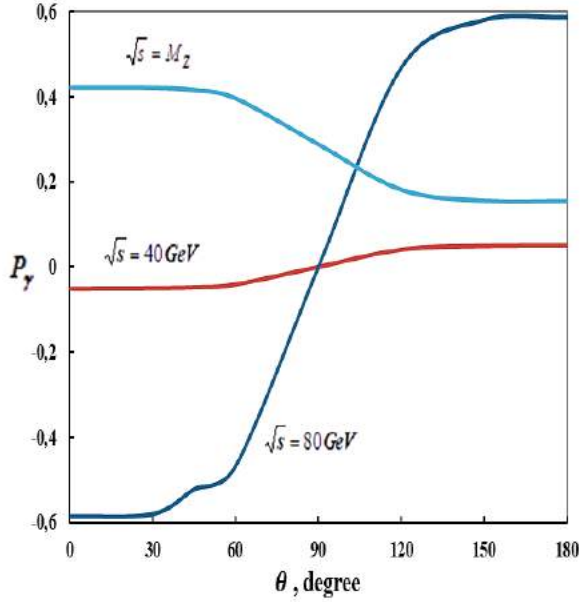


Fig. 8. Angular dependence  $P_\gamma(s, z)$  in decay  $H \Rightarrow e^- e^+ \gamma$ .

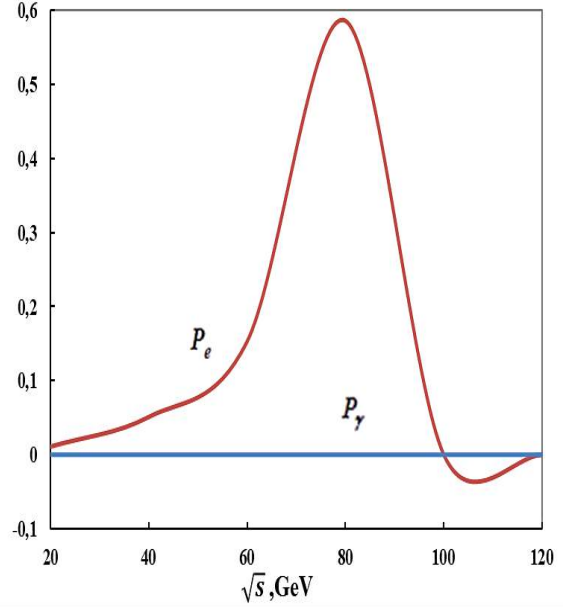


Fig. 10. The degrees of circular polarization of the photon  $P_\gamma(s)$  and degree of longitudinal electron polarization  $P_e(s)$  as a function of  $\sqrt{s}$ .

## CONCLUSION

Within the framework of the SM, the radiation decay of standard Higgs boson  $H \Rightarrow f + \bar{f} + \gamma$  was considered. The diagrams corresponding to the radiation of the photon by the fermion and antifermion, as well as the fermion and  $W$  - boson loop diagrams are studied in detail. Taking into account the longitudinal polarizations of the fermion pair and the circular polarization of the photon, an analytical expression is obtained for the decay width  $H \Rightarrow f + \bar{f} + \gamma$ . Expressions are found for the degree of circular polarization of the photon  $P_\gamma(s, z)$ ,  $P_\gamma(s)$ , the degree of longitudinal polarization of the fermion

$P_f(s, z)$ ,  $P_f(s)$  and the angular asymmetry of the forward and backward  $A_{FB}(s)$ . Then, numerical estimates of these quantities in the  $H \Rightarrow e^- + e^+ + \gamma$  decay are performed. The results are illustrated by graphs.

## APPENDIX

Here we give the expression of the squared amplitude corresponding to the contribution of the fermion and  $W$  - boson loop diagrams:

$$|M_{LOOP}|^2 = |M_1|^2 + |M_2|^2 + M_1^* M_2 + M_2^* M_1, \quad (A.1)$$

$$\begin{aligned} |M_1|^2 = & 2(p_1 \cdot k)(p_2 \cdot k)(e \cdot q)(e^* \cdot q)\{(1 - \lambda_1 \lambda_2)[|A_1|^2 + |A_2|^2] + 2(\lambda_2 - \lambda_1)Re(A_1 A_2^*)\} + (k \cdot q)^2 \times \\ & \times \{(1 - \lambda_1 \lambda_2)[(|A_1|^2 + |A_2|^2)((p_2 \cdot e)(p_1 \cdot e^*) + (p_1 \cdot e)(p_2 \cdot e^*) - (p_1 \cdot p_2)(e^* \cdot e)) - 2Re(A_1 A_2^*) \times \\ & \times i(p_1 p_2 e e^*)_\varepsilon] + (\lambda_2 - \lambda_1)[(|A_1|^2 + |A_2|^2)i(p_1 p_2 e^* e)_\varepsilon + 2Re(A_1 A_2^*)((p_2 \cdot e)(p_1 \cdot e^*) + \\ & + (p_1 \cdot e)(p_2 \cdot e^*) - (p_1 \cdot p_2)(e^* \cdot e))\} - (k \cdot q)(e \cdot q)\{(1 - \lambda_1 \lambda_2)[(|A_1|^2 + |A_2|^2)((p_1 \cdot e^*)(p_2 \cdot k) + \\ & + (p_2 \cdot e^*)(p_1 \cdot k)) - 2Re(A_1 A_2^*)i(p_1 p_2 k e^*)_\varepsilon] + (\lambda_2 - \lambda_1)[(|A_1|^2 + |A_2|^2)i(p_1 p_2 e^* k)_\varepsilon + 2Re(A_1 A_2^*) \times \\ & \times (p_1 \cdot e^*)(p_2 \cdot k) + (p_2 \cdot e^*)(p_1 \cdot k))\} - (k \cdot q)(e^* \cdot q)\{(1 - \lambda_1 \lambda_2)[(|A_1|^2 + |A_2|^2)((p_2 \cdot e) \times \\ & \times (p_1 \cdot k) + (p_1 \cdot e)(p_2 \cdot k)) + 2Re(A_1 A_2^*)i(p_1 p_2 k e)_\varepsilon] + (\lambda_2 - \lambda_1)[(|A_1|^2 + |A_2|^2)i(p_1 p_2 k e)_\varepsilon + \\ & + 2Re(A_1 A_2^*)((p_1 \cdot e)(p_2 \cdot k) + (p_2 \cdot e)(p_1 \cdot k))\}]; \end{aligned} \quad (A.2)$$

$$\begin{aligned} |M_2|^2 = & (1 - \lambda_1 \lambda_2)\{|A_3|^2 + |A_4|^2\}[2(p_1 p_2 k e^*)_\varepsilon(p_1 p_2 e k)_\varepsilon + (p_1 \cdot p_2)(\mu e^* k q)_\varepsilon(\mu e q k)_\varepsilon] + \\ & + 2Re(A_3 A_4^*)(\mu e^* k q)_\varepsilon(ve k q)_\varepsilon i(\mu \nu p_1 p_2)_\varepsilon\} + (\lambda_2 - \lambda_1)\{|A_3|^2 + |A_4|^2\}i(\mu e^* k q)_\varepsilon(ve k q)_\varepsilon(\mu \nu p_1 p_2)_\varepsilon + \\ & + 2Re(A_3 A_4^*)[2(p_1 p_2 k e^*)_\varepsilon(p_1 p_2 e k)_\varepsilon + (p_1 \cdot p_2)(\mu e^* k q)_\varepsilon(\mu e q k)_\varepsilon]; \end{aligned} \quad (A.3)$$

$$\begin{aligned} M_1^* M_2 + M_2^* M_1 = & (e \cdot q)\{(1 - \lambda_1 \lambda_2)[(A_1^* A_3 + A_2^* A_4)i(p_1 p_2 k e^*)_\varepsilon((p_2 \cdot k) - (p_1 \cdot k)) + \\ & + (A_1^* A_4 + A_2^* A_3)(\mu k q e^*)_\varepsilon(\mu p_1 p_2 k)_\varepsilon] + (\lambda_2 - \lambda_1)[(A_1^* A_3 + A_2^* A_4)(\mu k q e^*)_\varepsilon(\mu p_1 p_2 k)_\varepsilon + \\ & + (A_1^* A_4 + A_2^* A_3)i(p_1 p_2 k e^*)_\varepsilon((p_2 \cdot k) - (p_1 \cdot k))\} + (e^* \cdot q)\{(1 - \lambda_1 \lambda_2)[(A_3^* A_1 + A_4^* A_2) \times \\ & \times i(p_1 p_2 k e)_\varepsilon((p_1 \cdot k) - (p_2 \cdot k)) + (A_3^* A_2 + A_4^* A_1)(ve k q)_\varepsilon(vp_1 p_2 k)_\varepsilon] + (\lambda_2 - \lambda_1) \times \\ & \times [(A_3^* A_1 + A_4^* A_2)(ve k q)_\varepsilon(vp_1 p_2 k e)_\varepsilon + (A_3^* A_2 + A_4^* A_1)i(p_1 p_2 k e)_\varepsilon((p_1 \cdot k) - (p_2 \cdot k))\} + \\ & + (k \cdot q)\{(1 - \lambda_1 \lambda_2)[(A_1^* A_3 + A_2^* A_4)((p_2 \cdot e)i(p_1 e^* k q)_\varepsilon + (p_1 \cdot e)i(p_2 e^* k q)_\varepsilon - (p_1 \cdot p_2) \times \\ & \times i(e e^* k q)_\varepsilon] + (A_1^* A_4 + A_2^* A_3)(\mu e^* k q)_\varepsilon(p_2 e p_1 \mu)_\varepsilon - (A_3^* A_1 + A_4^* A_2)((p_2 \cdot e^*)i(p_1 e k q)_\varepsilon + \\ & + (p_1 \cdot e^*)i(p_2 e k q)_\varepsilon - (p_1 \cdot p_2)i(e^* e k q)_\varepsilon] - (A_3^* A_2 + A_4^* A_1)(ve k q)_\varepsilon(vp_1 p_2 e^*)_\varepsilon] + (\lambda_2 - \lambda_1) \times \\ & \times [(A_1^* A_3 + A_2^* A_4)(\mu e^* k q)_\varepsilon(\mu p_1 p_2 e)_\varepsilon + (A_1^* A_4 + A_2^* A_3)((p_2 \cdot e)i(p_1 e^* k q)_\varepsilon + (p_1 \cdot e)i(p_2 e^* k q)_\varepsilon - \\ & - (p_1 \cdot p_2)i(e e^* k q)_\varepsilon] - (A_3^* A_1 + A_4^* A_2)(ve k q)_\varepsilon(vp_1 p_2 e^*)_\varepsilon - (A_3^* A_2 + A_4^* A_1)((p_2 \cdot e^*)i(p_1 e k q)_\varepsilon + \\ & + (p_1 \cdot e^*)i(p_2 e k q)_\varepsilon - (p_1 \cdot p_2)i(e^* e k q)_\varepsilon]\}. \end{aligned} \quad (A.4)$$

Given designations are the following:

$$(abcd)_\varepsilon = \varepsilon_{\mu\nu\rho\sigma} a_\mu b_\nu c_\rho d_\sigma, \quad (\mu abc)_\varepsilon = \varepsilon_{\mu\nu\rho\sigma} a_\nu b_\rho c_\sigma, \quad (\mu\nu ab)_\varepsilon = \varepsilon_{\mu\nu\rho\sigma} a_\rho b_\sigma.$$

- |  |   |
|--|---|
| <p>[1] A. Djouadi. The Anatomy of Electro-Weak Symmetry Breaking. Tome I. The Higgs Boson in the Standard Model. arXiv: hep-ph / 050317v.2, 2005.</p> <p>[2] S.K. Abdullaev. Common properties of fundamental interactions. Baku, "Zəka print", 2018, p. 332 (in Azerbaijani).</p> <p>[3] ATLAS Collaboration. Observation of a new particle in the search for the Standard Model Higgs boson at the ATLAS detector at the LHC. Phys. Letters, 2012. B 716, p. 1-29.</p> | <p>[4] CMS Collaboration. Observation of a new boson at mass of 125 GeV with the CMS experiment at the LHC. Phys. Letters, 2012, B 716, p. 30-61.</p> <p>[5] V.A. Rubakov. UFN, 2012, t.182, №.10, p.1017-1025 (in Russian).</p> <p>[6] A.V. Lanev. UFN, 2014, t. 184, № 9, p. 996-1004 (in Russian).</p> <p>[7] D.I. Kazakov. UFN, 2014, t.184, № 9, p.1004-1017 (in Russian).</p> |
|--|---|

- [8] *S.K. Abdullayev, M.Sh. Gojayev, F.A. Saddigh.* Decay channels of the Standard Higgs Boson. Moscow University Physics Bulletin, 2017, vol. 72, № 4, p. 329-339.
- [9] *S.K. Abdullayev, E.Sh. Omarova.* Decays of Higgs Bosons into a gauge boson and a fermion-antifermion pair. Russian Physics Journal, 2019, vol. 62. № 1, p. 30-39.
- [10] *S.K. Abdullayev, E.Sh. Omarova.* Decay channels of Higgs Bosons  $H \Rightarrow \gamma\gamma$ ,  $H \Rightarrow \gamma Z$ ,  $H^\pm \Rightarrow \gamma W^\pm$ . Journal of BEU, Physics, 2019, vol. 3, № 1, p. 39-57.
- [11] *Yi Sun, H.-R. Chang, D.-N. Gao.* Higgs decays to  $\gamma l^+ l$  in the Standard Model. arXiv: 1303.2230v2, [hep-ph], 2013.
- [12] *A. Abbasabadi, D. Browser-Chao, D.A. Dicus, W.W. Repko.* Radiative Higgs boson decays  $H \Rightarrow f \bar{f} \gamma$ . Phys. Rev. 1997, D55, p. 5647.
- [13] *A. Abbasabadi, W.W. Repko.* Higgs boson decay to  $\mu \bar{\mu} \gamma$ . Phys. Rev. 2000, D62, p.054025.
- [14] *R. Akbar, I. Ahmed, M.J. Aslam.* Lepton polarization asymmetries of  $H \Rightarrow \gamma \tau^+ \tau^-$  decay in the Standard Model. Prog. Theor. Exp. Phys., 20114, p. 093B03.
- [15] *D.A. Dicus, W.W. Repko.* Calculation of the decay  $H \Rightarrow e \bar{e} \gamma$ . arXiv: 1302.2159 [hep-ph].

*Received: 02.12.2019*

# COMPARATIVE STUDY ON THE ELECTRICAL CHARACTERISTICS OF Au/n-Si AND Au/P3HT/n-Si SCHOTTKY CONTACTS

X. HIDIYEV, A. ASIMOV, A. KERIMOVA

*G.M. Abdullayev Institute of Physics of NAS Azerbaijan  
33, H. Javid ave., Baku, Azerbaijan, AZ-1143*

*Corresponding author: E-mail address: Hidiyev@gmail.com*

In this work, we have fabricated Au/P3HT/n-Si and Au/n-Si Schottky barrier diodes (SBDs) to investigate the effect of polymer interfacial layer on the electronic parameters. Electronic parameters of these two diodes were calculated from the current-voltage characteristics. It was seen that the ideality factor value of 3.47 calculated for the Au/P3HT/n-Si device was higher than the value of 1.18 of the Au/n-Si Schottky diodes. The high values in the ideality factor are caused possibly by various effects such as inhomogeneities of polymer interfacial layer film thickness and series resistance  $R_s$ . The  $R_s$  values obtained from Cheung's function are 18.6 and 495 for Au/n-Si and Au/P3HT/n-Si, respectively. Our results show that P3HT conductive polymer can be used in device modification for Schottky barrier diodes or photodiodes.

**Keywords:** Schottky diodes, conductive polymer, spin coating, poly (3-hexylthiophene)

**PACS:** 72.10-d; 73.30.+y; 73.40.GK.

## 1. INTRODUCTION

Conductive polymeric materials have advantage such as a good mechanical flexibility, high hole mobility, stable in the atmosphere and easy fabrication [1–5]. There has been much interest in the conductive polymeric materials in the study area of solar cells, light emitting diodes and thin film transistors. The polymeric interfacial layer in metal/polymer/semiconductor (MPS) structures play an important role in the determination of the electrical parameters of these diodes [6–10]. Among the conducting polymers, P3HT has specific properties such as a good mechanical flexibility, high hole mobility and is stable in the atmosphere. The performance of a MPS structures depends on various factors such as presence of the interface states at the metal/ polymer interfacial layer and barrier height and series resistance ( $R_s$ ) of MPS diodes.  $R_s$  and interfacial polymer layer is very important parameter of MPS structures. The electronic parameters of the diodes such as the ideality factor, the barrier height, the interface state density ( $N_{ss}$ ), the thickness of the interfacial layer and series resistance ( $R_s$ ) from current–voltage ( $I$ – $V$ ) and capacitance–voltage ( $C$ – $V$ ) measurements.

In this study, we will fabricate the Au/P3HT/n-Si metal/polymer/semiconductor (MPS) device by spin coating method. We investigated the electrical parameters of our Au/P3HT/n-Si Schottky diode using forward-bias current–voltage ( $I$ – $V$ ) measurements and compared the parameters to those for a conventional Au/n-Si diode.

## 2. EXPERIMENTAL PROCEDURES

$n$ -type Si semiconductor wafer with (100) orientation and 280 mm thickness was used before making contacts, the wafer was chemically cleaned using the RCA cleaning procedure (i.e. 10 min boil in  $H_2SO_4 + H_2O_2$  followed by a 10 min  $HCl + H_2O_2 + 6H_2O$  at 60°C). It was immersed in diluted 20% HF

for 60 s. The wafer was rinsed in de-ionized water of resistivity 18 M $\Omega$  cm with ultrasonic cleaning in each step. Finally, the sample was dried by exposing the surfaces to high-purity nitrogen. The ohmic contact with a thickness of  $\sim 1500$  Å was made by evaporating 99.9% purity Au metal on the back surface of the n-Si substrate, then was annealed at 550°C for 3 min in  $N_2$  atmosphere. Front surface of samples were coated with a conducting polymer poly(3-hexylthiophene) (P3HT) (fig. 1) film by spin coating (VTC-100) with 1200 rpm for 60 s. After that rectifier, Schottky contacts were formed on the other faces by evaporating  $\sim 2000$  Å thick Au. We also fabricated Au/n-Si reference diode without the polymer layer to compare with the electrical parameters of the Au/P3HT/n-Si device. All evaporation processes were carried out in a vacuum coating unit at about  $5.1 \times 10^{-6}$  Torr. Thus, Au/P3HT/n-Si/Au sandwich Schottky barrier type diode was fabricated. The  $I$ – $V$  measurements were performed using a Keithley 6517A electrometer. All measurements were controlled by a computer via an IEEE–488 standard interface so that the data collecting, processing and plotting could be accomplished automatically.

## 3. ANALYSIS OF AU/P3HT/N-SI JUNCTION DIODE AT ROOM TEMPERATURE

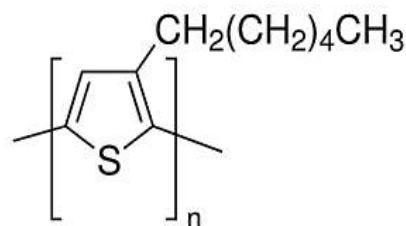


Fig. 1. Molecular structure of P3HT.

The forward-and reverse-bias  $I$ – $V$  characteristics of the Au/P3HT/n-Si contact and Au/n-Si diode at room temperature are shown in fig. 2. It is shown that

the saturation current in these semi-logarithmic plots decreases by P3HT. As clearly seen from fig. 2, the Au/P3HT/n-Si structure exhibits a good rectifying behavior. We analyze the experimental I-V characteristics by the forward bias thermionic emission (TE) theory given as follows [1-2].

$$I = I_0 \exp\left(\frac{q(V-IR)}{nkT}\right) \left[1 - \exp\left(\frac{-q(V-IR)}{kT}\right)\right] \quad (1)$$

where

$$I_0 = AA^*T \exp\left(-q \frac{\Phi_{b0}}{kT}\right) \quad (2)$$

is the saturation current,  $\Phi_{b0}$  (I-V) is the zero bias barrier height,  $A^*$  is the Richardson constant and equals to  $120 \text{ A cm}^{-2} \text{ K}^{-2}$  for  $n$ -type Si, where  $q$  is the electron charge,  $V$  is the bias voltage,  $A$  is the

effective diode area,  $k$  is the Boltzmann's constant,  $T$  is the temperature in Kelvin,  $n$  is the ideality factor. From eq. (1), ideality factor  $n$  can be written as:

$$n = \frac{q}{kT} \left(\frac{dV}{d(\ln I)}\right) \quad (3)$$

$n$  equals to one for an ideal diode. However,  $n$  has usually a value greater than unity. High values of  $n$  can be attributed to the presence of the interfacial thin native oxide layer and a wide distribution of low-SBH patches (or barrier height inhomogeneities), and, therefore, to the bias voltage dependence of the SBH [1-2].  $\Phi_{b0}$  is the zero-bias barrier height (BH), which can be obtained from the following equation

$$\Phi_{b0} = \frac{kT}{q} \ln\left(\frac{AA^*T^2}{I_0}\right) \quad (4)$$

Table

The experimental values of some parameters obtained from the forward bias I-V characteristics of Au/n-Si and Au/P3HT/n-Si Schottky barrier diodes at room temperature.

Diodes	n	$\Phi_b$	$I_0$	dV/dLn(I)		H (I)	
				n	$R_s$	$R_s$	$\Phi_b$
Au/n-Si	1,18	0,78	7,56e-9	1,12	18,6	13,5	0,73
Au/P3HT/n-Si	3,47	0,75	2,08E-8	6,07	495	611	0,74

Figure 2 presents the forward bias current-voltage (I-V) characteristics of the Au/P3HT/n-Si/Au structure. The  $\Phi_{b0}$  and  $n$  values of these diodes were calculated from a linear fit of the  $\ln I$  vs  $V$  plots in fig. 2 by using the eqs. (2) and (3) and the obtained values are 0.78 eV and 1.18 for Au/n-Si/Au diode, 0.75 eV and 3,47 for Au/P3HT/n-Si/Au diode, respectively. It has been observed that ideality factor of Au/P3HT/n-Si structure increases about 2.29 with respect to Au/n-Si at room temperature. The value of the ideality factor is greater than unity. The high values in the ideality factor are caused possibly by various effects such as inhomogeneities of P3HT film thickness, non-uniformity of the interfacial charges and series resistance, [11-14]. The values of the series resistance is determined from following functions using eq. (4).

$$\frac{dV}{d(\ln I)} = IR_s + n\left(\frac{kT}{q}\right) \quad (5)$$

$$H(I) = V - n\left(\frac{kT}{q}\right) \ln\left(\frac{I_0}{AA^*T^2}\right) \quad (6)$$

In fig. 3 (a) and (b), the values of  $dV/d(\ln I)$  and  $H(I)-I$  are plotted for Au/P3HT/n-Si and Au/n-Si Schottky contacts, respectively. A plot of  $dV/d(\ln I)$  vs  $I$  will gives  $R_s$  as the slope and  $n$  the  $y$ -axis intercept [15, 16]. The values of  $n$  and  $R_s$  for SBD were derived from fig. 3 by using eqs. (5) and (6), respectively, and they were presented in table 1. The  $R_s$  values obtained from eq. (5) are 18.6 and 495 for Au/n-Si and Au/P3HT/n-Si respectively. The high series resistance  $R_s$  value can be attributed to the presence of a native

interfacial layer between metal and semiconductor.

The interface states and interfacial layer between the metal/semiconductor structures play an important role in the determination of the electronic parameters of the diodes.

Density of interface states proposed by Card and Rhoderick can be simplified and given as [17, 18]:

$$N_{ss}(V) = \frac{1}{q} \left\{ \frac{\epsilon_i}{\delta} [n(V) - 1] - \frac{\epsilon_s}{W_D} \right\} \quad (7)$$

where  $N_{ss}$  is the density of the interface states,  $\delta$  is the thickness of interfacial layer,  $W_D$  is the space charge width, and  $n(V)$  is the voltage-dependent ideality factor,  $\epsilon_s = 11.8\epsilon_0$  and  $\epsilon_i = 3\epsilon_0$  are the permittivity of the semiconductor and conducting polymer (P3HT), respectively. In  $n$ -type semiconductors, the energy of the interface states  $E_{ss}$  with respect to the bottom of the conduction band at the surface of the semiconductor is given by

$$E_c - E_{ss} = q(\Phi_e - V_D) \quad (8)$$

where  $V_D$  is the applied voltage drop across the depletion layer and  $\Phi_e$  is the effective barrier height.  $N_{ss}$  values are obtained via eq. (7). Figure 4 shows the energy distribution profiles of  $N_{ss}$  extracted from the forward bias I-V characteristics for Au/P3HT/n-Si and Au/n-Si Schottky barrier diodes. The magnitude of  $N_{ss}$  ranges from  $5.05 \times 10^{11}$  at Ec-0.63 eV to  $2.01 \times 10^{12} \text{ eV}^{-1} \text{ cm}^{-2}$  at Ec-0.46 eV for Au/P3HT/n-SiSBD and  $5.46 \times 10^{11}$  at Ec-0.61 eV to  $6.33 \times 10^{11} \text{ eV}^{-1} \text{ cm}^{-2}$  at Ec-0.47 eV for Au/n-Si Schottky barrier diodes.



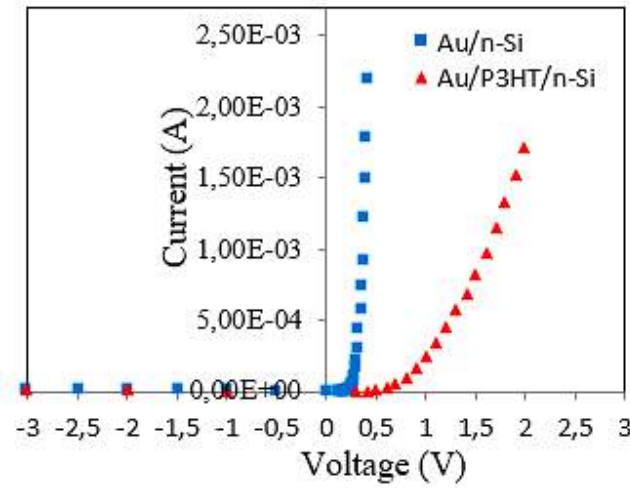


Fig. 2. The forward and reverse bias semi-logarithmic I-V characteristics of Au/n-Si and Au/P3HT/n-Si Schottky barrier diodes at room temperature.

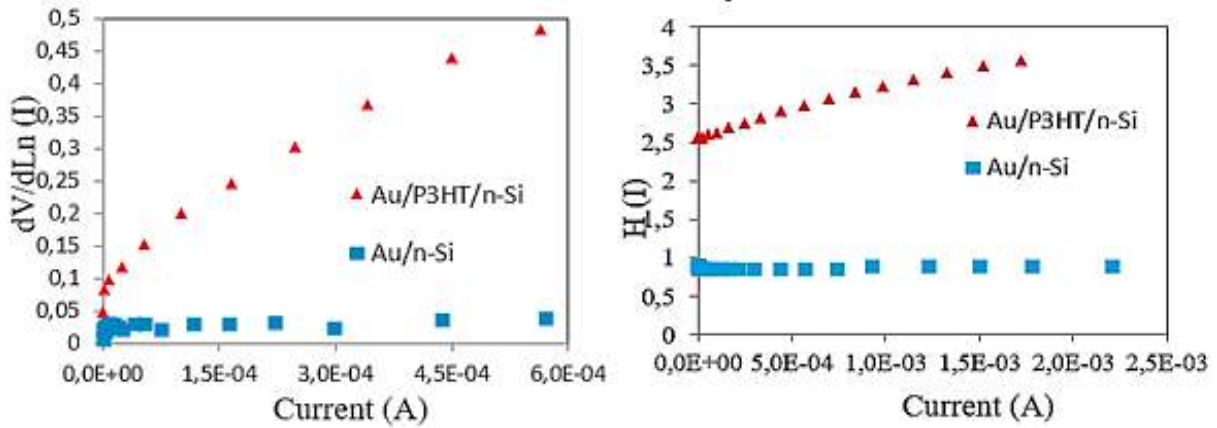


Fig. 3. The plots of  $dV/d \ln I$  and  $H(I)$  vs. current of Au/n-Si and Au/P3HT/n-Si Schottky barrier diodes at room temperature.

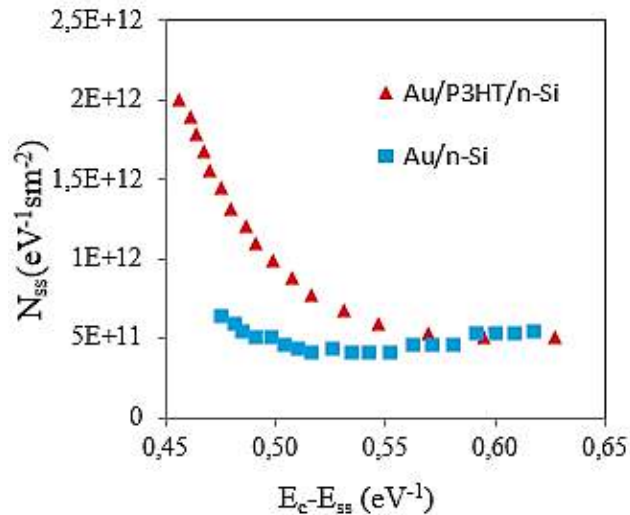


Fig. 4. The energy distribution profiles of  $N_{ss}$  for Au/n-Si and Au/P3HT/n-Si Schottky barrier diodes at room temperature.

#### 4. CONCLUSION

Electronic properties of the Au/n-Si and Au/P3HT/n-Si Schottky barrier diode have been investigated by means of I-V measurements at room temperature. It was seen that the ideality factor value of 3.47 eV calculated for the Au/P3HT/n-Si device

was higher than the value of 1.18 eV of the Au/n-Si Schottky barrier diodes. The values of the ideality factor, series resistance and barrier height obtained from Cheung and Norde method were compared, and it was seen that there was an agreement with each other.

- [1] *S.M. Sze. Physics of Semiconductor Devices*, 2nd ed., John Wiley & Sons, New York, 1981.
- [2] *E.H. Rhoderick, R.H. Williams. Metal–Semiconductor Contacts*, Clarendon, Oxford, 1988.
- [3] *T. Tunç, İ. Uslu, İ. Dökme, Ş. Altındal, H. Uslu. International Journal of Polymeric Materials*, 2010.
- [4] *F. Yakuphanoglu. Synthetic Metals* 160, 1551–1555, 2010.
- [5] *P. Anuragudom. J. El-daye, P. Chinwangso, R.C. Advincula, S. Phanichphant, T.R. Lee. Polymer International* 60 660–665, 2011.
- [6] *Ahmed Fatime E, OA. Yassin. Microelectron J*; 38:834, 2007.
- [7] *F. Yakuphanoglu. J. Alloys Compd.* 494, 451e455, 2010.
- [8] *N.C. Nguyen. Potje-Kamloth K. Thin Solid Films*; 338:142, 1999.
- [9] *W. Brütting. Physics of Organic Semiconductors*, Wiley- VCH- Verlag GmbH & Co. KGaA, Weinheim, 2005.
- [10] *E.J. Meijer, A.V.G. Mangnus, C.M. Hart, D.M. de Leeuw, T.M. Klapwijk. Appl. Phys. Lett.* 78, 2001.
- [11] *F.Yakuphanoglu, M.Shah and W. Aslam Farooq. A. Phys. Polonica A* 120, 3, 2011.
- [12] *E. Voroshazi, B. Verreet, T. Aernouts, P. Heremans. Solar Energy Mater. Solar Cells* 95, 1303–1307, 2011.
- [13] *M. Manceau, A. Rivaton, J.L. Gardette, S.Guillerez, N. Lemaître. Solar Energy Mater. Solar Cells* 95, 1315–1325, 2011.
- [14] *O. Güllü, S. Aydoğan, A. Türüt. Microelectron. Eng.* 85, 1647, 2008.
- [15] *S.K. Cheung, N.W. Cheung. Appl. Phys. Lett.* 49, 85, 1986.
- [16] *T. Kilicoğlu. Thin Solid Films*; 516:967, 2008.
- [17] *H.J. Norde. Appl. Phys.*; 50:5052, 1979.
- [18] *H.C. Card. E.H. Rhoderick, J. Phys. D: Appl. Phys.* 4, 1589, 1971.

*Received: 31.01.2020*

ANALYSIS OF FLUCTUATION CONDUCTIVITY IN  $Y_{0.6}Cd_{0.4}Ba_2Cu_3O_{7-\delta}$ V.M. ALIEV<sup>1</sup>, J.A. RAGIMOV<sup>2</sup>, R.I. SELIM-ZADE<sup>1</sup>, B.A. TAIROV<sup>1</sup><sup>1</sup>*Institute of Physics of the National Academy of Sciences of Azerbaijan,  
131, H. Javid Ave., Baku, AZ 1143*<sup>2</sup>*Azerbaijan Medical University, 23, Bakykhanov str., Baku, AZ 1022  
v\_aliev@bk.ru*

The mechanism of formation of excess conductivity in cuprate high-temperature superconductors (HTSC)  $Y_{0.6}Cd_{0.4}Ba_2Cu_3O_{7-\delta}$  and  $YBa_2Cu_3O_{7-\delta}$  was considered within the framework of the local pair model taking into account the Aslamazov-Larkin theory near  $T_c$ . The temperature  $T_0$  of the transition from the 2D fluctuation region to the 3D region (the temperature of the 2D-3D crossover) is determined. The coherence lengths of the fluctuation Cooper pairs  $\xi_c(0)$  along the  $c$  axis are calculated. It was shown that a partial substitution of Y by Cd in the Y – Ba – Cu – O system leads to a decrease in  $\xi_c(0)$  by  $\sim 2$  times (from 6.32 Å to 3.18 Å), as well as to the expansion as the region of existence pseudogaps and superconducting (SC) fluctuations near  $T_c$ . The temperature dependence of the pseudogap  $\Delta^*(T)$  and the values of  $\Delta^*(T_c)$  are determined, and temperatures  $T_m$  corresponding to the maximum temperature dependence of the pseudogap in these materials are estimated. The maximum values of the pseudogap in samples  $Y_{0.6}Cd_{0.4}Ba_2Cu_3O_{7-\delta}$  and  $YBa_2Cu_3O_{7-\delta}$  are 34.56 meV and 28.4 meV correspondingly.

PACS: 74.25.Fy, 74.20.Mn, 74.72.±h, 74.25.±q, 74.25.Jb

Keywords: superconductivity, pseudogap, excess conductivity, coherence length, composition.

## INTRODUCTION

In recent years, the group of works [1–5] devoted to the analysis of pseudogap effects in HTSC compounds has appeared. Pseudogap (PG) is a unique phenomenon characteristic of HTSC with an active  $CuO_2$  plane (cuprates) in the doping region less than optimal. It manifests itself in studies of the phenomena of tunneling, photoemission, heat capacity [2, 4] and other properties of HTSC. It is assumed that at a certain temperature  $T^* \gg T_c$  ( $T_c$  is the critical temperature of the superconducting transition) the density of states on the Fermi surface is redistributed: on a part of this surface the density of states decreases. Below the temperature  $T^*$ , the compound is in a pseudogap state. In these works, possible conduction mechanisms in the modes of the normal, superconducting, and pseudogap states in HTSC are also discussed.

Recently, the work [6], devoted to the study of the pseudogap state in  $Pb_{0.55}Bi_{1.5}Sr_{1.6}La_{0.4}CuO_{6+\delta}$  (Pb-Bi2201) appeared. A series of Pb-Bi2201 single crystals was obtained, on which a wide range of investigations were conducted to identify the pseudogap state. The results of studies on three different experimental methods indicate that the appearance of a pseudogap at  $T \approx 132$  K should be perceived only as a phase transition. Thus, the authors confirmed the assumption that at the temperature decreasing, the HESC material must undergo two phase transitions: first the appearance of a pseudogap, and then a transition to the superconducting state.

However, as noted by A. Abrikosov [7], the pseudogap state cannot really be considered as some kind of new phase state of matter, since the PG is not separated from the normal state by a phase transition. So the question of a possible phase transition at  $T = T^*$  also remains open. At the same time, it can be said that a crossover occurs at  $T = T^*$  [1]. Below this temperature, due to reasons not yet established to date,

the density of quasiparticle states at the Fermi level begins to decrease. Actually for this reason, this phenomenon is called "pseudogap". For the first time, this result was obtained in experiments on the study of NMR in a weakly doped Y123 system, in which an anomalous decrease of the Knight shift [2] during cooling, which is directly related to the density of states at the Fermi level in the Landau theory, was observed.

In order to receive answers to the above questions in this work, we have analyzed the excess conductivity separated from resistive measurements on partially doped  $Y_{0.6}Cd_{0.4}Ba_2Cu_3O_{7-\delta}$  with a SC transition at 85 K.

Thus, the aim of this work is to study the normal state of  $YBa_2Cu_3O_{7-\delta}$  (Y1) and  $Y_{0.6}Cd_{0.4}Ba_2Cu_3O_{7-\delta}$  (Y2) in the temperature range  $T^* > T > T_c$ , to determine their physical characteristics, as well as to study the possibility of the occurrence of the PG states in these compounds. The analysis was carried out on the basis of the study of excess conductivity above  $T_c$  in the framework of the local pair (LP) model [3, 4] taking into account the Aslamazov – Larkin fluctuation theory [8] near  $T_c$ .

## EXPERIMENTAL RESULTS AND THEIR PROCESSING

The method for obtaining  $Y_{0.6}Cd_{0.4}Ba_2Cu_3O_{7-\delta}$  is described in [9].

The temperature dependences of the specific resistivity  $\rho$  of the samples Y1 and Y2 are showed in fig.1. The critical temperatures of the SC transition  $T_c$  were determined from the maximum obtained by differentiating of the curve  $\rho(T)$ . Critical temperatures of investigated samples are  $T_{c1} = 92.63$  K (Y1) and  $T_{c2} = 89.23$  K (Y2) (fig.1). In this case, the resistivity of the sample  $Y_{0.6}Cd_{0.4}Ba_2Cu_3O_{7-\delta}$  in the normal phase at 300 K increases almost 2 times in comparison with  $YBa_2Cu_3O_{7-\delta}$ .

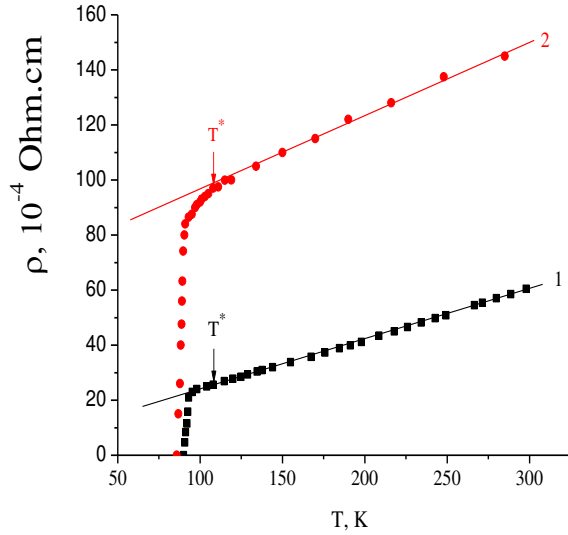


Fig. 1. Temperature dependences of the resistivity of samples Y1 is  $\text{YBa}_2\text{Cu}_3\text{O}_{7-\delta}$  (1) and Y2 is  $\text{Y}_{0.6}\text{Cd}_{0.4}\text{Ba}_2\text{Cu}_3\text{O}_{7-\delta}$  (2).

## FLUCTUATION CONDUCTIVITY

The linear course of the temperature dependence of the specific resistance of samples Y1 and Y2 in the normal phase is well extrapolated by the expressions  $\rho_{Y1n}(T) = (D + \kappa T + BT^2)$  and  $\rho_{Y2n}(T) = (\rho_0 + \kappa T + BT^2)$  (here  $D$ ,  $B$  and  $k$  are some constants). This linear relationship, extrapolated to the low temperature range, was used to determine excess conductivity  $\Delta\sigma(T)$  according to:

$$\Delta\sigma(T) = \rho^{-1}(T) - \rho_n^{-1}(T). \quad (1)$$

The analysis of the behavior of excess conductivities was carried out in the framework of the local pair model [4, 10].

Assuming the possibility of the formation of local pairs [3,4] in samples at temperatures below  $T^* = 107.57\text{K}$  (Y1) and  $T^* = 108.22\text{K}$  (Y2), the experimental results obtained near  $T_c$  were analyzed taking into account the occurrence of fluctuation Cooper pairs (FCP) above  $T_c$  in the framework of the theory of Aslamazov-Larkin (AL) [8].

The fig. 2 shows dependence of the logarithm of the excess conductivity of the samples Y1 (1) and Y2 (2) on the logarithm of the reduced temperature  $\varepsilon = (T/T_c - 1)$ . According to the theory of AL, as well as Hikami-Larkin (HL) developed for HTSC [10], in the region of  $T > T_c$  (but near  $T_c$ ), the fluctuation coupling of charge carriers occurs, leading to the appearance of fluctuation conductivity (FC). In this region, the temperature dependence of excess conductivity on temperature is described by the expressions:

$$\Delta\sigma_{\text{AL3D}} = C_{3D} \{e^2/[32\hbar\xi_c(0)]\} \varepsilon^{-1/2}, \quad (2)$$

$$\Delta\sigma_{\text{AL2D}} = C_{2D} \{e^2/[16\hbar d]\} \varepsilon^{-1}, \quad (3)$$

respectively for three-dimensional (3D) and two-dimensional (2D) region. The scaling coefficients  $C$  are used to combine the theory with experiment [4].

Thus, by the angle of inclination  $\alpha$  of dependences  $\ln(\Delta\sigma)$  as a function of  $\varepsilon = \ln(T/T_c - 1)$  (see fig. 3), we can distinguish 2D ( $\text{tg}\alpha = -1$ ) and 3D ( $\text{tg}\alpha = -1/2$ ) regions of phase transition. It can also determine the crossover temperature  $T_0$  (the transition temperature from  $\Delta\sigma_{2D}$  to  $\sigma_{3D}$ ) and the tangents of the slopes of the dependences  $\Delta\sigma(T)$  corresponding to the exponents  $\varepsilon$  in equations (2) and (3). The corresponding values of the parameters 2D and 3D regions determined from the experiment for sample Y1 are 2D ( $\text{tg}\alpha = -1.04$ ) and 3D ( $\text{tg}\alpha = -0.44$ ) and for Y2 are 2D ( $\text{tg}\alpha = -1.1$ ) and 3D ( $\text{tg}\alpha = -0.49$ ).

On basis of value the temperature of the crossover  $T_0$ , which corresponds to  $\ln\varepsilon_0$ , according to Fig. 2, it can determine the coherence length of local pairs along the  $c$  axis [11,12]:

$$\xi_c(0) = d\sqrt{\varepsilon_0}, \quad (4)$$

here  $d$  is the distance between the inner conducting planes in Y-Ba-Cu-O [13],  $d \approx 11.7\text{\AA}$ . The values of  $\xi_c(0) = 6.32\text{\AA}$  ( $\ln\varepsilon_0 \approx -1.2318$ ) for Y1 and  $\xi_c(0) = 3.18$  ( $\ln\varepsilon_0 \approx -2.755$ ) for Y2 are obtained correspondingly

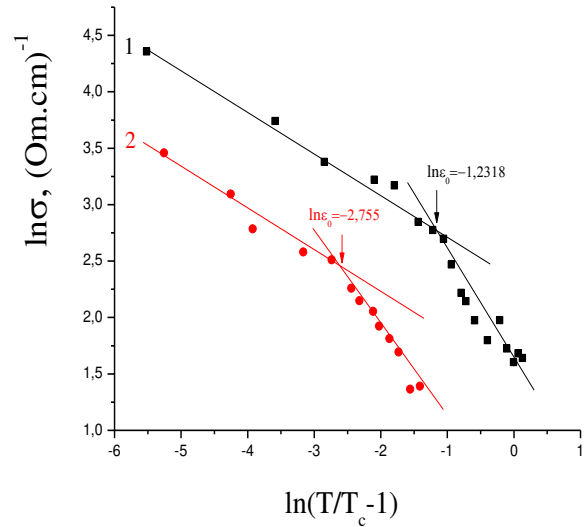


Fig. 2. The dependences of the logarithm of excess conductivity on logarithm  $(T/T_c - 1)$  of samples Y1 (1) and Y2 (2). The solid lines are the calculations in the framework of the Aslamazov-Larkin theory.

## ANALYSIS OF THE MAGNITUDE AND TEMPERATURE DEPENDENCE OF THE PSEUDOGAP

As noted above, in the cuprates at  $T < T^*$ , the density of electron states of quasiparticles on the Fermi level decreases [14] (the cause of this phenomenon is not yet fully elucidated), which creates conditions for the formation of a pseudogap in the excitation spectrum and it leads ultimately to the formation of an excess conductivity. The magnitude and temperature dependence of the pseudogap in the investigated samples was analyzed using the local pair model, taking into account the transition from Bose-Einstein condensation (BEC) to the BCS mode predicted by the theory [10] for HTSC when the temperature decreases in the interval  $T^* < T < T_c$ . Note

that excess conductivity exists precisely in this temperature range, where fermions supposedly form pairs- the so-called strongly coupled bosons (SCB). The pseudogap is characterized by a certain value of the binding energy  $\varepsilon_b \sim 1/\xi^2(T)$ , causing the creation of such pairs [10,13], which decreases with temperature, because the coherence length of the Cooper pairs  $\xi(T) = \xi(0)(T/T_c - 1)^{-1/2}$ , on the contrary, increases with decreasing temperatures. Therefore, according to the LP model, the SCB transform into the FCP when the temperature approaches  $T_c$  (BEC-BCSh transition), which becomes possible due to the extremely small coherence length  $\xi(T)$  in cuprates.

From our studies, we can estimate the magnitude and temperature dependence of PG, based on the temperature dependence of excess conductivity in the temperature interval from  $T^*$  to  $T_c$  according to [3, 13]:

$$\Delta\sigma(\varepsilon) = \left\{ \frac{A(1 - T/T^*)[\exp(-\Delta^*/T)]e^2}{16\eta\xi_c(0)\sqrt{2\varepsilon_0^*} \cdot sh(2\varepsilon/\varepsilon_0^*)} \right\} \quad (5)$$

where the  $(1 - T/T^*)$  determines the number of pairs formed at  $T \leq T^*$ ; and the  $\exp(-\Delta^*/T)$  determines the number of pairs destroyed by thermal fluctuations below the BEC-BCSh transition temperature. The coefficient  $A$  has the same meaning as the coefficients  $C_{3D}$  and  $C_{2D}$  in (2) and (3).

The solution of equation (5) gives the value of  $\Delta^*$ :

$$\Delta^*(T) = T \cdot \ln \left\{ \frac{A(1 - T/T^*)e^2}{\Delta\sigma(T)16\eta\xi_c(0)\sqrt{2\varepsilon_0^*} \cdot sh(2\varepsilon/\varepsilon_0^*)} \right\} \quad (6)$$

where  $\Delta\sigma(T)$  is the experimentally determined excess conductivity.

Fig. 3 shows the dependence of logarithm of the excess conductivity of samples Y1 and Y2 on the inverse temperature. The choice of such coordinates is due to the strong sensitivity of the linear region  $\ln\Delta\sigma(1/T)$  to the value of  $\Delta^*(T_c)$  in equation (5), which allows to estimate this parameter with high accuracy (this is necessary to find the coefficient  $A$ ) [3,13,15]. The dependences  $\ln\Delta\sigma(1/T)$  were calculated according to the method approved in [12]. As can be seen from fig. 3 (curves 1 and 2), in this case, the values  $\ln\Delta\sigma(1/T)$  calculated for both samples with parameters:  $A = 82.4 \pm 0.1$ ,  $T^* = 107.57K$ ,  $\xi_c(0) = 6.32 \text{ \AA}$  (Y1) and  $A = 5.53 \pm 0.1$ ,  $T^* = 108.22K$ ,  $\xi_c(0) = 3.18 \text{ \AA}$  (Y2) are in good agreement with the experimental data.

The temperature dependence and the value of the pseudogap parameter  $\Delta^*(T)$  (fig. 4) were calculated on the basis of equation (6) with the parameters given above. As noted in [3, 4, 13], the value of the coefficient  $A$  is selected from the condition of coincidence of the temperature dependence of  $\Delta\sigma$  (equation (5), assuming  $\Delta^* = \Delta^*(T)$ ) with experimental data in the region of 3D fluctuations near  $T_c$ . According to [13, 16], the optimal approximation for the HTSC material is achieved with values of  $2\Delta^*(T_c)/k_B T_c \approx 5 \div 7$ .

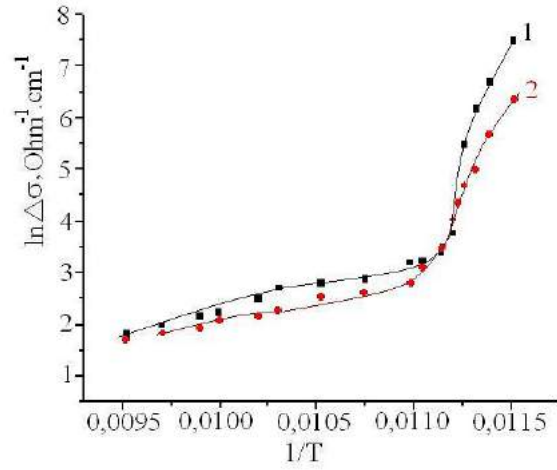


Fig. 3. The dependences of logarithm of excess conductivity on inverse temperature: 1-Y1; 2-Y2; solid lines are approximations of eq. (3) with the parameters given in text.

For sample Y1, the values  $2\Delta^*(T_c)/k_B T_c = 5$ , and for Y2  $2\Delta^*(T_c)/k_B T_c = 4.5$  have been obtained. As a result, the values of  $A = 82.4$  and  $\Delta^*(T_c) = 92.62 \cdot 2.7 = 250.07K$ ; for Y2  $A = 5.53$  and  $\Delta^*(T_c) = 89.23 \cdot 2.5 = 223.075K$  have been obtained, and it consistent with the experimental data (fig. 4).

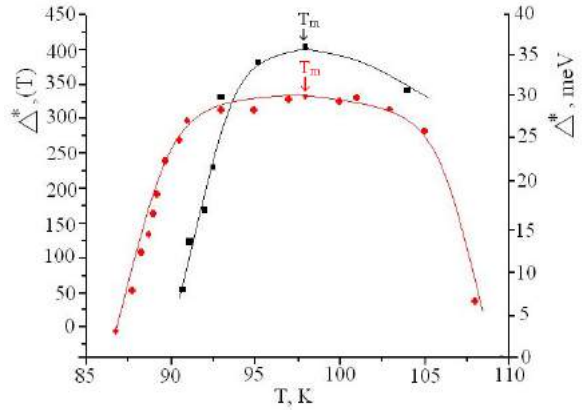


Fig. 4. Temperature dependences of the calculated pseudogap of samples Y1 (1) and Y2 (2) with the parameters given in the text. The arrows show the pseudogap maximum values.

The temperature dependences of  $\Delta^*(T)$  obtained on the basis of equation (6) are shown in fig. 4. The maximum values of the pseudogap for Y1  $\Delta^*_{\max} \approx 34.56 \text{ meV}$  ( $\Delta^*(T_m) \approx 402.66 \text{ K}$ ,  $T_m = 97.98K$ ) for Y2  $\Delta^*_{\max} \approx 28.5 \text{ meV}$  ( $\Delta^*(T_m) \approx 330.13 \text{ K}$ ,  $T_m \approx 98.22 \text{ K}$ ) are determined.

From the presented data in fig. 4, it is also seen that as  $T$  decreases, the pseudogap value first increases, then, after passing through a maximum, decreases. This decrease is due to the transformation of the SCB in the PCF as a result of the BEC-BCSh transition, which accompanied by an increase in excess conductivity at  $T \rightarrow T_c$ . Such a behavior of  $\Delta^*$  with decreasing temperature was first found on YBCO films [3.13] with different oxygen contents, which

seems to be typical of cuprate HTSC [13]. Thus it can be concluded that in investigated  $Y_{0.6}Cd_{0.4}Ba_2Cu_3O_{7-\delta}$  and  $YBa_2Cu_3O_{7-\delta}$  it is possible the local pair formation of charge carriers at  $T \gg T_c$ , which creates conditions for the formation of a pseudogap [13,16] the subsequent establishment of the phase coherence of the fluctuating Cooper pairs at  $T < T_c$  [17].

## CONCLUSION

The investigation of the effect of partial substitution of Y by Cd on the mechanism of excess conductivity in Y-Ba-Cu-O polycrystals showed that partial substitution of Y by Cd leads to a decrease in the critical temperatures of the  $Y_{0.6}Cd_{0.4}Ba_2Cu_3O_{7-\delta}$  (Y2) sample compared to  $YBa_2Cu_3O_{7-\delta}$  (Y1) (respectively  $T_c$  (Y2)=89.23K and  $T_c$  (Y1)= 92.628K). In this case, the resistivity of the sample  $Y_{0.6}Cd_{0.4}Ba_2Cu_3O_{7-\delta}$  in the normal phase at 300 K increases (2 times) compared to  $YBa_2Cu_3O_{7-\delta}$ . At the same time, there is an expansion of the temperature regions of PG and FCP, as well as a decrease in the coherence length of Cooper pairs.

Studies and analysis have shown that the excess conductivity  $\Delta\sigma(T)$  in  $Y_{0.6}Cd_{0.4}Ba_2Cu_3O_{7-\delta}$  in the temperature range  $T_c < T < T^*$  is satisfactorily described in the framework of the model of local pairs [3,14].

The analysis result of the pseudogap state by the method of excess conductivity confirms that the model of local pairs in this case is applicable to both samples.

At  $T \rightarrow T_c$ , the behavior of  $\Delta\sigma(T)$  of both samples obeys to the Aslamazov – Larkin theory for 2D and 3D fluctuations [8, 11]. Thus, before the transition to the superconducting state, the region of superconducting fluctuations is always realized in the form of a FCP, in which  $\Delta\sigma(T)$  is described by equation (2) for 3D superconductors (that is, before the SP transition, the HTSC transition is always three-dimensional).

Thus, it can be assumed that in  $YBa_2Cu_3O_{7-\delta}$  and  $Y_{0.6}Cd_{0.4}Ba_2Cu_3O_{7-\delta}$  PG forms by converting the  $d$ -wave SC energy gap in  $CuO_2$  planes into the corresponding gap of the fluctuation Cooper pairs above  $T_c$ .

- 
- [1] E.B. Amitin, K.R. Zhdanov, A.G. Blinov et al. Low Temp. Phys., 31, 4, 323-326, 2005.
  - [2] M.V. Sadovsky. Physics-Uspekhi, 171, 539-564, 2001.
  - [3] M.R. Trunin. Physics-Uspekhi, 175, 10, 1017-1037, 2005.
  - [4] A.L. Soloviev, V.M. Dmitriev. Low Temp. Phys., 32, 6, 753-760, 2006.
  - [5] A.L. Solovjov, M.A. Tkachenko, R.V. Vovk, A. Chroneos. Physica C, 501, 24–31, 2014.
  - [6] He Rui-Hua., M. Hashimoto, H. Karapetyan et al. Science, 331, 1579-1583, 2011.
  - [7] A.A. Abrikosov. Physics-Uspekhi, 174, 11, 1233-1239, 2004.
  - [8] L.G. Aslamazov and A.L. Larkin. Physics Letters, 26A, 6, 238-239, 1968.
  - [9] S.A. Aliev, S.S. Ragimov, V.M. Aliev. AJP Fizika, 10, 4, 42-43, 2004.
  - [10] V.M. Loktev, V.M. Turkowski. Low Temp. Phys., 30, 3, 247-260, 2004.
  - [11] S. Hikami, A.I. Larkin. Modern Phys. Lett., V. B2, 693-697, 1988.
  - [12] B.Oh, K.Char, A.D.Kent et al. Phys. Rev. B37, 13, 7861-7864, 1988.
  - [13] A.L. Soloviev, V.M. Dmitriev, Low Temp. Phys., 35, 3, 227-264, 2009.
  - [14] A.A. Kordyuk, Low Temp. Phys., 41, 5, 417-444, 2015.
  - [15] D.D. Prokofiev, M.P. Volkov, Yu.A. Boykov. Solid State Physics, 45, 7, 1168-1176, 2003.
  - [16] V.V. Florentiev, A.V. Inyushkin, A.N. Taldenkov et al. Superconductivity: physics, chemistry, technology, 3, 10, part 2, 2302-2319, 1990.
  - [17] R. Peters and J. Bauer. Phys. Rev. B 92, 014511 - Published 22 July, 2015.

Received: 03.02.2020



# THE STUDY OF THE PHOTORESPONSE OF THE MAPD MATRIX FOR SCINTILLATION RADIATION

**RAMIL ALADDIN AKBAROV**

*National Nuclear Research Center, Baku, Azerbaijan*

*Joint Institute for Nuclear Research, Dubna, Russia*

*Institute of Radiation Problems, Baku Azerbaijan*

*ramilakbarow@gmail.com*

This paper presents the performance of the detection efficiency of gamma radiation with a detector based on LYSO, YSO (Ce), BGO scintillators and a nine-channel array of micropixel avalanche photodiodes (MAPD) with high pixel density (PD) and photon detection efficiency (PDE). The sensitive area of the detector, consisting of single MAPDs with an active area of  $3.7 \times 3.7 \text{ mm}^2$  and has a common output for signal output, is  $11.5 \times 11.5 \text{ mm}^2$ . Breakdown voltages were measured for each channel, as a result of which the optimal operating voltage for the entire array was revealed. The linearity range and energy resolution for each crystal were determined by the energy range from 30 to 1770 keV. The high pixel density of the array made it possible to achieve good linearity in the studied energy range, which makes it possible to use the matrix in gamma-ray spectroscopy detectors.

**Keywords:** MAPD; mikropixel avalanche photodiode; SiPM; photodetection efficiency.

**PACS:** 72.40.+w, 77.22.Ch

## INTRODUCTION

Traditional vacuum photomultiplier tubes (PMTs) have long been successfully used as a photodetector. However, modern technologies have led to the development of new types of photodetectors -silicon photomultipliers (SiPM), which have such advantages as high detection efficiency, low operating voltage, compactness, insensitivity to magnetic fields, low cost, etc. [1-3]. Despite the advantages, they have some disadvantages, such as limited pixel density (PD), and active region. Due to the limited pixel density, the SiPM response is nonlinear with an increase in the number of photons [4]. Therefore, it is necessary to develop SiPM with a high pixel density while maintaining photon detection efficiency (PDE). Significant improvement in SiPM dynamic range is provided by Zecotek Photonics Inc.'s innovative MAPD design. [3, 5-7]. For scintillation detectors, the detection efficiency increases with increasing area of the photosensor and crystals. To increase the

efficiency of photon collection from large scintillators, it becomes necessary to use several SiPMs due to their small core sizes. This paper presents a study of a nine-element MAPD-based matrix with a high PD/PDE ratio and three scintillators with different light output and decay time as a detector in gamma spectrometry.

## USED SAMPLES

An array of 9 single-element MAPD-3NK photodiodes from Zecotek Photonics Inc. It was assembled on a specially designed printed circuit board, the contact pads of which were located on the back side. Each MAPD-3NK element had an area of  $3.7 \times 3.7 \text{ mm}^2$  with a pixel density of  $10\,000 \text{ mm}^{-2}$  and a high PDE - 40%. The matrix had a total capacitance of  $\sim 1.8 \text{ nF}$ . The geometric fill factor (GFF) of the MAPD array was 76%.

To test the MAPD matrix, three types of scintillators LYSO, YSO, and BGO were selected [8], the properties of which are presented in Table 1.

Properties of scintillators

Table 1

	LYSO (Ce)	YSO	BGO
Density (g/cm <sup>3</sup> )	7,25	4,50	7,13
Emission wavelength max (nm)	420	420	480
Light output (Photons/MeV)	28000-34000	21000-24000	8000-10000
Decay time (ns)	42	50-70	300
Refractive index	1,82	1,8	2,15
Hygroscopic	no	no	no
Size (mm <sup>2</sup> )	10×10×10	10×10×10	10×10×10

## EXPERIMENTAL SETUP

The experimental setup is shown in fig. 1. During the measurements, the detector and preamplifier were placed in a shielded and light isolated black box. The signal was amplified by a preamplifier (gain 40) and recorded by the CAEN DT5720B analog-to-digital converter (ADC). The ADC input impedance was 50 ohms. All data analysis

was performed using an algorithm written in the ROOT data analysis environment developed by CERN. The measurements were carried out at a temperature of 22° C. In the experiments, Co-57, Cs-137, Eu-152, and Bi-207 were used as gamma radiation sources, the gamma-ray energy of which is in the range 30–1770 keV. All measurements were carried out under the same conditions and in the same time interval of 300 nanoseconds.

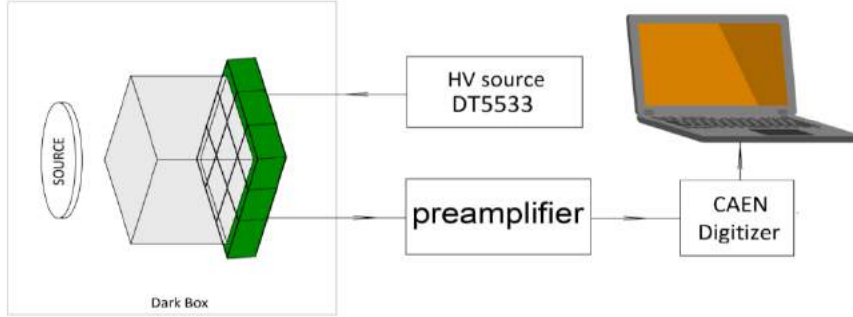


Fig. 1. The block diagram of the experimental setup.

## EXPERIMENTAL RESULTS

The breakdown voltage for each SiPM is individual and also depends on production processes.

Therefore, it was necessary to determine the breakdown voltage for each MAPD. Measurements of the current-voltage characteristics (I-V) were performed for all MAPDs.

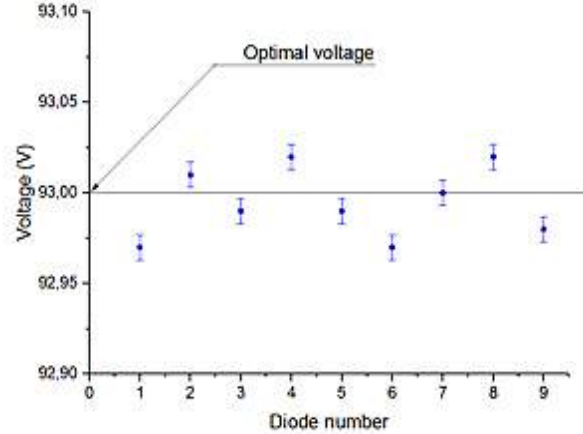
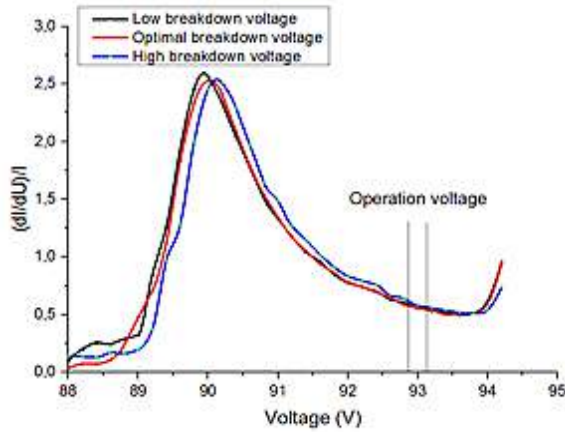


Fig. 2. Current-voltage characteristics (left) and operating voltages (right) for all MAPDs in the matrix.

Fig. 2 (left) shows the I-V characteristics for MAPDs with lower, normal, and higher operating voltages in the array. As shown on diagram, the breakdown voltage is at the point  $90 \pm 0.05$  V. Also, fig. 2 (right) shows the scatter of the operating voltage of photodiodes. The average value of the operating voltage was chosen of 93 V for all elements of the matrix.

For detecting the efficiency of gamma radiation with assembled matrix of MAPDs and scintillators, we used point sources Co-57, Cs-137, Eu-152 and Bi-207. The signal integration time was chosen corresponding to the decay time of the scintillator. For LYSO and YSO crystals, the signal integration time was 400 ns, and for BGO, it was 750 ns. The characteristic energy spectra for the LYSO and YSO scintillators are shown in fig. 3 (a) and (b), respectively.

Fig. 3 (c) shows the energy spectra for the BGO scintillator. The diagrams clearly show the main lines of gamma radiation of the used sources. The pulse height and energy resolution were determined from the peaks using a Gaussian function.

Using the data from the spectra, energy curves were constructed for the photodiode array. A linear dependence of the energies and the experimentally measured pulse heights was found fig. 4.

The calibration curve has a linear function. The results showed that the MAPD-based matrix showed good linearity over a wide energy range (30–1770 keV). This linearity can be explained by the high pixel density of the MAPD. Fig. 4 also allows determining the relative light output of the used scintillators, respectively to the relative light outputs given in Table 1.

Fig. 5 shows the function of the dependence of the energy resolution as a function of the energy of gamma radiation for all three scintillators. For gamma radiation with energy of 661.7 keV Cs-137, the energy

resolution was 9.25% (LYSO), 9.28% (YSO) and 14.33% (BGO). The BGO crystal showed low energy resolution due to its low light output.

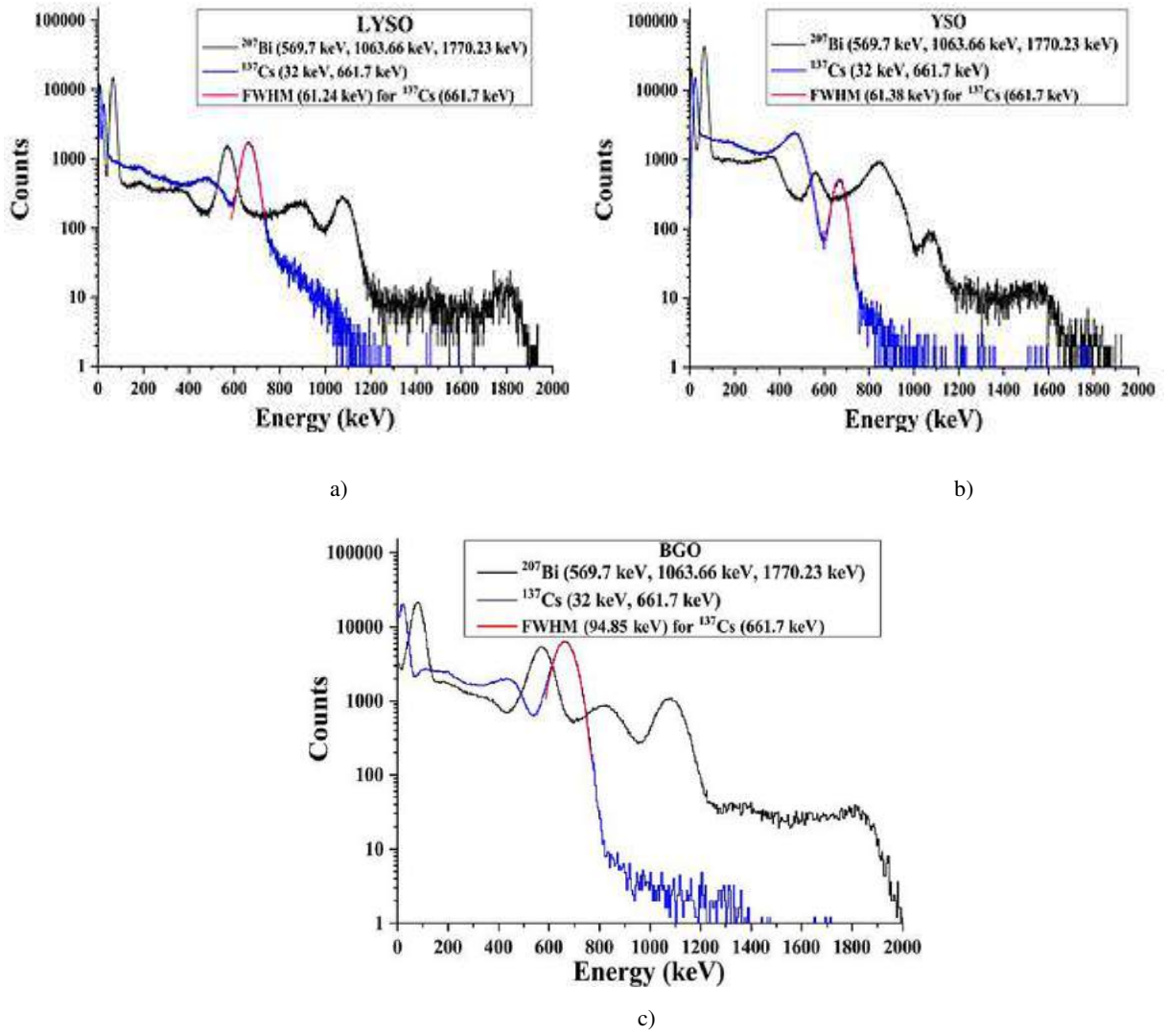


Fig. 3. Energy spectra of gamma radiation from Cs-137 and Bi-207 sources, measured by MAPD detectors and the scintillator LYSO (a) and YSO (b) and BGO (c).

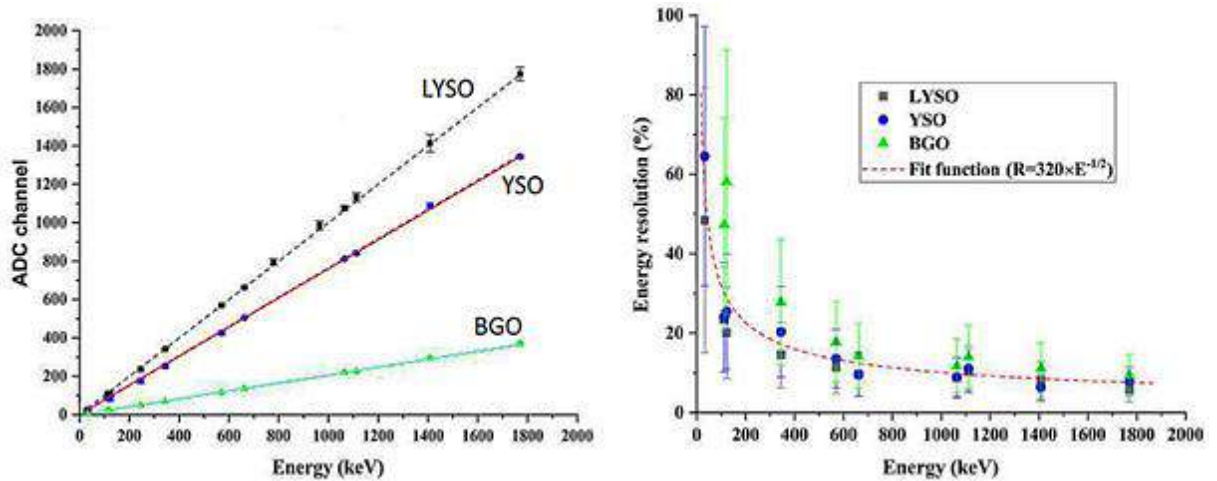


Fig. 4. The dependence of the ADC channel on the energy of gamma radiation.

Fig. 5. The dependence of the energy resolutions on the energies of Cs-137 gamma rays with an energy of 661.7 keV.

## CONCLUSION

A matrix of 9 elements based on MAPD photodiodes was assembled, the total active region of which was  $11,5 \times 11,5 \text{ mm}^2$ , and the gap between the individual elements was up to  $200 \text{ }\mu\text{m}$ . For the matrix test, LYSO, YSO, and BGO scintillators with a size of  $10 \times 10 \times 10 \text{ mm}^3$  were used. For Cs-137 gamma rays with energy of 662 keV, the energy resolution was 9.25% (LYSO), 9.28% (YSO), and 14.33% (BGO). The detector showed a good linearity between the ADC channels and the gamma radiation in the range up to 1770 keV. The energy resolution characteristics

for LYSO, YSO and BGO showed the same curve shape. The relative luminous efficiencies obtained by the LYSO, YSO, and BGO scintillators were in good agreement with the data of [8].

The results showed that a matrix of 9 MAPD photodiodes can be used as a light sensitive element in scintillation detectors in field of medicine, space industry and public safety. In addition, the high pixel density ( $10\,000 \text{ pixels/mm}^2$ ) of sensitive elements can be considered the most important advantage, which provides a fairly good linear response while maintaining PDE (40%).

- 
- |  |   |
|--|---|
| <p>[1] <i>D. Renker and E. Lorenz.</i> Advances in solid state photon detectors, 2009, JINST 4 P04004.</p> <p>[2] <i>N. Dinu et al.</i> Characteristics of a prototype matrix of Silicon PhotoMultipliers (SiPM), 2009, JINST 4 P03016.</p> <p>[3] <i>F. Ahmadov, G. Ahmadov, E. Guliyev, R. Madatov, A. Sadigov, Z. Sadygov et al.</i> New gamma detector modules based on micropixel avalanche photodiode, 2017, JINST 12 C01003.</p> <p>[4] <i>E. Garutti.</i> Silicon Photomultipliers for High Energy Physics Detectors, 2011, JINST 6C10003 [arXiv:1108.3166].</p> | <p>[5] <a href="http://zecotek.com/">http://zecotek.com/</a>.</p> <p>[6] <i>Z. Sadygov, A. Olshevski, I. Chirikov, I. Zheleznykh and A. Novikov.</i> Three advanced designs of micro-pixel avalanche photodiodes: Their present status, maximum possibilities and limitations, Nucl. Instrum. Meth. A 567, 70, 2006.</p> <p>[7] <i>Z. Sadygov, A. Ol'shevskii, N. Anfimov, T. Bokova, A. Dovlatov, V. Zhezher et al.</i> Microchannel avalanche photodiode with broad linearity range, Tech. Phys. Lett. 36, 528, 2010.</p> <p>[8] <a href="http://scintillator.lbl.gov/">http://scintillator.lbl.gov/</a>.</p> |
|--|---|

## FIRST PRINCIPLES STUDY Ge -DOPED MONOLAYER GRAPHENE

S.S. HUSEYNOVA

*Institute of Physics, 131 H. Javid, Baku Az-1143, Azerbaijan**E mail: suma\_huseynova.physics@mail.ru*

The electronic and structural properties of vacancy in graphene and doping of graphene with Ge calculated by the density functional theory (DFT) method within the Generalized Gradient Approximation (GGA). To simulate the vacancy effects have been studied 54 and 18 atom supercells to account for possible program software. Ferromagnetic spin ordering of vacancy of carbon atoms have been studied. It was shown that ferromagnetic ordering of the carbon atoms vacancies are located near the doping Ge atom. In addition DOS for 18 graphene atoms doped by Ge for s,p,d state have been calculated.

**Keywords:** *ab initio* calculation, DFT, ATK, graphene, Ge-doped, supercell, DOS, magnetic moment.

**PACS:** 31.10.+z, 31.15.E-, 75.50.Gg.

## INTRODUCTION

Graphene is obvious to have important properties, in occasion of electronic conductivity, thermal stability, structural flexibility, and surface area that make it well suited as a building block in 3D architectures. The [1] result gives that the graphene sheets can improve the electrochemical performances of nanostructured transition metal oxides as anode materials for lithium-ion batteries. Graphene satisfies as conductive channels; graphene nanosheets facilitate charge transfer during the cycling process by forming an electrically conductive network with nanoparticles [2]. Graphene demonstrates high electronic performance [3–5] optical properties [6] thermal performance [7], larger specific surface area [8, 9] excellent elastic modules [10]. Graphene has an unusual band structure which is practically important for electronic devices. In [11] work all cases, along with lithium adsorption, the bandgap energy is increased, so that the germanium doped compound has the highest bandgap and the structure with no doped atom has the least bandgap. In [12] work have given for this material semiconducting properties and to rate its altering energy gap. Equivalent to other 2D structures, like germanene [13], silicene [14], and phosphorene [15], it is expected that graphene may be useful for the development of leading-edge technologies.

The experimental synthesis of germanium-graphene nanocomposite material [16], which can represent for lithium-ion battery applications [17], and the simulation of low energy ion implantation of germanium into a graphene target, which may be useful for single-atom catalysis [18]. Theoretical studies using *ab initio* calculations constitute a important and convenient method to obtain valuable information about nanomaterials [19–22]. Al-doped graphene was theoretically found to significantly increase the adsorbing energy of CO molecule, where CO binds to the top site of Al [23].

There are two types of graphene doping: electrical and chemical [24]. Have been investigated [25] the chemical doping of graphene, where doping occurs via chemical routes, namely substitutional doping with heteroatoms. In the present contribution, it is investigated the effects of the germanium doping

on the properties of graphene 54 and 18 atom supercells using first principles calculations.

## MODEL AND CALCULATION METHOD

The calculations have been performed using the periodic using Atomistix Tool Kit (ATK) [26] implementing the spin-polarized DFT, PAW (projector-augmented wave method) and the PBE (Perdew–Burke–Ernzerhof exchange-correlation functional) [27].

Our calculations were performed for the primitive cell of Graphene and for a number of supercells with as many atoms as 54 by implementing the density functional theory (DFT) method within the Generalized Gradient Approximation (GGA) [28] and using the Atomistix Tool Kit program software. The Perdew–Burke–Ernzerhof (PBE) exchange-correlation functional (PBE) and Double Zeta Polarized basis sets were used in our calculations. The kinetic cut-off energy was 150 Ry. The primitive cell of Graphene was relaxed and optimized with force and stress tolerances of 0.01 eV/Å and 0.01 eV/Å<sup>3</sup>, respectively.

## Ge DOPED AND VACANCIES IN GRAPHENE

To simulate the doping and vacancy effects we have studied bulk compound and its 54 atom graphene supercell. The following shares in the total magnetic moment are derived from Mulliken population analysis in the case of atom vacancy: 1.232  $\mu$  ( $\mu_B$ ), where  $\mu_B$  is the Bohr magneton.

Fig. 1 shows the atomic structure of the vacancy in the 54 atoms graphene supercells and displays the density of states (DOS). The presence of carbon vacancies leads to acquired magnetic moment. 26<sup>th</sup> carbon atom acquires magnetic moment in the preferred direction  $\mu(C) = (0.32 \mu_B)$ . We established that acquired magnetic moments are: 3<sup>rd</sup> carbon atom ( $0.32 \mu_B$ ), 21<sup>th</sup> ( $0.32 \mu_B$ ), 26<sup>th</sup> ( $0.327 \mu_B$ ), 9<sup>th</sup> ( $0.101 \mu_B$ ), 15<sup>th</sup> ( $0.101 \mu_B$ ) in the preferred direction, actually  $\mu(C) = 8^{\text{th}}$  ( $-0.035 \mu_B$ ), 31 ( $-0.036 \mu_B$ ), 49<sup>nd</sup> ( $-0.036 \mu_B$ ), and 14<sup>th</sup> carbon atom ( $-0.033 \mu_B$ ) on the opposite direction.



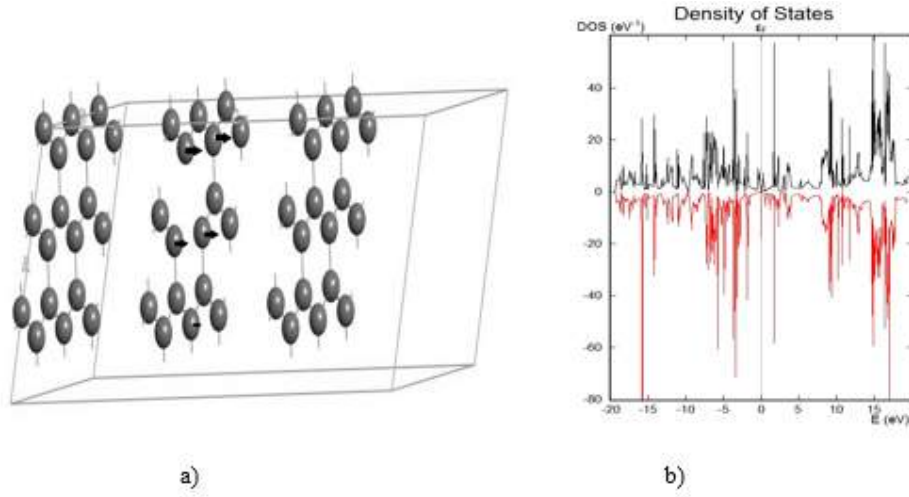


Fig. 1. The structure of defects in (a) supercell 54 atoms graphene with carbon vacancy and (b) DOS.

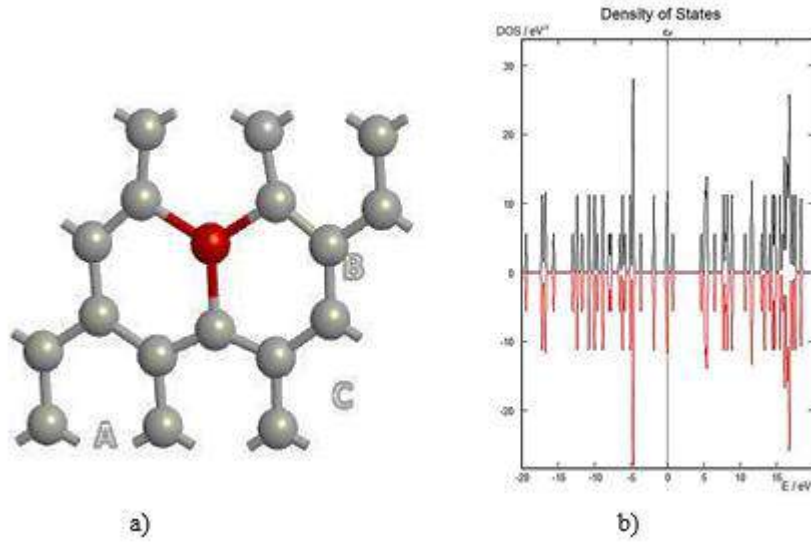


Fig. 2. (a) Atomic structure of 18 atom doped by Ge graphene and (b) density of state (DOS).

Fig. 2 displays the atomic structure of the Ge doped graphene plane and density of state (DOS).

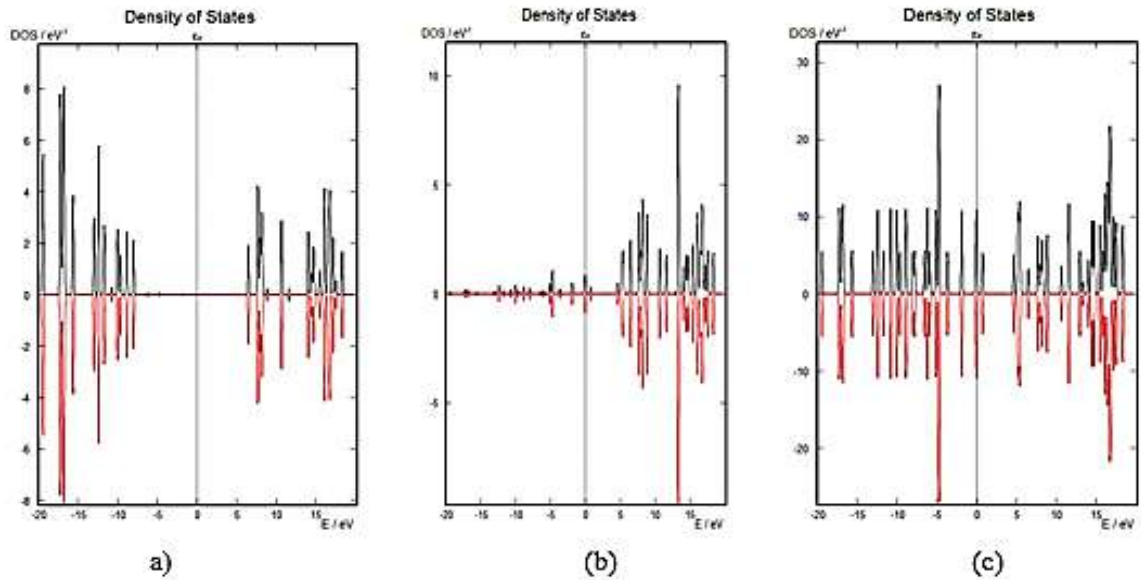


Fig. 3. The DOS for spin up and spin down d-, s-, and s p-electrons of the dopant Ge atom in the 18 atoms supercell: a) d- state, b) s-state, c) s p-state.



Fig. 3 shows the DOS for d-, s-, and -s p electrons of dopant Ge atom in the graphene supercells. The upper curve corresponds to electrons

with the direction of the spin up, and the lower with the direction of spin down.

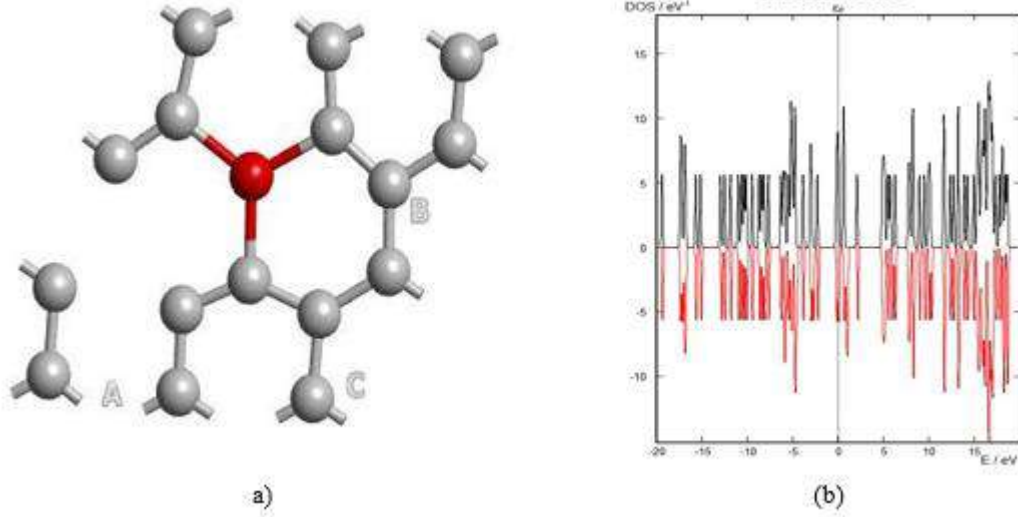


Fig. 4. (a) Atomic structure of the vacancy (Ge doped) and C vacancy in the graphene plane and (b) density of state (DOS).

Fig.4 displays the atomic structure of the Ge doped (a) graphene plane with C vacancy and (b) density of state (DOS).

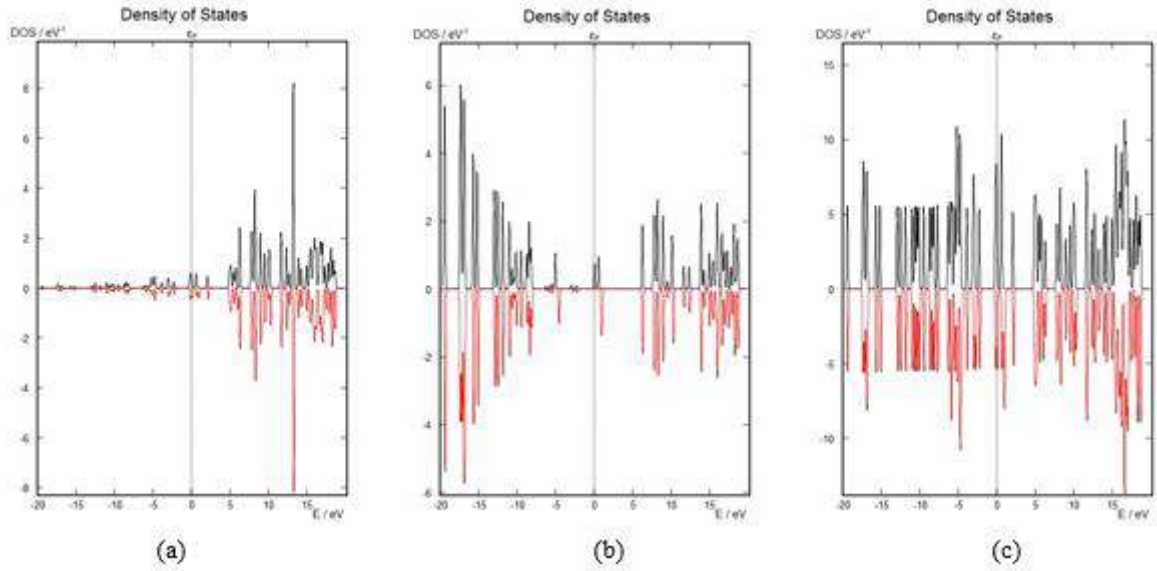


Fig. 5. The DOS for spin up and spin down d-, s-, and s p-electrons of the dopant Ge atom and C vacancy in the 18 atoms supercell : a) d-state, b) s-state, c) s p-state

Fig. 5 shows the DOS for d-, s-, and -s p electrons of dopant Ge atom and C vacancy in the graphene. Observed for the spin-down and spin up d-states below the Fermi level.

Si was the least effective element at opening the band gap, Ge ( $r = 1.23 \text{ \AA}$ ) is a little more effective than Si ( $r = 1.18 \text{ \AA}$ ), probably due to its larger size, which can induce more distortion than Si in the  $sp^2$  C ( $r = 0.77 \text{ \AA}$ ) framework [29].

The total magnetic moment in the supercell Ge doped graphene and C vacancy:  $0.998 \mu (\mu_B)$ . In case of Ge substitution C and in presence of C-vacancy which positioned near the dopant Ge atom creates magnetic moment  $0.031 \mu_B$ . Near the vacancy

$0.48 \mu (\mu_B)$  and the Ge additives  $0.031 \mu (\mu_B)$ , carbon atoms gained more magnetic moment.

## CONCLUSIONS

The structural, electronic, and magnetic properties of Ge-doped graphene was studied using DFT calculations. Band structure and density of states Ge-doped, vacancy case of monolayer graphene are shown. To simulate the doping effect, we have performed our calculations for 54 atom graphene and Ge doped 18 atom-contained supercells. It has been established that doping the monolayer of graphene leads to a significant altering its electronic properties.

Mulliken population analysis shows that the presence Ge- doped and carbon vacancy state graphene supercell acquire  $\mu(C) = (0.998 \mu B)$  magnetic moment.

The presence vacancy graphene supercell acquired magnetic moment of the carbon near the

vacancy is noticeably larger  $\mu(C) = (0.998 \mu B)$  than that of the other without vacancy state  $\mu(C) = (0.001 \mu B)$ . In the presence of Ge-doped and no vacancies in supercell,  $E_g = 0.505 \text{ eV}$ , while Ge-doped and vacancies  $E_g = 0.21 \text{ eV}$ .

- [1] P. Lian, X. Zhu, H. Xiang, Z. Li, W. Yang, H. Wang. Enhanced cycling performance of Fe<sub>3</sub>O<sub>4</sub> – graphene nanocomposite as an anode material for lithium-ion batteries. *Electrochim Acta*, 56:834-840, 2010. doi:10.1016/j.electacta.2010.09.086.
- [2] AK Rai, J. Gim, LT Anh, J Kim. Partially reduced Co<sub>3</sub>O<sub>4</sub>/graphene nanocomposite as an anode material for secondary lithium ion battery. *Electrochim Acta*, 100:63-71, 2013. A simple and rapid urea-assisted, auto-combustion approach for the synthesis of high-performance Co<sub>3</sub>O<sub>4</sub>/graphene nanocomposite anode is reported, DOI:10.1016/j.electacta.2013.03.140.
- [3] C.W.J. Beenakker. Colloquium: Andreev reflection and Klein tunneling in graphene, *Rev. Mod. Phys.*, 2008, 80, 1337–1354, DOI: <https://doi.org/10.1103/RevModPhys.80.1337>.
- [4] A.H. Castro Neto, F. Guinea, N.M.R. Peres, K.S. Novoselov and A.K. Geim. The electronic properties of graphene, *Rev. Mod. Phys.*, 2009, 81,109–162, DOI: 10.1103/RevModPhys.81.109.
- [5] S.D. Sarma, S. Adam, E.H. Hwang and E. Rossi. Electronic transport in two dimensional graphene. *Rev. Mod. Phys.*, 83, 407–470, 2011. DOI: <https://doi.org/10.1103/RevModPhys.83.407>.
- [6] R.R. Nair, P. Blake, A.N. Grigorenko, K.S. Novoselov, T.J. Booth, T. Stauber, N. MR. Peres and A.K. Geim. Fine structure constant defines visual transparency of graphene, *Science*, 320, 1308, 2008. doi: 10.1126/science.1156965.
- [7] A.A. Balandin, S. Ghosh, W. Bao, I. Calizo, D. Teweldebrhan, F. Miao and C.N. Lau. Superior thermal conductivity of single-layer graphene, *Nano Lett.*, 8, 902–907, 2008. doi/10.1021/nl0731872.
- [8] B. Luo, B. Wang, X.L. Li, Y.Y. Jia, M.H. Liang and L.J. Zhi. Graphene-confined Sn nanosheets with enhanced lithium storage capability, *Adv. Mater.*, 24, 3538–3543, 2012. DOI: 10.1002/adma.201201173.
- [9] C.H. Xu, B.H. Xu, Y. Gu, Z.G. Xiong, J. Sun and X.S. Zhao. Graphene-based electrodes for electrochemical energy storage, *Energy Environ. Sci.*, 6, 1388–1414, 2013 DOI: 10.1002/adma.201201173.
- [10] C. Lee, X.D. Wei, J.W. Kysar and J. Hone. Measurement of the elastic properties and intrinsic strength of monolayer graphene, *Science*, 321, 385–388. 2008. doi: 10.1126/science.1157996.
- [11] M.M. Loghavia, b, H. Mohammadi-Maneshb, R. Egraa, A. Ghasemia and M. Babaieea. DFT Study of Adsorption of Lithium on Si, Ge-doped Divacancy Defected Graphene as Anode Material of Li-ion Battery *Phys. Chem. Res.*, Vol. 6, No. 4, 871-878, December 2018. DOI: 10.22036/pcr.2018.148943.1543.
- [12] S.S. Huseynova. AB initio study of Si -doped monolayer graphene, *Transactions of National Academy of Science of Azerbaijan, series of physics-mathematical and technical, Physics and Astronomy*, № 2, 2020.
- [13] A. Acun, L. Zhang, P. Bampoulis, M. Farmanbar, A. van Houselt, A.N. Rudenko, M. Lingenfelder, G. Brocks, B. Poelsema, M.I. Katsnelson, and H.J.W. Zandvliet Germanene. The germanium analogue of graphene, *J. Phys.: Condens. Matter* 27, 443002 (11 pp), 2015. doi:10.1088/0953-8984/27/44/443002.
- [14] B. Lalmi, H. Oughaddou, H. Enriquez, A. Kara, S. Vizzini, B. Ealet, B. Aufray. Epitaxial growth of a silicene sheet, *Appl. Phys. Lett.* 97, 223109, 2010. <https://doi.org/10.1063/1.3524215>.
- [15] Z. Guan, W. Wang, J. Huang, X. Wu, Q. Li, J. Yang. Metal-Free Magnetism and Half-Metallicity of Carbon Nitride Nanotubes: A First-Principles Study, *J. Phys. Chem. C* 118, 39, 22491-22498, 2014. <https://doi.org/10.1021/jp508617k>.
- [16] E. Aktürk, C. Ataca, S. Ciraci. Effects of silicon and germanium adsorbed on graphene, *Appl. Phys. Lett.* 96, 123112, 2010; <https://doi.org/10.1063/1.3368704>
- [17] J.G. Ren, Q.H. Wu, H. Tang, G. Hong, W. Zhang, S.T. Lee. Germanium–graphene composite anode for high-energy lithium batteries with long cycle life, *J. Mater. Chem. A* 1, 1821 2013. <https://doi.org/10.1039/C2TA01286C>.
- [18] M. Tripathi, A. Markevich, R. Böttger, S. Facsko, E. Besley, J. Kotakoski, T. Susi. Implanting Germanium into Graphene *ACS Nano* 12, 4641, 2018. <https://doi.org/10.1021/acsnano.8b01191>.
- [19] M. Sajjad, N. Singh, U. Schwingenschlgl. Strongly bound excitons in monolayer PtS<sub>2</sub> and PtSe<sub>2</sub> *Appl. Phys. Lett.* 112, 043101 2018, <https://doi.org/10.1063/1.5010881>.

- [20] *N. Singh, Udo Schwingenschlögl.* A Route to Permanent Valley Polarization in Monolayer MoS<sub>2</sub>, *Adv. Mater.* 29(1), 1600970, 2017. DOI: 10.1002/adma.201600970.
- [21] *M.H. Mohammed, A.S. Al-Asadi, F.H. Hanoon.* Superlattices Microstructures 129, 14 -19 (2019) Electronic structure and band gap engineering of bilayer graphene nanoflakes in the presence of nitrogen, boron and boron nitride impurities, DOI:10.1016/j.spmi.2019.03.012.
- [22] *M.H. Mohammed, A.S. Al-Asadi, F.H. Hanoon.* Solid State Commun. 282, 28-32, 2018. Semi-metallic bilayer MS<sub>2</sub> (M= W, Mo) induced by Boron, Carbon, and Nitrogen impurities, Solid State Communications, Pub.Date : 2018. DOI: 10.1016/j.ssc.2018.07.011.
- [23] *Z.M. Ao, J. Yang, S. Li and Q. Jiang.* Enhancement of CO detection in Al doped graphene *Chem. Phys. Lett.*, 2008, 461, 276, <https://doi.org/10.1016/j.cplett.2008.07.039>.
- [24] *Lv Ruitao and M. Terrones.* Towards new graphene materials: Doped graphene sheets and nanoribbons, *Mater.Lett.* 78, 209-218, 2012. DOI:10.1016/j.matlet.2012.04.033.
- [25] *M Yu Arsent'ev, A V Prihodko, A V Shmigel, T L Egorova and M V Kalinina.* Doping graphene with a monovacancy: bonding and magnetism, *Journal of Physics: Conference Series* 661, 012028, 2015. doi: 10.1088/1742-6596/661/1/012028 <http://quantumwise.com>.
- [26] *M. Ernzerhofa and G.E. Scuseria.* Assessment of the Perdew–Burke–Ernzerhof exchange–correlation functional, *Journal of Chemical Physics*, v.110, No 11. 5029-5036, 1999.
- [27] *S.A. Tolba, K.M. Gameel, B.A. Ali, H.A. Almossalami and N.K. Allam.* The DFT+U: Approaches, Accuracy, and Applications, 2018. DOI:10.5772/intechopen.72020. <https://www.sciencedirect.com/topics/chemistry/generalized-gradient-approximation>, 1-30.
- [28] *A. Pablo Denis.* Chemical Reactivity and Band-Gap Opening of Graphene Doped with Gallium, Germanium, Arsenic, and Selenium Atoms, DOI: 10.1002/cphc.201402608, 2014. Wiley-VCH Verlag GmbH & Co. KGaA, Weinheim.

*Received: 10.03.2020*

# DIELECTRIC PROPERTIES OF $\text{Ba}_{0.8}\text{Sr}_{0.2}\text{TiO}_3$ IN HEATING AND COOLING PROCESSES

A.E. NABIYEV

*Azerbaijan State Pedagogical University  
68, U. Hajibeyov str., Baku, Azerbaijan, 1000*

The temperature dependences during heating and cooling processes of the dielectric properties of the metal- dielectric-semiconductor (MDS) structure based on ferroelectric  $\text{Ba}_{0.8}\text{Sr}_{0.2}\text{TiO}_3$  films deposited on silicon substrates (*n*-type 3KEF and *p*-type 4KDB) by high-frequency sputtering in the crystallographic direction (100) are studied in the temperature range 300-440 K. Several relaxation-type phase transitions associated with the ferroelectric property of these crystals are discovered.

**Keywords:** ferroelectric film, metal-dielectric- semiconductor, heating, cooling, dielectric constant, dielectric loss tangent.

**PACS:** 77.80.-e

## INTRODUCTION

Currently, one of the promising areas of modern materials science is the creation of new multifunctional materials. Last years, the sharp increase in investigations directed on development of ferroelectric nonvolatile memory with random access [1, 10, 13] has been observed. Such materials have been successfully used in super high frequency (SHF) electronics, including high-voltage pulse technology. In this regard, the use of ferroelectrics as a high-energy-containing materials in the field of electronic devices is relevant. Therefore, the use of ferroelectric films has been recently begun to expand rapidly. It should be noted that in modern microelectronics, SHF electronics is of great practical interest. In this regard, the field of special applications to the category of mass consumption, such as cellular telephony, satellite television, acoustoelectronic devices, etc., is the global information network [2, 8, 11, 12]. Information on the electrophysical properties ( $C$ ,  $R$ ,  $\rho$ ,  $\sigma$ ,  $\varepsilon$ ,  $\text{tg}\delta$ ) of multilayer heterostructures, including high values of the high dielectric constant of the films containing ferroelectrics, including  $\text{Ba}_{0.8}\text{Sr}_{0.2}\text{TiO}_3$ , plays a particularly important role. Measurements of dielectric properties show that the obtained structures are promising for the construction of spin-wave devices for processing of SHF signals [1, 5, 6, 7, 11]. In this regard, at the investigation of new multifunctional ferroelectric materials it is necessary to have information on the temperature and frequency dispersion of the real ( $\varepsilon'$ ) and imaginary ( $\varepsilon''$ ) parts of the complex dielectric constant ( $\varepsilon$ ), the dielectric loss tangent ( $\text{tg}\delta$ ), the electrical conductivity at constant ( $\sigma_{dc}$ ) and alternating ( $\sigma_{ac}$ ) electric fields, and the basic laws of variation of these parameters and the dielectric relaxation spectrum.

It should be noted that in work [2] it was shown that a planar condenser in medium-power SHF devices operates in severe temperature conditions, as well as on the basis of calculations critical operating modes of the capacitor were estimated at frequencies of 3-15 GHz at different powers. The purpose of this work is to study the dielectric properties of  $\text{Ba}_{0.8}\text{Sr}_{0.2}\text{TiO}_3$  in heating and cooling processes at a

temperature of (293-493K) in alternating electric field.

## EXPERIMENTAL TECHNIQUE

As objects of study, we synthesized MDS structures, which are a *p*- and *n*-type silicon substrate, a  $\text{Ba}_{0.8}\text{Sr}_{0.2}\text{TiO}_3$  ferroelectric film, and an upper nickel electrode. The thickness of the silicon substrates was  $200 \pm 2 \mu\text{m}$ , and the crystallographic orientation was (100). The ferroelectric film was deposited on a silicon substrate by high-frequency sputtering of a polycrystalline target in an oxygen atmosphere using a Plasma-50SE installation. The design of the installation and the technique of film deposition are given in [2].

The upper nickel electrode was deposited onto the ferroelectric film by the electron beam method through a shadow mask. The contacts area was  $2.7 \times 10^{-4} \text{ cm}^2$ , and the thickness was  $0.1 \mu\text{m}$ . Two MDS structures on *p*-type silicon (3KDB, 4KDB) type silicon) and two MDS structures on *n*-type silicon (3KEF, 4 KEF) were fabricated. Under similar technological conditions, a ferroelectric film was applied to the 4 KEF and 4 KDB substrates during 15 minutes, and to the 3 KEF and 3KDB substrates during 20 minutes. The thickness of the ferroelectric film plus the  $\text{SiO}_2$  insulating layer was  $450 \pm 10 \text{ nm}$  and  $480 \pm 10 \text{ nm}$ , respectively. The electrophysical properties of MDS structures were measured using an E7-20 LCR meter. The frequency range is  $25\text{-}10^6 \text{ Hz}$  [9]. The values of the real and imaginary parts of the dielectric constant were calculated based on the thickness of the ferroelectric film  $d$  and the contact area  $S$  according to the formulae for a flat capacitor  $\varepsilon' = c \cdot d / \varepsilon_0 S$  and  $\varepsilon'' = \text{tg}\delta \varepsilon'$  at the voltage  $U = 1 \text{ V}$ .

## EXPERIMENTAL RESULTS AND THEIR DISCUSSION

It is known that mechanical stresses can significantly affect on the temperature dependences of the dielectric constant  $\varepsilon(T)$  and the dielectric loss tangent  $\text{tg}\delta = f(T)$ .

It is shown that the obtained structures are promising for the construction of spin-wave devices for processing of SHF signals. It should be noted that each ferroelectric material has a number of peculiar electrophysical properties. It is known [1, 4, 7, 14] that ferroelectrics are called polar dielectrics, which in a certain temperature range possess spontaneous polarization. Obtaining of ferroelectric materials is one of the important tasks to predict the effects of external factors (external electric fields, temperatures, pressure, humidity, ionizing radiation, etc.). Fig. 1-4 shows the dependences  $\varepsilon' = f(T)$  and  $\text{tg}\delta = f(T)$  at heating and cooling of 3KEF and 4 KDB samples.

In [3, 4] it is shown that various scattering processes make contributions to the value of  $\text{tg}\delta$ ; these contributions are important in the research of low-loss microwave dielectrics. This makes it possible to use these ferroelectrics in microwave electronics, including high-voltage pulse technology. Fig. 1 shows the  $\varepsilon' = f(T)$  dependence of 3KEF sample with MDS structure during heating and cooling.

As seen in the process of heating (fig. 1. 3KEF), with increase the of the temperature there is observed an increase in the value of  $\varepsilon'$ , spontaneous polarization is observed in the polar phase at temperatures below the Curie temperature. At  $T=393\text{K}$ , the Curie temperature is maximized and the phase transition is manifests itself. Let's also note that, regular and irregular transitions, typical for the ferroelectricity depend on the structure elements (molecules, ions and radicals) of the crystal and these structure elements may be in two or more equilibrium states. It's on its turn characterized by a dipole moment. In the temperature above the Curie temperature in the nonpolar phase,  $\varepsilon'$ , along with the dependence from the temperature, also depends on the field voltage. In the high-temperature area (after the temperature of the Curie), with increasing of energy, the dipole-dipole interaction increases as a result of the heat flux and every instant, the dipoles are randomly directed, as a result, the total polarization equals to zero (total dipole moment  $P=0$ ) and ferroelectricity in the non-polar phase behaves like a dielectric. Now, if we look at the reverse process, we will see that with decreasing of the temperature due to dipole-dipole interactions in the phase transition, the formation of elements with a regular polar structure takes place in itself, therefore, spontaneous polarization and  $P>0$  occur in the ferroelectric samples under study. Note that a phase transition at  $T=393\text{K}$  also occurred during the cooling process.

Temperature dependence of tangent of dielectric loss angle ( $\text{tg}\delta = f(T)$ ) on the heating and cooling processes is given in fig. 2. Here if we see curve 2, we can observe creation of several maxima ( $T=363\text{K}$ ,  $T=393\text{K}$ ) and this is can be connected with several Curie temperatures, which is characteristic with ferroelectrics. The dependences  $\varepsilon' = f(T)$  and  $\text{tg}\delta = f(T)$  of the 4KDB sample in heating and cooling processes are given in fig. 3 and fig. 4. Here the same tendency manifests itself in the same way as the previous explanation. Here, also in the curve in fig. 3,

depending on the temperature the formation of several maxima is observed, which also characterizes the phase transitions arising from ferroelectric properties and being of the process - relational type. This is characteristic of the dependence of the electrophysical properties of the MSD crystalline system on both temperature and frequency.

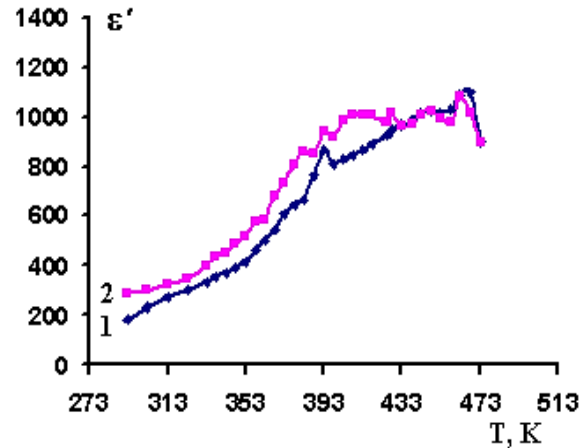


Fig. 1.  $\varepsilon' = f(T)$  dependence for 3KEF in heating and cooling processes. 1 is heating, 2 is cooling.

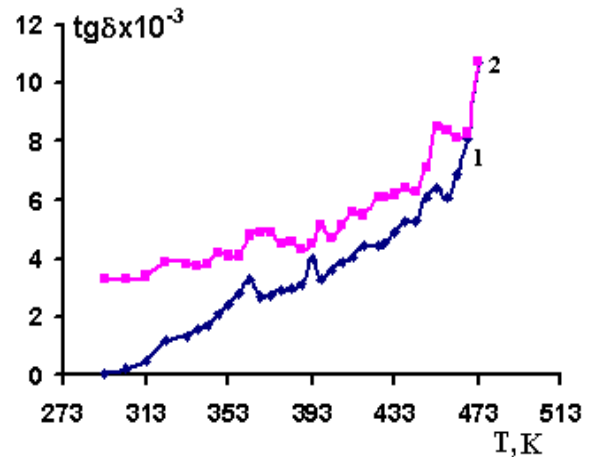


Fig. 2.  $\text{tg}\delta = f(T)$  dependence of 3KEF in heating and cooling processes. 1 is heating, 2 is cooling.

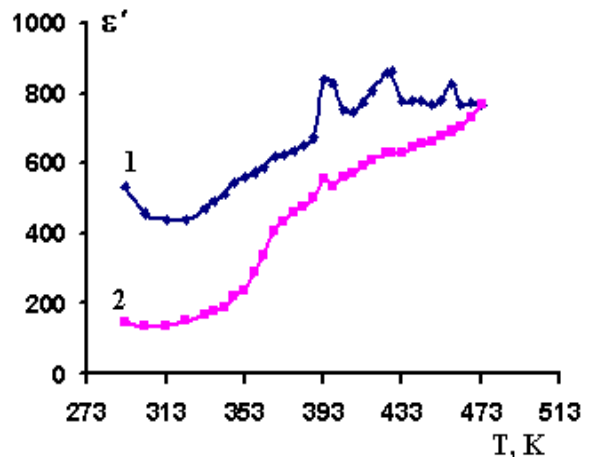


Fig. 3.  $\varepsilon' = f(T)$  dependence of 4 KDB in the heating and cooling processes. 1 is heating, 2 is cooling.



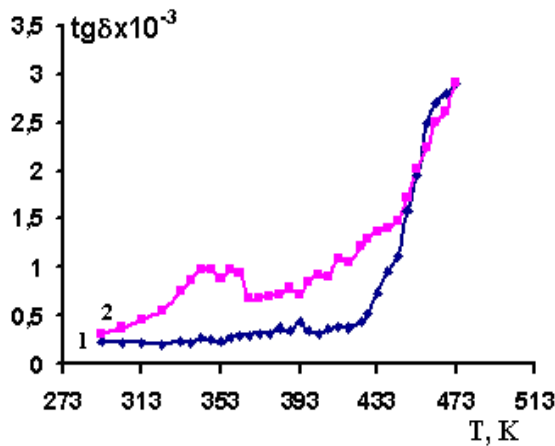


Fig. 4.  $\text{tg}\delta=f(T)$  dependence of 4KDB in heating and cooling processes. 1 is heating, 2 is cooling down.

Temperature dependence of the activation energy of relaxation processes during heating and cooling processes of 3KEF and 4KDB samples at 1 kHz is calculated with Arrhenius formula

$$E_{ak}=kT\ln(\tau/\tau_0) \quad (1)$$

here,  $\tau_0$  is characteristic relational time in the same arrangement with the dance phase of the atom ( $\tau_0 \sim 10^{-13}$  sec.),  $\tau$  is the duration of the external area and  $\tau=10^{-3}$  sec [15]. The activation energy of the relaxation process during the heating process increases from 1,02eV to 1,65eV in the temperature range 293÷473K. In the reverse cooling process the activation energy decreases.

As it is seen in fig. 1-4 during heating and back cooling processes the shifted maxima of the relaxation

process according to the corresponding temperature are observed

An increase in the activation energy upon heating and a decrease upon cooling is a common regularity for the measured dependences, this is also associated with a change in carriers energy due to temperature changes and so mean corresponds to a change in the Fermi status within the band gap of the material. Changes in the dielectric properties of this medium can lead to the release of trapped loads. On the other hand, a breakthrough may occur for new energy states in a MDS medium.

It should also be noted that as the temperature rises, the mobility of the structural elements of the samples also increases. The higher the molecular velocity, the greater the movement and turning angle of the domains in the electric field. Consequently, the dependence of the electrical conductivity and the tangent of the loss angle associated with it, the dielectric relaxation time and the activation energy of polarization processes at certain areas of the temperatures can be stepwise, what is seen in fig. 1-4. Here, on the curve of the cooling down process, the stepwise character is more noticeable (fig. 1-4, curve 2), this behavior can be explained by the phase transition in the material, i.e., the transition from the ferroelectric phase to the paraelectric phase.

## CONCLUSION

The results of the carried investigations show that in temperature dependence of dielectric properties of crystal with MDS structure (3KEF and 4KDB) the several phase transitions are observed. It is connected with the fact that these crystals have the ferroelectric properties.

- [1] G.V. Chucheva, M.S. Afanasyev, I.A. Anisimov, A.I. Georgieva, S.A. Levashov, A.E. Nabiev. Determination of planar capacitors based on thin-film ferroelectric material, News of the Saratov University, New series, V. 12 Ser. Physics, №2, p. 8-11, 2012.
- [2] D.A. Kiselev, M.S. Afanasyev, S.A. Levashov, G.V. Chucheva. Kinetics of the growth of induced domains in ferroelectric thin films  $\text{Ba}_{0.8}\text{Sr}_{0.2}\text{TiO}_3$ , PSS, V. 57, № 6, p.1134-1137, 2015.
- [3] A.S. Sigov, E.D. Mishina, V.M. Mukhortov. Thin ferroelectric films: production and prospects for integration, PSS, V. 52, № 4, p. 709-717, 2010.
- [4] Yu.A. Boykov, T. Klaeson. Dielectric response of (110)  $\text{Ba}_{0.8}\text{Sr}_{0.2}\text{TiO}_3$  films to changes in temperature and electric field, PSS, V 57, № 5, p. 945-949, 2015; PSS, 2015, V. 57, № 5, p. 945-949.
- [5] V.V. Shirokov, V.V. Kalinchuk, R.A. Shakhovoy and Yu.I. Yuzyuk. Physical properties of thin  $\text{Ba}_{0.8}\text{Sr}_{0.2}\text{TiO}_3$  films, PSS, V. 58, № 10, p. 1964-1968, 2016.
- [6] M.S. Ivanov, M.S. Afanasyev. Features of the formation of thin ferroelectric  $\text{Ba}_x\text{Sr}_{1-x}\text{TiO}_3$  films on various substrates by high-frequency sputterin, PSS, V. 51, № 7, p. 1259-1262, 2009.
- [7] M.S. Afanasyev, A.E. Nabiev, G.V. Chucheva. Optical monitoring of the deposition of ferroelectric films, PSS, V. 57, № 7, p 1354-1357, 2015.
- [8] Yu.M. Poplavko, L.P. Pereverzeva, I.P. Raevsky. Physics of active dielectrics. Rostov n/a: Publishing house of YFU, p. 480, 2009.
- [9] D.A. Golosov, S.M. Zavadsky, V.V. Kolos, A.S. Turtsevich. Ferroelectric properties of films of niobium-doped strontium-bismuth tantalate. PSS, V. 58, Issue 1, pp. 51-55, 2016.
- [10] Physics of ferroelectrics. A modern view. Edited by K.M. Rabe, C.G. An, J.M. Triskon, English translation 3rd edition, 443 p., Moscow, 2015.
- [11] O.S. Gefle, S.M. Lebedev, Yu.P. Pokholkov. Frequency spectra of the complex dielectric constant of composite dielectrics based on polyvinyl chloride. News of Tomsk



- Polytechnic University. V. 310, № 1, p. 87-91, 2007.
- [12] *M.A. Kudryashov, A.I. Mashin, A.A. Logunov, iG. Chidichimo, iG. De Filpo.* Dielectric properties of Ag/PAN nanocomposites. Technical Physics, v. 84, v. 7, p. 67-71, 2014.
- [13] *A.M. Solodukha, I.E. Shramchenko, A.M. Khoviv, V.A. Logacheva.* Dielectric properties of lead zirconate titanate films synthesized by oxidation of metal layers, PSS, V. 49, № 4, p. 719-722, 2007.
- [14] *V.M. Gurevich.* Conductivity of ferroelectrics, Edition of the Committee of Standards, Measuring Instruments under the Council of Ministers of the USSR, p. 383, 1969.
- [15] *N.M. Ushakov, A.N. Ulzutuev, I.D. Kosobudsky.* Thermoelectric properties of polymer composite nanomaterials based on copper-copper oxide in a high-pressure polyethylene matrix. Technical Physics, V.78, №12, p. 65-69, 2008.

*Received: 13.03.2020*

## INFLUENCE OF Nd IMPURITY ATOMS AND GAMMA IRRADIATION ON ROENTGENOGRAPHIC SPECTRUM OF GeS LAYERED SINGLE CRYSTAL

A.S. ALEKPEROV, A.A. NABIYEV, T.M. AYDINOVA

*Azerbaijan State Pedagogical University*

*68, U. Hajibeyov str., Baku, Azerbaijan, 1000*

*E-mail: aydin60@inbox.ru*

The roentgenograms of layered single crystals GeS and  $\text{Ge}_{0.995}\text{Nd}_{0.005}\text{S}$  before and after gamma irradiation are investigated. It is revealed that at identical conditions after gamma irradiation by dose 30 krad, the reflex intensity of GaS single crystal roentgenogram increases in 2,25 times and for  $\text{Ge}_{0.995}\text{Nd}_{0.005}\text{S}$  single crystal this value achieves up to 35. It is supposed that neodymium atoms form the complex aggregates in compositions of which the oxygen atoms consist in. The crystal temperature increases under the influences of quantum small doses and complexes are destroyed. As a result, the oxygen atoms leave the crystal, neodymium crystals take the cation vacancies migrating in crystal and this leads to crystal structure ordering.

**Keywords:** rare-earth elements, self-compensation irradiation, annihilation, associate, complexing.

**PACS:**72.40.+W, 76.30Kg, 78.20, 79.60.-i

### INTRODUCTION

The germanium monosulfide belongs to  $A^{IV}B^{VI}$  semiconductor class with conductivity of  $p$ -type and is characterized by orthorhombic crystal structure  $D_{2h}^{16}$  (structure type SnS, sp. gr.  $P_{cmn}$ ). GeS also has the layered crystal structure where the atomic layers are connected by only Van der Waals forces [1]. In this connection, the uncompleted electron levels are absent on GeS single crystal surface and because of it the material surface is characterized by high chemical stability.

The heightened interest to GeS layered crystals is caused by the possibility of their application in electric memory devices [2] in the capacity of the mediums for hologram recording [3], the formation of sun cells and detectors of linear-polarized radiation [4] on their base. The scientists of North Carolina University USA create the unique device from GeS in the form of flower. Because of its small size and thin structure, it allows us to increase the capacity of lithium-ion batteries in many times. Such material is used in the capacity of the raw material at production of compact sun super-condensers [5]. The single crystal tapes grown up by the method of chemical precipitation from gas phase on GeS base are perspective nano-materials for the devices with high sensitivity of visible light [6, 7].

The traditional approach on the expansion of region of semiconductor material practical use is based on the use of doping processes by the impurities. Moreover, the task is the right choice of doping impurity. In contrast to other impurities, the rare-earth element (REE) impurities are characterized by low solubility limit of crystal lattice and chemical activity [8, 9]. In result of Coulomb and chemical interactions with main substance atoms REE form the complexes of different types. Many complexes forming as a result of such interactions, have the enough high stability and influence on semiconductor properties, being the effective scattering centers of

ionizing radiations. The complex formation processes are obeyed by controlling interactions. The irradiation is the one of the controlling influence. Such opinion, which had been up to 80<sup>th</sup> of the former century that penetrating radiation causes only the radiation damages [10, 11] in semiconductor materials. The carried investigations establish that the radiation (in the dependence on semiconductor material) in definite doses can serve the effective technological method which allows us to obtain the high-quality semiconductor materials. The use of gamma irradiation is perspective in technological processes of semiconductor device preparation [12, 13]. The condition for structure ordering is formed at irradiation of semiconductor by gamma-quantums. The reliability of revealed effect is confirmed by X-ray and electron-microscopic investigations.

### SAMPLES AND INVESTIGATION METHODS

The germanium with resistivity  $50 \text{ Ohm}\cdot\text{cm}$ , sulfur by "B5" mark, neodymium "Hд-2" are used in the capacity of initial materials. The calculated stoichiometric weighted samples of these elements are put in quartz ampoules by length  $10\div 15 \text{ cm}$  and inner diameter  $1,0\div 2,0 \text{ cm}$ . The ampoule is evacuated up to pressure  $10^{-3} \text{ mm}$  of mercury and it is soldered. In order to avoid the explosion, the germanium is grinded in powder and substance quantity is limited by  $10\div 15 \text{ gr}$ .

The synthesis process is carried out in two stages. Firstly, the ampoule in the furnace is heated with velocity  $3\div 5 \text{ degree/min}$  up to  $300^\circ\text{C}$  and it is endured up to  $10\div 12 \text{ hours}$ . Further, the temperature is increased with velocity  $2\div 3 \text{ degree/min}$  up to total melting of germanium and ampoule is endured  $18\div 20 \text{ hours}$ .

Bridgman method is applied for growing of GeS and  $\text{Ge}_{0.995}\text{Nd}_{0.005}\text{S}$  single crystals. The temperature of top part of furnace is  $50^\circ\text{C}$  on higher and bottom of furnace is on  $50^\circ\text{C}$  less than melting point of the

corresponding substance. The ampoule lowering speed in furnace is 2÷3 mm/h that is the condition for formation of single crystals. The single crystals grow up in the form of plane-parallel plates by 10x8x0,1mm<sup>3</sup> dimension and needles. The layered single crystals obtained from big ingots are easily delaminated directly before measurements along plane perpendicular to *c* axis. They are not endured by the further mechanical and thermal treatment because of well mirror surface. The crystal melting point is

obtained by differentially-thermal analysis in installation “Perkin-Elmer”. The crystal structure and phase composition of materials are investigated by the method of roentgen beam diffraction with use of D8 ADVANCE diffractometer on CuK<sub>α</sub> ( $\lambda=1,5418\text{\AA}$ ) radiation [14, 15]. The data of X-ray investigations confirm the appliance of obtained crystals to orthorhombic syngony with parameters given in table 1.

Table 1

Parameters of alloy crystal lattice

Single crystals	<i>a</i> , Å	<i>b</i> , Å	<i>c</i> , Å
GeS	4.297	3.641	10.471
Ge <sub>0.995</sub> Nd <sub>0.005</sub> S	4.319	3.651	10.492
Ge <sub>0.995</sub> Nd <sub>0.005</sub> S (after irradiation)	4.332	3.645	10.485

The morphology of single crystals is investigated by screening method of electron microscopy on electron microscopy by SIGMA VP VAT mark. The sample irradiation by gamma quanta is carried out at room temperature on installation PXVH/D-20000 from source <sup>60</sup>Co with phase power in irradiation zone ~1,37 R/sec.

## THE INVESTIGATION RESULTS AND THEIR DISCUSSION.

The series of additional effects connected with defect formation because of the composition inclination from stoichiometric one appears at doping of GeS compounds by Nd atoms. The introduction in compound the substitutional impurity in essential quantities in Ge element sublattice leads to additional change of main component concentration in the crystal. At essential difference of introduced impurity atom dimensions ( $r_{\text{Nd}}=0,96\text{\AA}$ ) and replaced atom ( $r_{\text{Ge}}=0,72\text{\AA}$ ) the doping process can be accompanied by the generation of additional eigen point defects and change of their disposition form in the crystal. The big quantity of cation vacancies ( $10^{17}\div 10^{18}\text{cm}^{-3}$ ) essentially influence on introduction character of impurities in Ge lattice. In small concentration region Nd atoms directly dissolve in vacancies, the solubility in vacancies depends on vacancy concentration in initial material. The impurity solubility in vacancies is limited and it is always less than vacancy concentration. At the existence of free vacancies, it is possible the solubility of Nd impurity in essential quantities by the way of germanium exchange in lattice nodes. Taking under consideration these data one can suppose that the main mechanism of small concentration solubility of Nd impurity in germanium mono-sulphide leads to “recovering” of cation vacancies.

The one significant property-ability to make material “purification” at definite conditions is emphasized in semiconductors with investigation of electron structure of REE atoms. Moreover, one can decrease the background impurities in A<sup>4</sup>B<sup>6</sup>

compounds on 2÷3 order and essentially increase the electron mobility. The main difficulty with REE work is in their special chemical activity. REE are covered by the film of corresponding oxide the elimination of which is practically impossible.

It is obvious, that the real picture of defect formation in GeS at inclination from stoichiometry and doping has the complex character and consist in the complex formation of eigen point defects, impurity atoms, oxygen atoms. It is possible that because of Coulomb and chemical interactions, the formation of electro-neutral complexes Nd<sub>2</sub>O<sub>3</sub> in interstitial space of germanium mono-sulphide matrix which “pure” the crystals from impurities and eigen defects. As a result, the intensity of roentgen reflexes in Ge<sub>0.995</sub>Nd<sub>0.005</sub>S single crystal exceeds in ~2,5 times the corresponding reflexes of GeS single crystals before irradiation (fig. 1a and fig. 2a). The similar method is the one from technological methods for the obtaining of perfect crystals [16].

There are two opinions at explanation of crystal “purification”: 1 is that REE chemical reactions with background impurity take place in liquid phase, the forming compounds stay in slag and aren’t introduced in solid phase; the second one is that REE complexes with non-metal impurities introduce in growing crystal but they are electrically neutral one. Comparing the mobility of electrons in the crystals the authors [17] lead to conclusion on formation of REE micro-inclusions with non-metal impurities.

The main deceleration mechanisms are the elastic collisions with nuclei and inelastic collisions with electrons at transmission of high energy particles through crystals [18]. At enough high value of incident particle the target atom shift from angular position takes place that leads to appearance of interstitial atom and vacancy (Frenkel pairs).

In the beginning of 80<sup>th</sup> of former century it had been known that irradiation of crystals, metals and alloys by charged particles and gamma-quanta lead to destroy of their structure [19, 20]. It is the general accepted point of view according to which there are no changes take place at radiation by particle

fluxes which are less on several orders of charge carrier concentration value in semiconductor crystals [21, 22]. However, as a result of experimental investigations it is established that [23] the interaction process of ionizing radiation with crystals don't correspond to general accepted conceptions in the case when absorbed dose is  $\sim 10^5$  gr. The radiation of gamma-quantums by shown absorbed dose of ionizing radiation of semiconductor crystals leads not to defect accumulation and vice versa, to their elimination and ordering of material structure [24].

The crystal structure reconstruction at irradiation by small doses of gamma quanta takes place because of disposal of accumulated energy in the crystal. The decrease of defect quantity in the crystal in irradiation process is accompanied by heat

release caused by annihilation and defect reconstruction [25, 26].

In GeS crystal the dislocation loops which are formed at join of small associations of point defects under influence of gamma quanta, the defect concentration and micro-stresses decrease. The structure ordering under influence of gamma quanta takes place very weak and reflex intensity increases only in 2,25 times (fig. 1a, 1b).

The structure ordering effect in more bright form is revealed in GeS crystal by Nd doped atoms after irradiation by gamma quanta and intensity of super-structure maximum increases after irradiation by small dose 30 (krad) of  $\text{Ge}_{0.995}\text{Nd}_{0.005}\text{S}$  single crystal increases ( $\sim 35$  times) (fig. 2a, 2b).

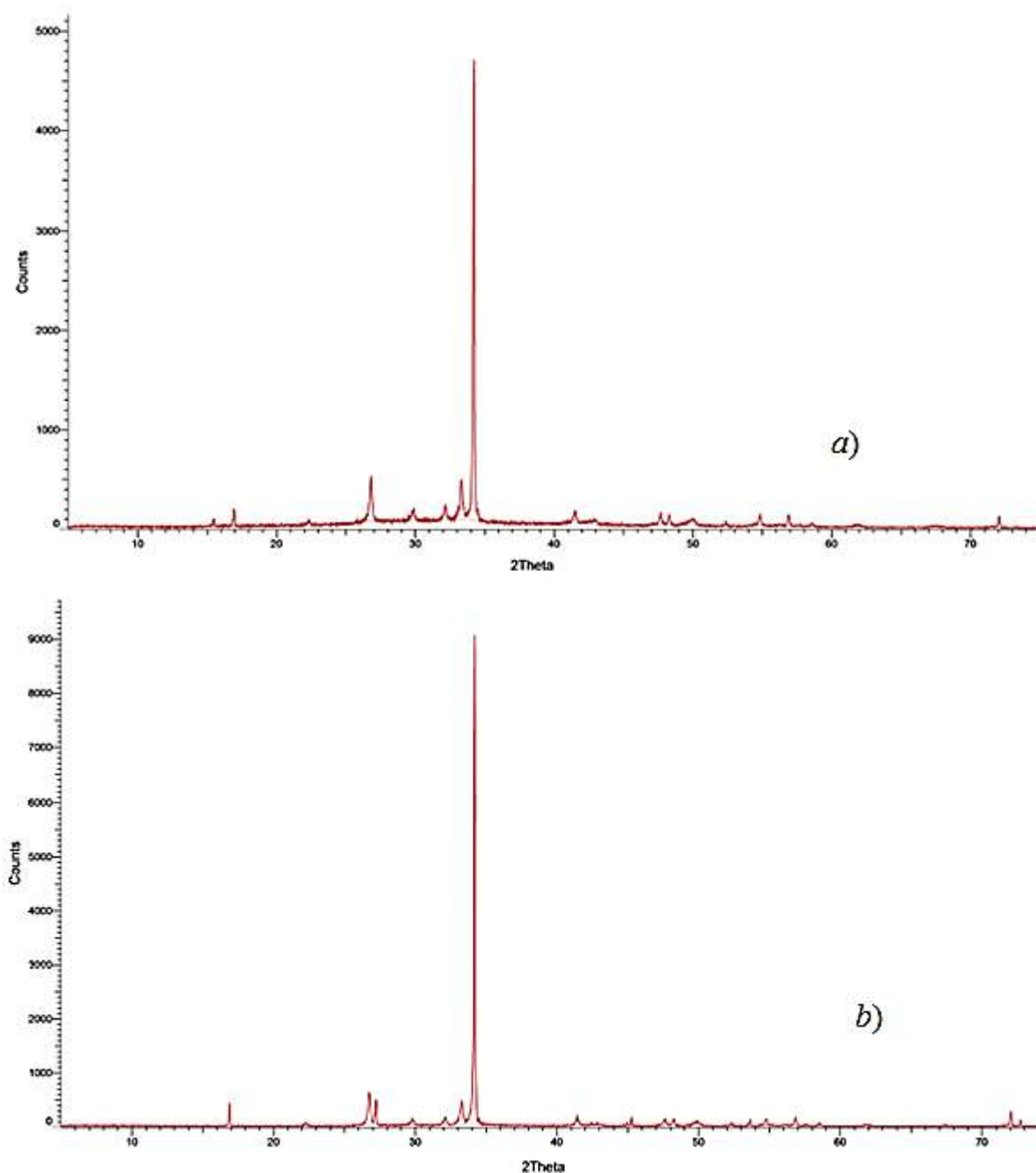


Fig. 1. Roentgenographic diffractograms of single crystals  
a) GeS before irradiation; b) GeS after irradiation by dose 30 krad.

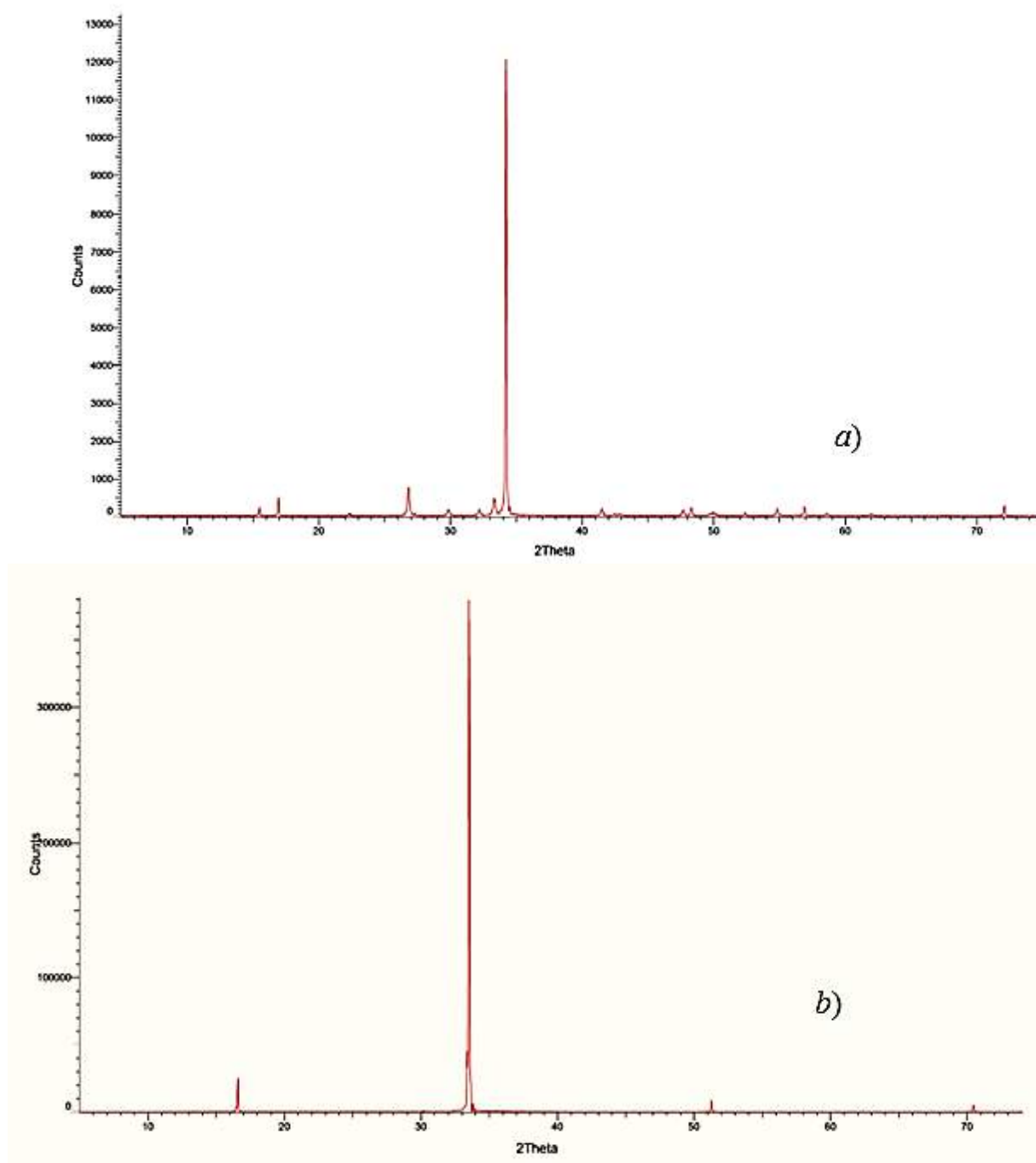


Fig. 2. Roentgenographic diffractograms of single crystals

a)  $\text{Ge}_{0.995}\text{Nd}_{0.005}\text{S}$  before irradiation; b)  $\text{Ge}_{0.995}\text{Nd}_{0.005}\text{S}$  after irradiation by dose 30 krad.

At the same time, as a result of joining of small associations of point defects the crystal blocks appear in crystal in the form of bright spots (fig. 3,a,b). The sizes of crystal blocks increase under the influence of gamma quanta (fig. 3c, d).

The picture of processes taking place in  $\text{Ge}_{0.995}\text{Nd}_{0.005}\text{S}$  single crystal at influence of gamma radiation of small doses (30 krad) one can explain by the following way. The gamma quanta create the electron-hole pairs in the crystal. These pairs in the semiconductor crystals exist the enough long time. Migrating along the crystal, they are captured by defects forming the charged interstitial atoms and

vacancies or their accumulations. The charged defects intensively interact between each other. The like defects join and form the bigger complexes of interstitial atoms and vacancies. In the case of unlike defect meeting the annihilation takes place and photon is formed at annihilation of electron and hole. Photon can interact with complexes and destroy them (in the composition of which REE and oxygen consist in). The released oxygen leaves the crystal and appeared free interstitial atoms annihilate with vacancies. At annihilation of Frenkel pairs the energy releases and the new electron-hole pairs appears because of this energy [27].

The described process changes the crystal state and leads to the crystal structure ordering. As it is seen from the table 1, the Nd impurity atoms and gamma irradiation of small dose insignificantly influence on elementary cell parameters and phase transformation isn't revealed. Thus,  $\text{Ge}_{0.995}\text{Nd}_{0.005}\text{S}$  crystal ordering

state where Nd atoms are in crystal lattice nodes, is formed under influence of gamma radiation of small dose. Note that that investigated effect is also observed in the example of single crystals  $\text{Ge}_{0.995}\text{Sm}_{0.005}\text{S}$  and  $\text{Ge}_{0.995}\text{Gd}_{0.005}\text{S}$ .

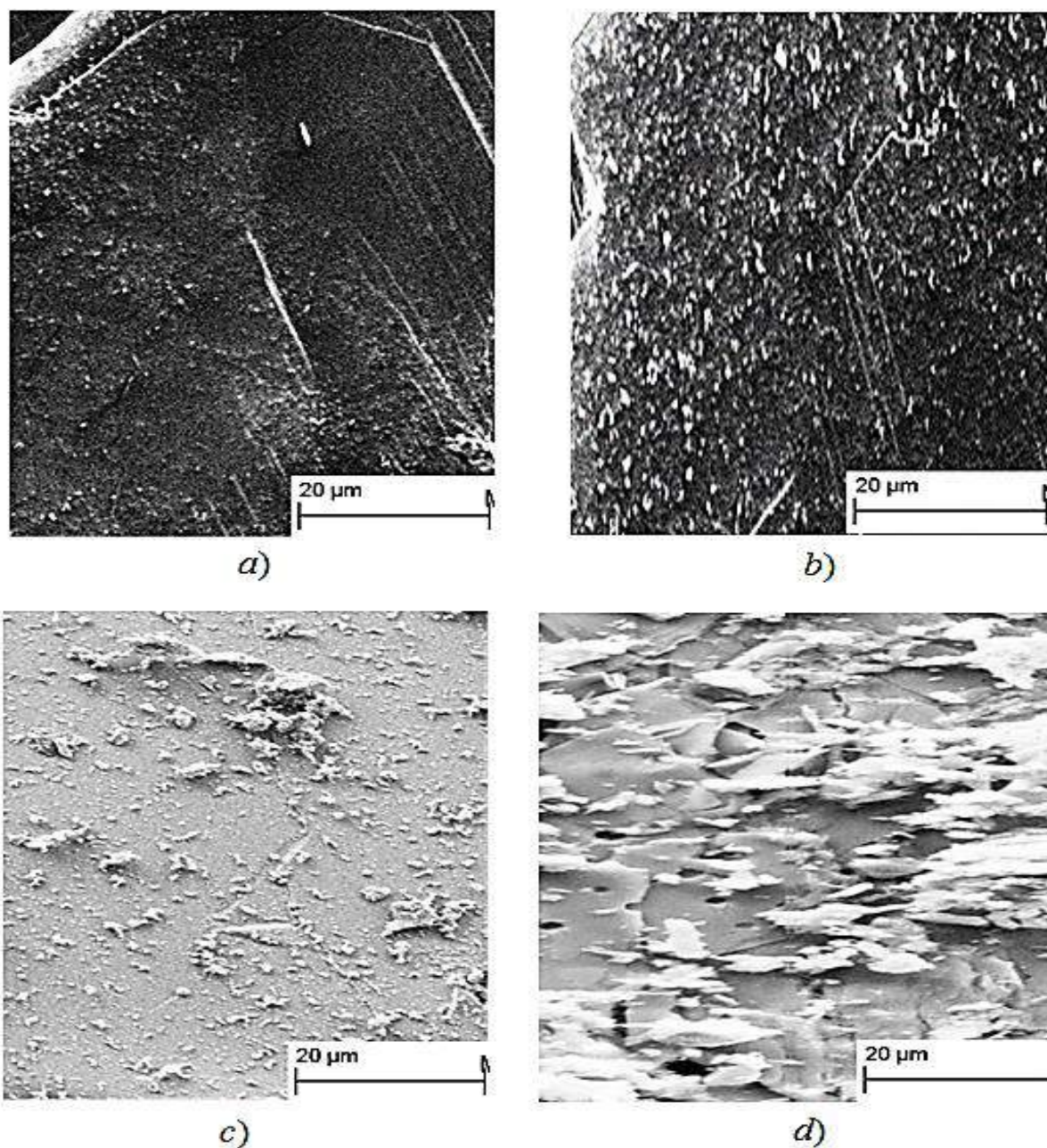


*Fig. 3. Micro-photos of single crystal surfaces*

- a) GeS before irradiation; b) GeS after irradiation by dose 30 krad;  
c)  $\text{Ge}_{0.995}\text{Nd}_{0.005}\text{S}$  before irradiation; d)  $\text{Ge}_{0.995}\text{Nd}_{0.005}\text{S}$  after irradiation by dose 30 krad.*

## CONCLUSION

Thus, summarizing the results of complex physical-chemical analysis one can conclude that the complex aggregates in the composition of which neodymium and oxygen atoms are included, form in  $\text{Ge}_{0.995}\text{Nd}_{0.005}\text{S}$  single crystals during crystal synthesis.

The crystal temperature increases and the destroy of these complexes takes place under the influence of gamma irradiation of small doses (30 krad). The oxygen atoms leave the crystal migrating along the substance, Nd atoms are captured by cation vacancies as a result of which  $\text{Ge}_{0.995}\text{Nd}_{0.005}\text{S}$  crystal structure ordering takes place.

- [1] Z.A. Jahangirli. Semiconductors, No.52, 436, 2010.
- [2] D.I. Bletska, V.I. Taran and M.U.Sichka. Ukrainian Journal of Physics, No 9,1436, 1976.
- [3] D.I. Bletska, I.F. Kopinets, P.P. Pogoretsky, et al., Crystallography, No.5, 1008, 1975.
- [4] D.I. Bletska, V.N. Kabatsiy, M.M. Bletska, Up-to-date Information Electronic Technology, Odessa, 228, 2015.
- [5] Chun Li, H. Liang, P. Gayatni, Yifei Yu, Linyou Cao, ACS Nano.V. 6, p. 8868, 2012.
- [6] Yong J.Ch., S.I. Hyung, M. Yoon, H.K. Chang, S.K. Han, H.B. Seung, R.L. Young, S.J. Chan, M.J. Dong, P. Jeung, Eun H. Ch., S.S. Min, Won J.Ch. Chemical Communications, V. 49. P. 4661, 2013.
- [7] K.U. Rajesh, L. Yi-Ying, K. Chia-Yung, R.T.Srinivasa, S. Raman, M.B. Karunakara, A.Ankur. Nanoscale. V. 8. p. 2284, 2016.
- [8] V.F. Masterov. Semiconductors. No. 9, 1435 1993.
- [9] K. Taylor, M. Darby. London, Chapman and Hall LTD, p. 378, 1972.
- [10] M.Tompson, D.Uolsh. Spectrometric Analysis Guide. M.: Nedra, p. 288, 1988 [in Russian].
- [11] V.S. Vavilov, N.A. Uchin. Radiation Effects in Semiconductors, L.: Nauka, p. 234, 1972 [in Russian].
- [12] I.I. Stroykov. Science Technical News of Information Technology, Mechanics and Optics. V. 16, p. 60-67, 2016.
- [13] A.Z. Abasova, R.S. Madatov, V. I. Stafeyev. Radiation- Stimulated ordering in Chalcogenides.: B, Elm, p. 352, 2010 [in Russian].
- [14] A.S. Alekperov. Journal of Advances in Physics. V. 10. p. 2795, 2015.
- [15] R.S. Madatov, A.S. Alekperov, Dzh.A. Maqerramova. Crystallography Reports, No. 60, 921, 2015.
- [16] I.P. Chernov, A.P. Mamontov. News of Tomsk Polytechnic University, p. 74-80, 2009
- [17] V.F. Masterov and L.F. Zakharenkov. Semiconductors. No. 4, 610, 1990.
- [18] Y.V. Astrova, V.V. Yemtsov, A.A. Lebedev, D.I. Poloskin, A.D. Remenyuk, Yu.V. Rud and V.Y. Khartsiyev. Semiconductors, No. 29, 1301, 1995.
- [19] V.T. Mack. Technical Physics Letters, No. 12, 17, 1989.
- [20] V.T. Mack. Technical Physics, No. 63, 173, 1993.
- [21] A.S. Belous, V.A. Soloducha, S.V. Shevedov. High Speed Electronic Devices, M.: Technosphere, p. 872, 2017 [in Russian].
- [22] K. Cenzual, L. Louise, M. Gelato, M. Penzo, E. Parthe. Acta Crystallography, V.47, p. 433, 1991.
- [23] A.P. Mamontov, I.P. Chernov. Effect of Small Doses of Ionizing Radiation, Tomsk.: Deltaplan, p. 288, 2009 [in Russian].
- [24] I.P. Chernov, A.P. Mamontov, A.A. Botaki. Atomic Energy, V. 57, p. 56-58, 1984.
- [25] I.P.Chernov, A.P.Mamontov, P.A. Chervantsev. Physics, V. 12, p. 58-66, 1994.
- [26] D.W. Zhang, F.T. Jin, J.M. Yuan. Chin. Phys. Lett., V. 2, p. 1876, 2006.

Received: 16.03.2020



## DEPOSITION OF NANODROP PHASE FROM EMITTER TIP ON NEARBY MOBILE SURFACE

**L.S. GASANOV**, S.A. ALIYEV, I.I. GURBANOV,  
E.M. AKBEROV, F.E. MAMEDOV, A.H. KERIMOVA

*G.M. Abdullayev Institute of Physics of NAS Azerbaijan  
33, H. Javid ave., Baku, Azerbaijan, AZ-1143*

The formation processes of low-sized structures by the means of fine-dispersed phase of liquid metal ion source (LMIS) are considered. The emitting tip is located in close distance from moved surface with the aim of deposition of narrow stripes. At distance tip – surface near 80  $\mu\text{m}$  on the axis of thin and wide traces of ( $\text{In}^+$ ,  $\text{Sn}^+$ ) ions the massive continuous paths by width of several microns are obtained. The structure of deposited stripes by the length more than 10 mm is the grain structure. At further approach of tip to surface the path melts because of high density of ion current and heterogeneous profile of its cross-section becomes smooth. For deposition of narrower structures, it is necessary the effective cooling of conducting mobile substrate.

**Keywords:** liquid metal ion source, field emission, nanoparticle.

**PACS:** 29.26.Ni;79.20.Rf

### INTRODUCTION

The nanodrop deposition on conducting surface is very perspective method for the creation of different surface structures. For this purpose, the liquid metal ion sources are used. The generation of charged drops on certain conditions takes place in liquid metal ion sources along with ion field emission [1]. If divergence angle of ion beam achieves  $90^\circ$  then the divergence of drop flux is  $3-4^\circ$  [2]. The size of ion emission zone is near 5 nm that confirms the high original density of ion current and small sizes of generated drops. The sizes of the least charged drops are obtained from the condition of Ray stability [3]:

$$\frac{E^2}{8\pi} > \frac{2\sigma}{R},$$

where  $E$  is field strength on surface of a drop of radius  $R$ ,  $\sigma$  is liquid surface tension coefficient.

The histogram of deposited particle sizes presents itself the sharply decreasing exponential function in range 2- 40nm [2]. The number of small particles on 3 order exceeds the number of the biggest ones. The separate drops with sizes near 100nm are observed. Note that the generation of nanoparticles takes place by threshold way and it is accompanied by ion current oscillation with frequency of tens of megahertz (MHz). The excitation of capillary instability on surface of liquid emitter [4] is the reason of the oscillation.

The registered particle sizes define the formation possibility of low-sized structures on the surface by the means of source dispersed phase that is the subject of present investigation.

### EXPERIMENT

The LMIS of container type, by the means of which the beams of ions In, Sn, Au, Ni, Ge, B (fig. 1, a) are obtained, is used.

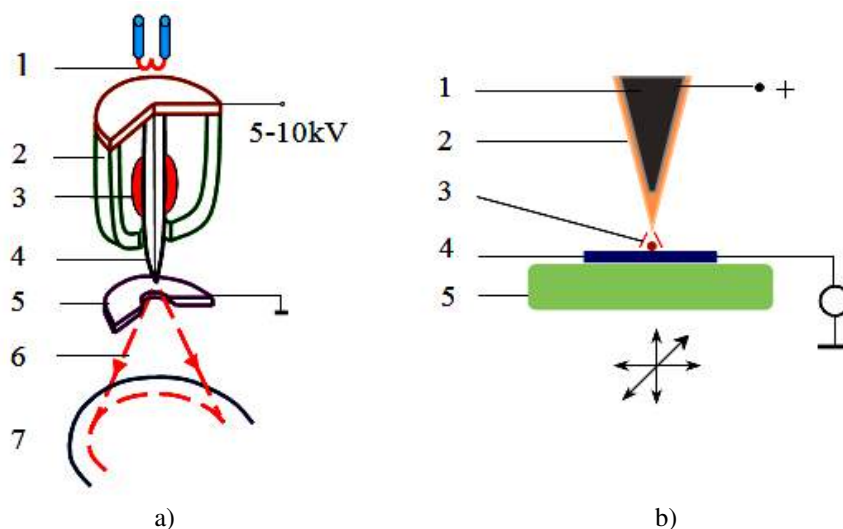


Fig. 1. a) LMIS scheme: 1 is cathode, 2 is container, 3 is working substance, 4 is tip, 5 is extractor, 6 is ion beam, 7 is collector; b) scheme of substrate three-dimensional shift relative to emitter tip: 1 is tip, 2 is working substance, 3 is ion beam, 4 is substrate, 5 is piezo-table.

The material of refractory tip is chosen for each working substance with the aim of reliable wetting of its surface. The graphite container with the tip and working substance is heated from backside by electron bombarding up to melting point of working substance. The strength of several kilovolt for the achievement of ion emission, is given on extractor situated in the distance up to 1mm from the tip. At ion current near  $40 \mu\text{A}$  (In, Sn) its oscillations with frequency of tens of megahertz appear, simultaneously, the charged particles are generated. At necessity the beam composition is defined by the means of mass-analyzer with crossed electromagnetic fields of Vin velocity filter type [5]. Taking under consideration the small divergence of nanoparticle beam it is possible the obtaining the narrow paths at horizontal shift of substrate situated in close distance from the tip. In the given case, the complex ion optics isn't used. The polished plates from cuprum, tungsten, molybdenum and silicon are used in the capacity of conducting substrate. The piezo-table by mark PZU 2300 which allows the vertical shift up to  $300\mu\text{m}$  with accuracy to 1nm and horizontal shift up to 100 mm (fig. 1, b), controlled by the computer, is used for precision shift of the substrate in three coordinates. The velocity of horizontal shift varies in interval 0,5–2 mm/sec. The piezo-table is put in vacuum camera. It demonstrated the reliable work at residual pressure  $p \lesssim 10^{-5}$  mm of mercury. The system is mounted on the base of vacuum installation A-700 Q Leybold-Heraeus with turbo-molecular evacuation. The deposited stripes are analyzed by the means of optical, raster electron and atomic force microscopes.

## RESULTS AND DISCUSSION

At usual ion release by the means of extractor (distance tip-extractor 0,5–1mm) the emission threshold voltage is 5÷6 kV. At the replacement of extractor by the plane substrate and approach of tip to it, the emission voltage essentially decreases. The stripe containing ions and indium nano-particles deposited on the tungsten plate is presented in fig. 2.

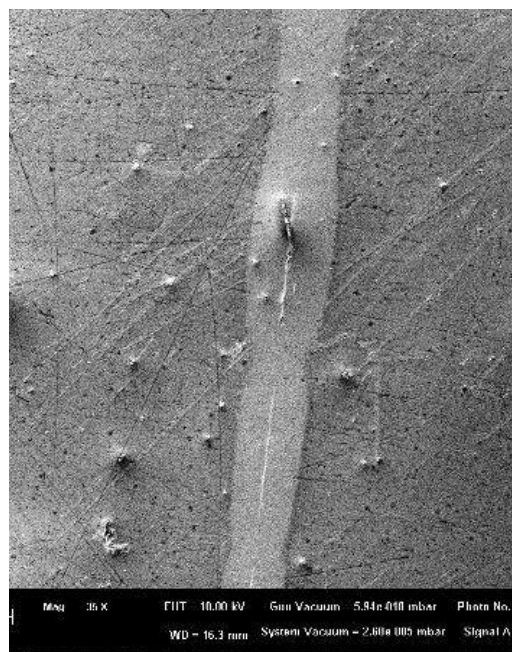
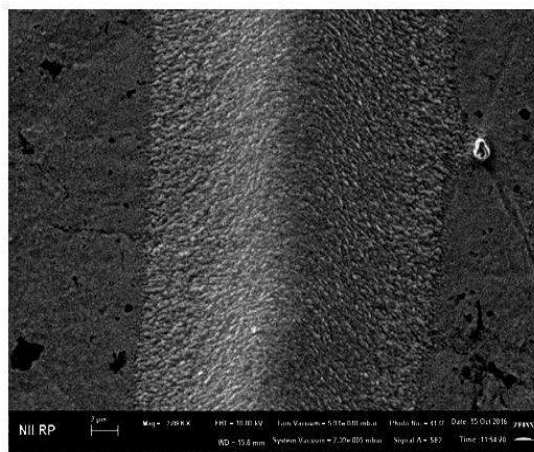
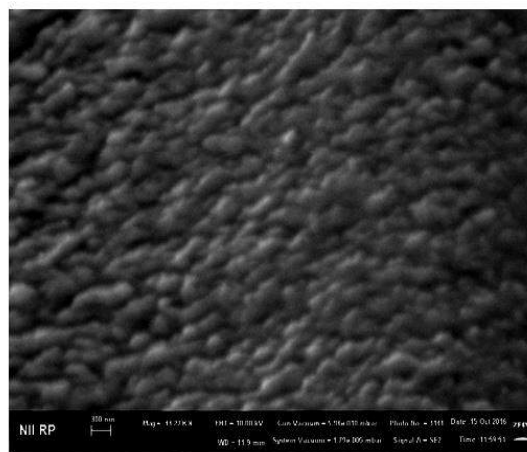


Fig. 2. FEM is the image of indium stripe on the surface of tungsten plate.

The extraction voltage is 4,5 kV, the distance tip-plate is  $200\mu\text{m}$ . The stripe has the width near  $200\mu\text{m}$  and it is defined by diameter of ion beam. The narrow path caused by nanodrop deposition is clearly seen in the middle of the stripe. This path width is  $20\mu\text{m}$  (fig. 3, a) and its central region is essentially increased in comparison with neighbor regions, it has coarse-grain structure (fig. 3, b). The character diameter of extended grains is 50-60 nm and the length is 100-200 nm. These sizes exceed the generated nanodrop sizes [6, 8]. Probably, the substrate significantly heats, the deposited particles aren't condensed that leads to their coagulation and formation of big grains because of high density of ion current. The calculation shows that the ion current density is approximately  $10\text{A}/\text{cm}^2$  on the distance 10 cm from tip and beam power is  $3 \cdot 10^4 \text{ Vt}/\text{cm}^2$ . The effective energy dissipation from the substrate is necessary in order to the nanodrops condensed not attach to each other.



a)



b)

Fig. 3. a) FEM-image of the trace of deposited nanoparticles; b) trace structure.

The substrate is fixed to massive cuprum radiator for increase of thermal tap from the substrate. The approach of the tip to the surface allows us to deposit

the narrower stripes with axial path width in several microns (fig. 4).

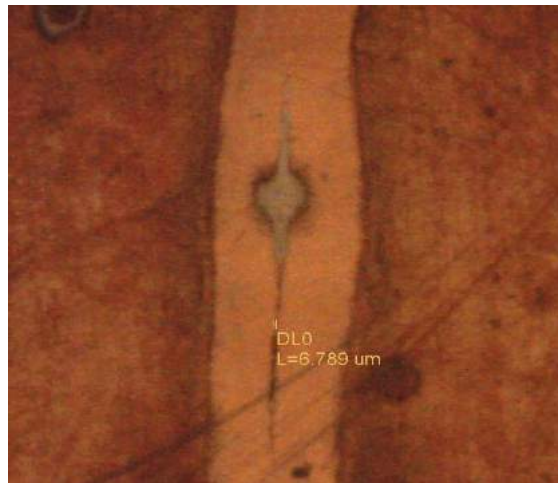
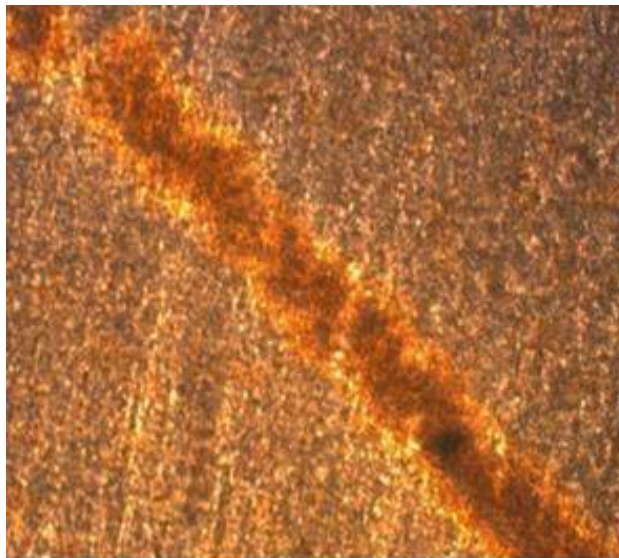


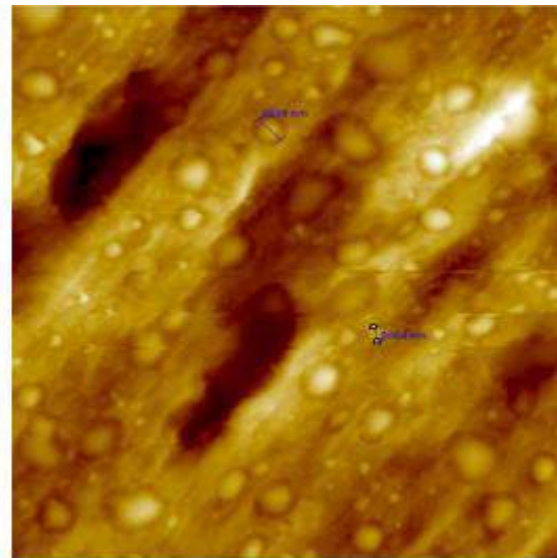
Fig. 4. The optical image of indium stripe on the surface of cuprum plate. The distance tip-plate is 80  $\mu\text{m}$ ,  $U = 3 \text{ kV}$ .

The further approach of the tip to the surface leads to smoothing of transversal profile of the deposited stripe: it becomes more heterogeneous one (fig. 5, a). Probably, now the deposited substance is heated almost up to the melting point and axial massive path isn't condensed. The stripe structure

isn't already grain one but in it the dispersion phase distributes evenly (fig. 5, b). The big particles with sizes in several microns are easily distinguished, but probably, the number of small particles is essentially exceeding the number of big ones.



a)



b)

Fig. 5. a) AFM-image of indium stripe on the surface of molybdenum plate. The distance tip-plate 50  $\mu\text{m}$ ,  $U = 3,5 \text{ kV}$ ,  
b) Dispersed stripe structure.

## CONCLUSION

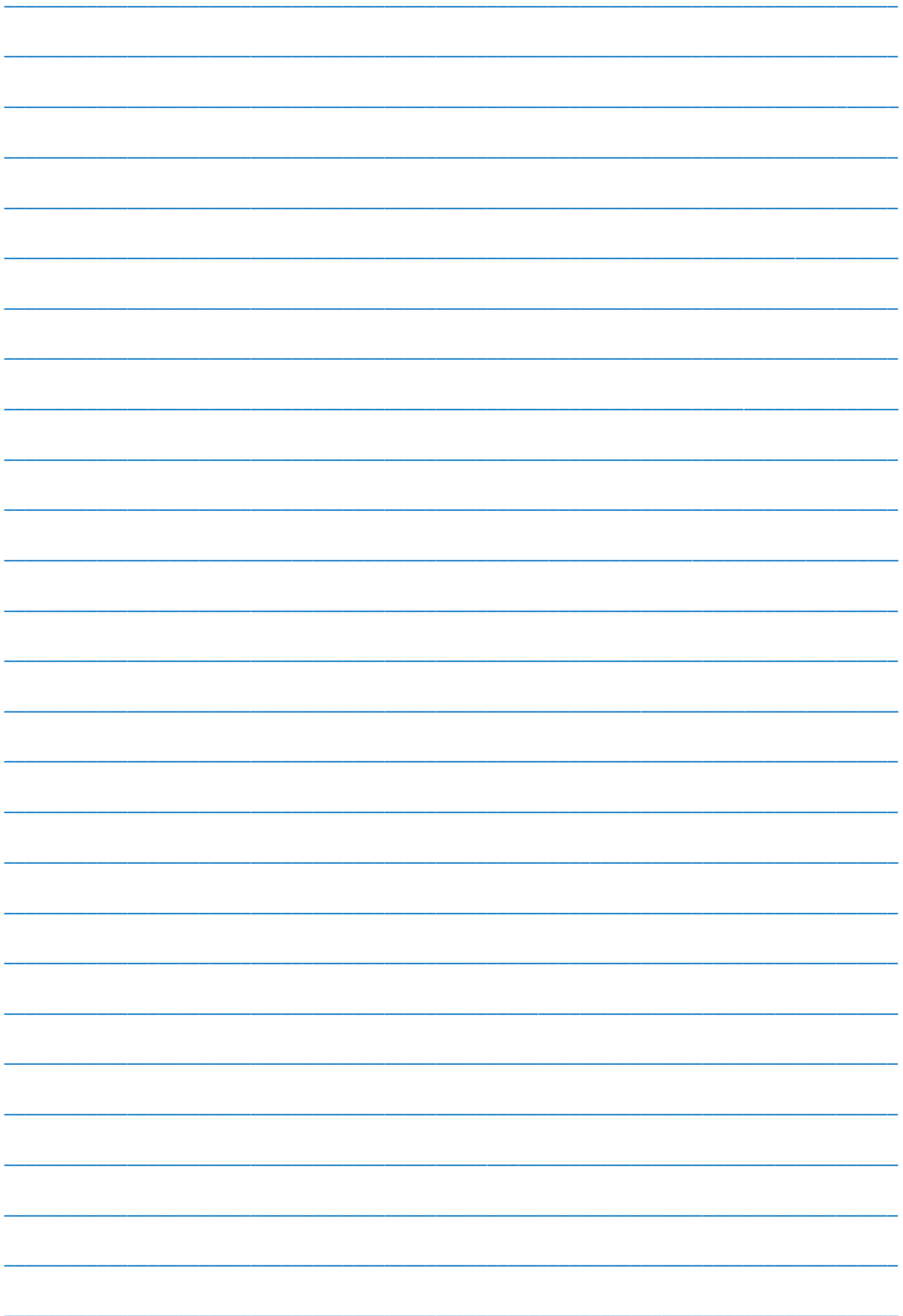
The long stripes In and Sn of width in several microns are formed by deposition of fine-dispersed phase of liquid metal ion source on nearby uncooled surface. The stripe structure is caused by particles of submicron sizes. There are not complex elements of ion - optical devices in system. The formation of

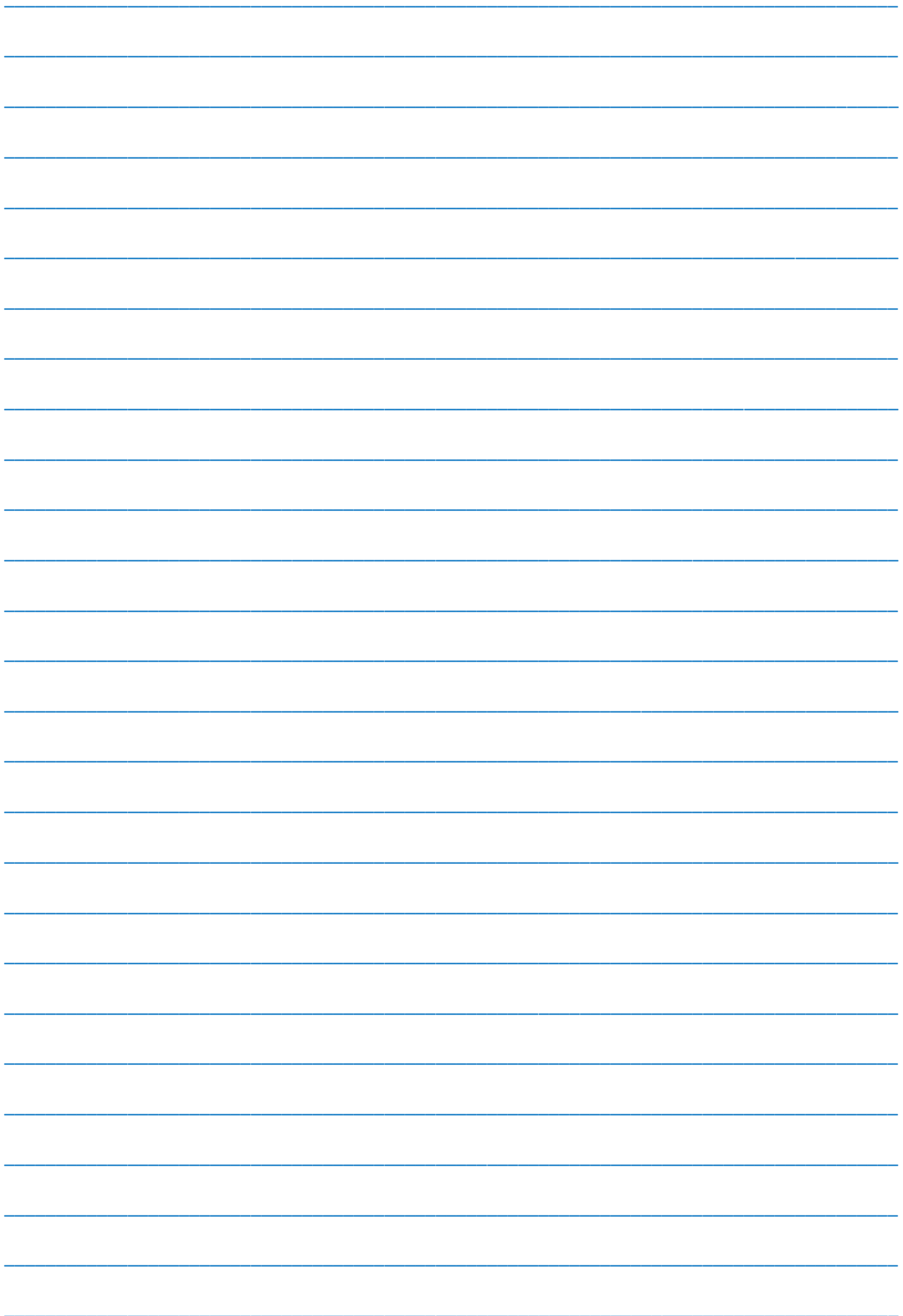
narrower surface structures presenting themselves the practical interest is possible by appropriate substrate cooling. If paths are deposited on cooled thin metal film, then it can be eliminated by etching. The given method can be applied in micro-electronics with the aim of carrying out of different technological operations.

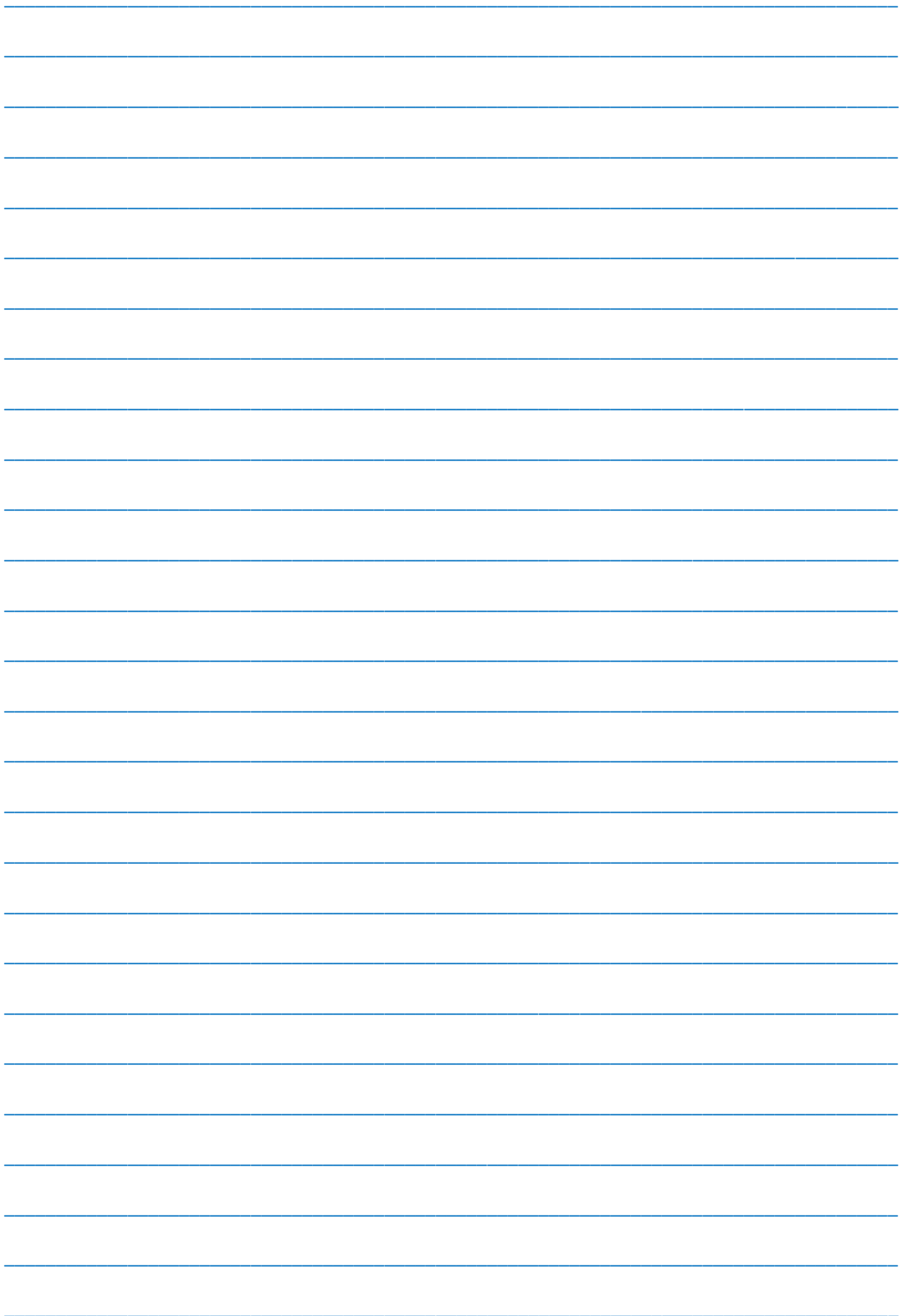


- [1] V.V. *Badan*, I.S. *Gasarov*. The finely dispersed phase and instability of the emission of liquid metal ion sources , Technical Physics Letters, v. 15, No. 17, p. 49-52, 1989.
- [2] I.S. *Hasanov*, I.I. *Gurbanov*. Formation of charged nanoparticles at capillary instability of the liquid emitter, JJAP, 47, No. 10, p. 8226-8229, 2008.
- [3] Charged Particle Optics. Edited by J. Orloff (CRC Press, London, New York, 2009), p. 665.
- [4] V.E. *Badan*, V.V. *Vladimirov*, V.P. *Gorshkov*, I.A. *Soloshenko*. Instability of Rayleigh and Faraday in liquid metal ion sources. Drop emission and the phenomenon of mikrodroplet chaos., Technical Physics, v. 63, No. 6, p.47-65, 1993.
- [5] I.S. *Gasarov*, I.I. *Gurbanov*. Nanostructure operations by means of the liquid metal ion sources., Rev. Sci. Instr., 83, 02B906, 2012.
- [6] I.S. *Gasarov*, I.I. *Gurbanov* and E.M. *Akbarov*. Losses of ion energy in the multicomponent beam. Eur. Phys. J. D., 2015. DOI: 10.1140/epjd/e2015-50531-0
- [7] I.S. *Gasarov*, I.I. *Gurbanov* and E.M. *Akbarov*. Ions passage through nanodroplets in multicomponent beam, ACTA Physica Polonica A, 134, No. 1, p. 119-121, 2018. DOI: 10.12693,APhysPolA.134.119
- [8] C. *Akhamadeliyev*, L. *Bischoff*, G.L.R. *Mair*, C.J. *Aidinis* and Th. *Ganetsos*. Investigation of emission stabilities of liquid metal ion sources, Microelectron. Eng., 73-74, p. 120-125, 2006.

*Received: 18.03.2020*









## CONTENTS

1.	Polarization effects at Higgs Boson decay $H \Rightarrow f\bar{f}\gamma$ <b>S.K. Abdullaev, E.Sh. Omarova</b>	3
2.	Comparative study on the electrical characteristics of Au/n-Si and AU/P3HT/n-Si Schottky contacts <b>X. Hidiyev, A. Asimov, A. Kerimova</b>	13
3.	Analysis of fluctuation conductivity in $Y_{0.6}Cd_{0.4}Ba_2Cu_3O_{7-\delta}$ <b>V.M. Aliev, J.A. Ragimov, R.I. Selim-Zade, B.A. Tairov</b>	17
4.	The study of the photoresponse of the MAPD matrix for scintillation radiation <b>Ramil Aladdin Akbarov</b>	21
5.	First principles study Ge -doped monolayer graphene <b>S.S. Huseynova</b>	25
6.	Dielectric properties of $Ba_{0.8}Sr_{0.2}TiO_3$ in heating and cooling processes <b>A.E. Nabiyev</b>	30
7.	Influence of Nd impurity atoms and gamma irradiation on roentgenographic spectrum of GeS layered single crystal <b>A.S. Alekperov, A.E. Nabiyev, T.M. Aydinova</b>	34
8.	Deposition of nanodrop phase from emitter tip on nearby mobile surface. <b>I.A. Gasanov</b> , S.A. Aliyev, I.I. Gurbanov, E.M. Akberov, F.E. Mamedov, A.H. Kerimova	40



[www.physics.gov.az](http://www.physics.gov.az)